HIGH RESOLUTION CHARACTERIZATION OF RESERVOIR HETEROGENEITY WITH CROSS-WELL SEISMIC DATA

BRADLEY J. BONNELL

High Resolution Characterization of Reservoir Heterogeneity with Cross-well Seismic Data

By
©Bradley J. Bonnell

A thesis submitted to the
School of Graduate Studies
in partial fulfillment of the requirements for the degree of
Master of Science

Department of Earth Sciences
Memorial University of Newfoundland
November 2006

Centre for Newfoundland Studies
APR 21 2008
MEMORIAL UNIVERSITY
OF NEWFOUNDLAND

St. John's Newfoundland

Abstract

Traditionally, reservoir characterization is limited to the inadequate frequency content of surface seismic data and the poor spatial sampling of borehole data for detecting metre-scale heterogeneities affecting fluid flow. Cross-well seismic data can provide the spatial and temporal resolution necessary for imaging these reservoir features. Three synthetic cross-well seismic datasets are created using velocity models that simulate lithologic detail and reservoir heterogeneities at the metre-scale. The first model is derived from an outcrop study of a deltaic depositional environment, and the second and third models are developed from offshore well log data. Statistical analysis of the lateral spatial properties of the high resolution seismic depth images produced from the models provides estimates of the lateral correlation length and the fractal dimension. The results display a unique distribution of spatial properties for each model, indicating that different types of reservoir heterogeneity result in distinctive statistics that are captured by the seismic data. These estimates can be used to provide high resolution constraints on reservoir heterogeneity that can be built into reservoir simulations.

Acknowledgements

Sincere thanks are extended to my supervisor, Dr. C.A. Hurich, for his invaluable knowledge and guidance throughout this project. Funding was provided through the Pan-Atlantic Petroleum Systems Consortium (PPSC), and through Natural Sciences and Engineering Research Council (NSERC) of Canada grants awarded to Dr. Hurich. The processing resources for this project were provided by Landmark Geophysical Corporation and by the Natural Sciences and Engineering Research Council (NSERC) of Canada.

The following people are owed many thanks for their support during this thesis. My second supervisor, Dr. R. Meyer, supplied valuable assistance with the geology and building of the models for this project. Leon Normore also assisted with the model building by providing information from his thesis work. Tony Kocurko provided the much appreciated technical support, which made my research more efficient and enjoyable. Dr. S. Deemer and the *ProMAX*® support staff supplied valuable processing help in *ProMAX*®. Matthew Hamilton also assisted with the processing by writing a piece of code for one of the processing steps. These people supplied much needed support and guidance for carrying out this project.

Friends and family have provided friendship and moral support throughout this project. I would like to thank my fellow graduate students, especially Stephen Kearsey and Stacey Mansfield, for making my time as a graduate student very enjoyable. Special thanks are extended to my parents, Wilf and Sandra Bonnell, for their continued support during my educational years, and Andrea Hickman for her patience and encouragement.

Table of Contents

List of Figures

Chapter 3

List of Tables

Chapter 1

Introduction

Characterization of reservoir heterogeneity is important for the understanding and optimization of production of oil and gas reservoirs. Reservoirs commonly contain impermeable lithological units and heterogeneous porosity/permeability distributions that are further affected by complex fault systems that all significantly control fluid flow paths and distribution. Fluid flow is affected by heterogeneity at a range of scales from the sub-metre scale, up to 10's of metres, but the predominant control is exerted by bedding, pore fluid changes, and diagenetic effects at the metre-scale (Grammer, et al, 2004).

Traditionally, well logging and surface seismology are the primary methods used to characterize reservoir features, but both have limitations that control the resolution of that characterization. Well log data is used to sample reservoir features at <1m vertical resolution (Whelan, personal communication), whereas surface seismic data typically have a vertical resolution of 30 – 50m at the reservoir interval depending on the frequency content (Yilmaz, 1999). However, well log data only sample a very small portion of the entire reservoir near the borehole and well spacing is typically larger than the spatial sampling of surface seismic data, which is typically around 10 – 30m (depending on acquisition geometry). The differences in vertical and spatial resolution that exist between well log and surface seismic data leave a gap in the effective scale of

reservoir characterization that includes the features that exert the strongest controls on fluid flow.

The resolution gap between seismic data and well log data can be alleviated by cross-well seismic data (Figure 1.1). Temporal and spatial resolution necessary for characterization of reservoir heterogeneities at the metre-scale can be achieved through cross-well seismic imaging. The geometry of cross-well seismic acquisition avoids near surface effects that drastically attenuate high frequencies, and provides a relatively short propagation distance for seismic energy that mitigates absorption. These two factors allow for high resolution sampling (~1m) directly at reservoir depths (Lazaratos, 1993). By bridging the resolution gap between seismic and well log data reservoir engineers have the opportunity to more accurately characterize reservoir performance.

Figure 1.1: Schematic showing how cross-well data bridges the resolution gap between surface seismic data and well log data.

Reservoir engineers perform flow simulations through a reservoir model, built using well logs, cores, seismic data, conceptual geological models, well tests, and production history to help understand fluid paths and production rates (Deutsch and Hewett, 1996). Reservoir simulations generate numerous predictions, presented in the

form of worst-, mid-, and best-case production forecasts that represent uncertainties incorporated into the simulations by disparate data. The sources of data carry information at different scales of resolution, at various degrees of precision, related to the true distribution of petrophysical and fluid properties of the reservoir. One particular source of uncertainty arises from the upscaling of well log data for correlation with surface seismic data. By upscaling, the data doesn't accurately represent reservoir variations at scales important for understanding features affecting fluid flow paths and distribution.

Reservoir flow predictions should be rendered more reliable by introducing cross-well seismic data. Cross-well seismic data is closer to the vertical resolution of well log data, and provides an order of magnitude greater spatial resolution of the reservoir than surface seismic data, largely due to the higher frequency content. The higher frequency content of cross-well seismic data is a result of the cross-well arrivals not experiencing the low-pass filtering of the near surface. Theoretically, cross-well seismic data should be able to resolve features a metre apart vertically, and resolve features a few (2-3m) metres apart horizontally (Appendix A). Features above the seismic resolution will produce coherent reflections that can be entered deterministically into the reservoir model. Features below the resolution limit will generate a scattered wavefield. It is from the scattered wavefield that geostatistical information in the form of stochastic descriptions can be extracted from cross-well seismic data to provide additional metre - scale constraints on the reservoir model. Additional statistical and deterministic constraints to

the reservoir model should reduce uncertainty in simulation results, hence improving design of reservoir production schemes.

This study aims to evaluate the effectiveness of borehole-to-borehole seismology for providing high resolution reservoir images and extraction of geostatistical information that can be used in reservoir simulation. Three synthetic cross-well seismic datasets are created using velocity models derived from petroleum reservoirs that simulate lithologic detail and reservoir heterogeneities at the metre-scale. The first model is derived from an outcrop study of the mid-Cretaceous age Ferron Sandstone Member in central Utah, USA, representing a deltaic depositional environment. The second and third models are developed to examine two different classifications of porosity heterogeneities based on well log data in the mid-Cretaceous age Ben Nevis Formation, offshore Newfoundland, Canada. The geostatistical information extracted from the processed cross-well seismic data adds significant new information applicable to reservoir characterization methods.

Chapter 2

Model Construction

Section 2.1 Introduction

Two sources of data are chosen to create the two dimensional velocity models for this study. The criteria used to select these sources of data are based on whether sufficient information is available to create a detailed reservoir model, and if a velocity model could be derived from the information. The first source of information is from a detailed outcrop study used as an analogue for many highly productive oil and gas reservoirs. The second source is from an offshore petroleum well, where well logs and core data are available. These two sources of data provide small-scale features about their respective reservoirs, important for understanding flow behavior and distribution within a reservoir.

2.2 Model 1: Parasequence sets within the Ferron Sandstones, Utah

The first model is created based on data from a study of the Ferron Sandstone Outcrop Belt in Utah by the Utah Geological Survey (Chidsey, 2001) (Figure 2.1). The Ferron Sandstone has been used as a deltaic reservoir analogue for highly productive oil and gas reservoirs in the Gulf Coast, Rocky Mountain basins, Alaskan North Slope, North Sea, and other reservoirs around the world (Chidsey, 2001). The model is constructed from a small portion of the outcrop belt called the Ivie Creek case-study area,

chosen because of the detailed mapping of the outcrop area and the high density of permeability data extracted along transects of the outcrop.

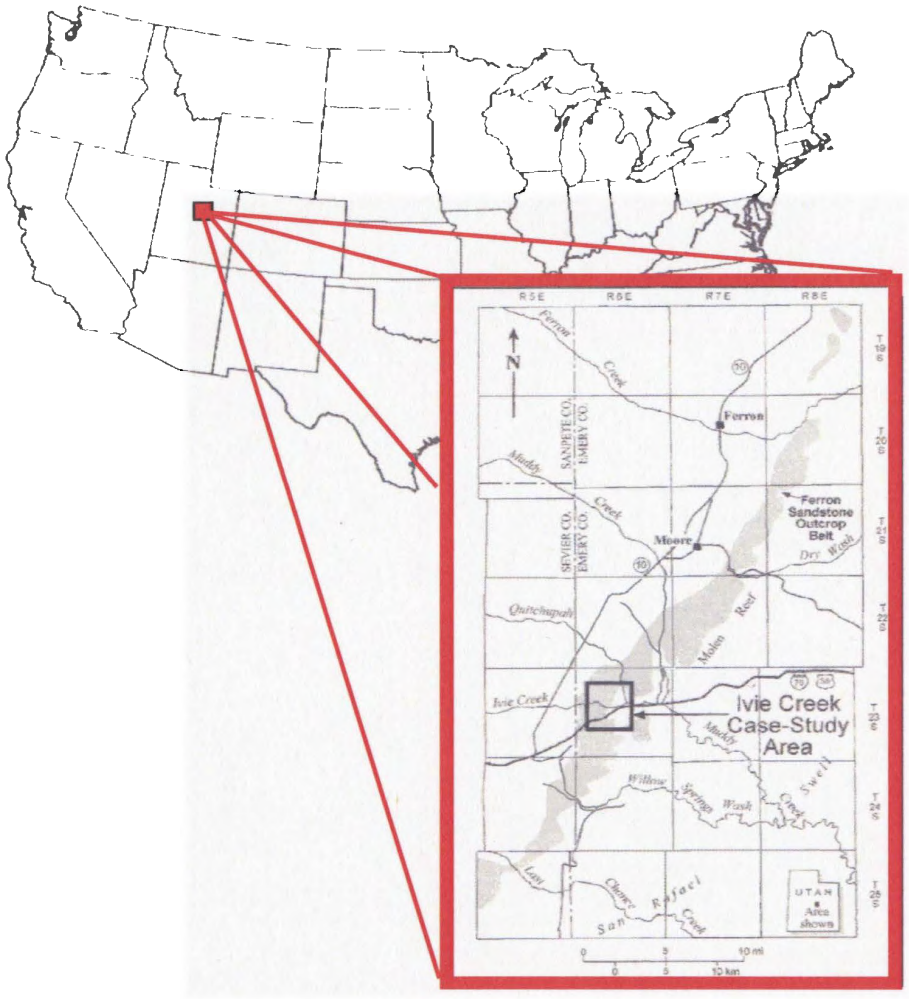

Figure 2.1: Location of the Ivie Creek case-study area, in Utah, USA. (modified from Chidsey, 2001).

2.2.1 Geological description of modeled parasequence sets

The Ivie Creek case-study area is a reservoir analogue for fluvial-dominated deltaic reservoirs. The outcrop contains two out of seven, ~20m thick, regional-scale parasequence sets contained in the entire Ferron Sandstone Outcrop Belt (Chidsey, 2001). The lower parasequence set, Kf-1, is interpreted as a fluvial-dominated delta deposit containing two bedsets that conformably overlies a shale unit called the Tunack shale member (Figure 2.2). The lower bedset (Kf-1-Iv[a]) is composed of sand-rich, fluvial deltaic dipping lobes that were deposited in an environment of minimum wave influence (Chidsey, 2001). At a smaller scale, Kf-1-Iv[a] has been sub-divided up into the following four clinoform facies (Figure 2.3) based on grain size, sedimentary structures, bedding thickness, inclination angle of the bed, and stratigraphic position: 1) clinoform proximal; 2) clinoform medial; 3) clinoform distal; and; 4) clinoform cap. Clinoform proximal represents deposits closest to the sediment source. These beds are composed of sandstone and were deposited at an inclination generally greater than 10^{o}. Clinoform medial is sandstone package with about 5% shale, dipping from 2^{o} to 10^{o}, representing deposits at an intermediate distance from the sediment source. Clinoform distal represent beds furthest away from the sediment source and were deposited primarily horizontal, composed of sandstone and about 10% shale. Clinoform cap is interpreted to be eroded and reworked delta top deposits composed of sandstone deposited horizontally (Chidsey, 2001). Clinoforms range in thickness from 1-2m to almost 10m, and extend laterally from 5m to greater than 100m.

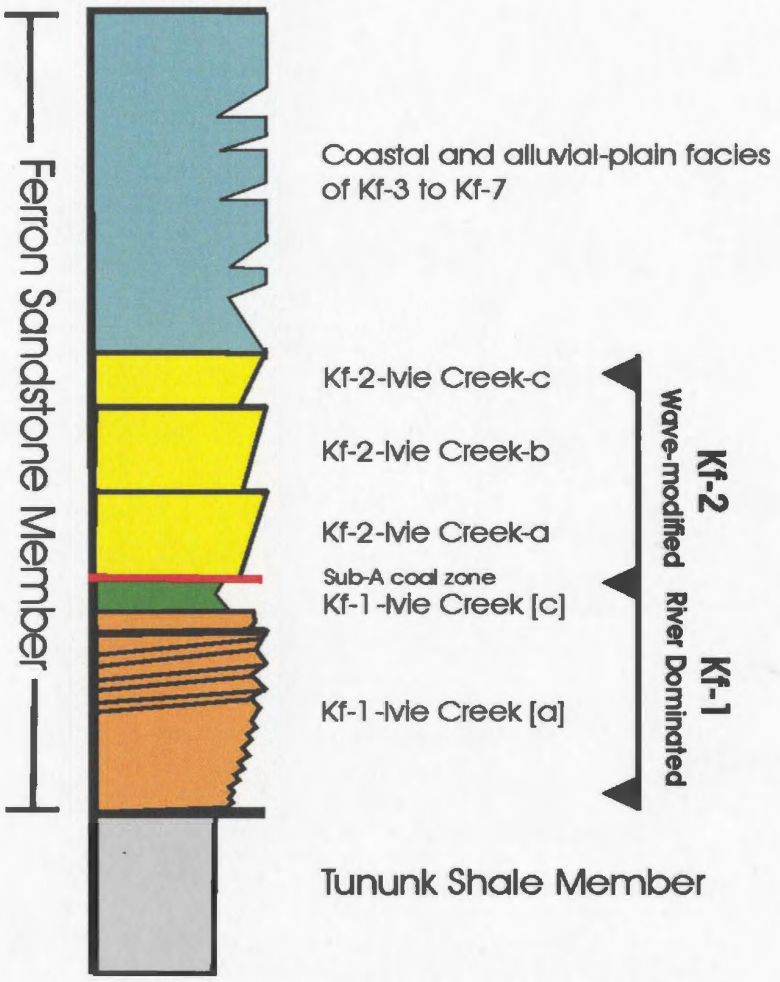

Figure 2.2: Schematic diagram of the stratigraphy for Ivie Creek case-study area (modified from Chidsey, 2001).

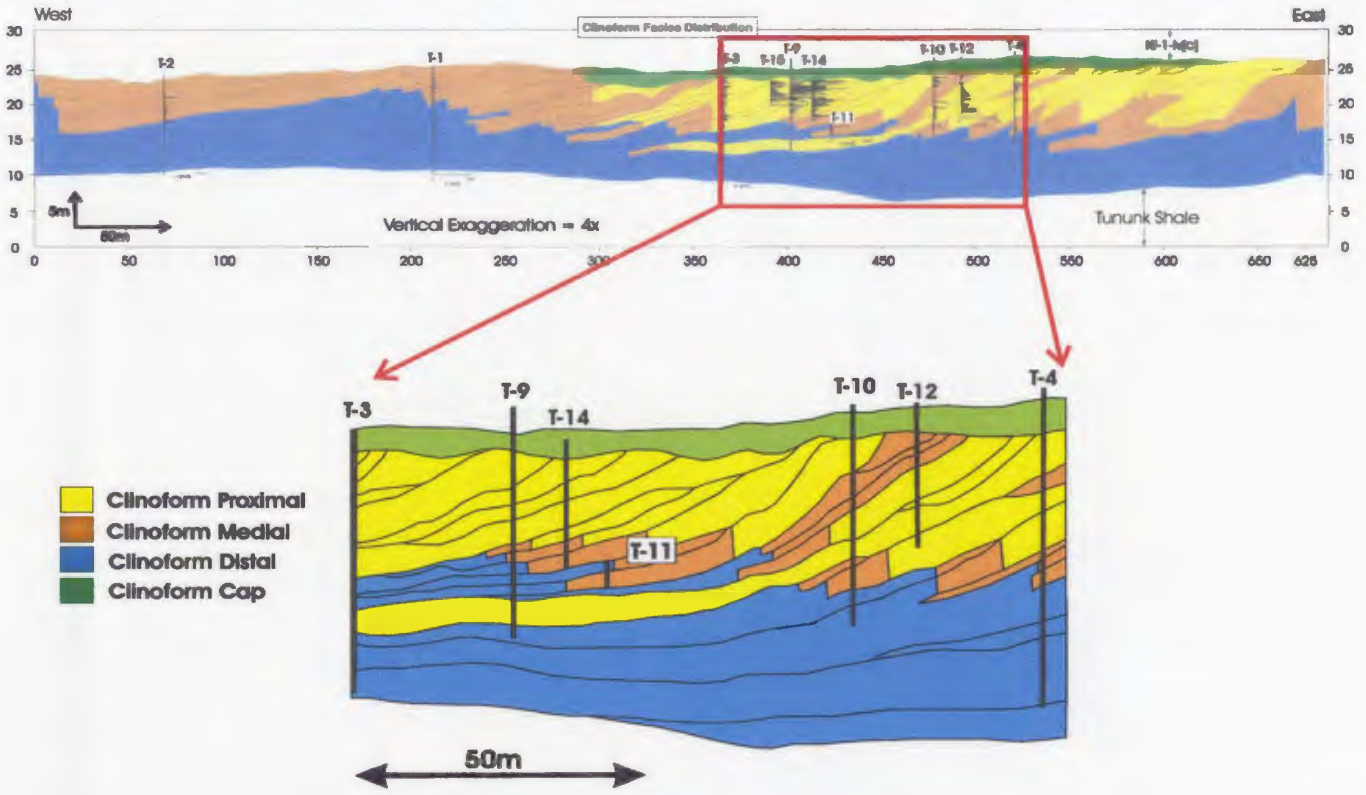

Figure 2.3: Portion of the Ivie Creek case-study area used for modeling, displaying the clinoform facies distribution and permeability transects (modified from Chidsey, 2001).

The upper bedset, Kf-1-Iv[c], is interpreted as the distal portion of another delta lobe, and has indications of wave and fluvial influences (Chidsey, 2001). The bedset is sand-rich and beds dip less then 5^{o} and is overlain by a thin layer of coal identified as the Sub-A coal zone (Figure 2.2).

The upper parasequence set, Kf-2, is divided into three parasequences named from oldest to youngest, Kf-2-Iv-a, Kf-2-Iv-b, and Kf-2-Iv-c (Chidsey, 2001). The lower part of Kf-2-Iv-a is interpreted as a prodelta to lower shoreface deposit consisting of interbedded sand and minor shale. Overlying are carbonaceous sandstone deposits from a middle shoreface environment. The Kf-2-Iv-b parasequence is composed of silty sandstones deposited in a middle shoreface environment at the base, and towards the top are distributary channel to mouth-bar deposits composed of sandstone. The youngest parasequence, Kf-2-Iv-c, is composed of sandstones from upper shoreface deposits (Chidsey, 2001).

2.2.2 Method of creating the model

The velocity model is created from permeability measurements taken from a cross-section of the Ivie Creek case-study area (Figure 2.3). This area is chosen because of its high density of permeability transects within a relatively small areal extent (8 transects within 125m). The area is extended vertically by a factor of 3 in order for the clinoforms to be within the resolution limits of cross-well seismic data (therefore all clinoform thicknesses mentioned henceforth are referred from the vertically exaggerated section). The permeability transects sample most of the clinoforms mapped in the section

that ranged in thickness from 1 – 10m, and extended 5 – 125m laterally. With such a large range in sizes of clinoforms, applying a constant velocity to each clinoform is sufficient to create a heterogeneous reservoir model detectable by cross-well seismic data. To construct a more complete section, parasequence sets Kf-3 to Kf-7 are used also, because without them the model would not have sufficient vertical extent to acquire a cross-well survey. These parasequence sets are not observed in outcrop in the Ivie Creek case-study area, but are extrapolated from the full stratigraphic thickness of the Ferron Sandstone to create a total section 280m thick. Permeability measurements are not acquired as in Kf-1 and Kf-2, so they could not be modeled in detail, but their relative thicknesses are incorporated into the model.

Velocities are derived from the large quantity of permeability measurements taken along transects T3, T15, T9, T14, T11, T10, T12, and T4 of parasequence sets Kf-1 and Kf-2 in the Ivie Creek case- study area (Chidsey, 2001) (Figure 2.3). The permeability measurements were acquired using a mini-permeameter on core plugs, drilled from the outcrop, 2cm in diameter and 2.5-7.6cm in length. A length of 2.5-7.6cm was used to avoid chemical weathering, which is shown to extend less than 1.3cm into the rock through drilling experience and examination of the core plugs (Chidsey, 2001). Laboratory measurements of porosity and permeability were also taken of the core plugs, for which a linear relationship between porosity and permeability was derived,

$$\ln(k) = -6.657 + 56.6 * ö$$

where k is permeability and ö is porosity (the symbol ö is used for consistency with Chidsey, 2001). Laboratory measurements were also taken to develop a relationship

between velocity and porosity at subsurface pressures (Chidsey, 2001). From a graph used to display the relationship (Figure 2.4), a curve was fit to the data points by Chidsey (2001) and a linear relationship is derived,

$$v = -9E^{-10}ö^2 - 9683.2ö + 5765.7$$

where v is velocity as a function of porosity. For the purposes of this study, the curve fit to the data points from Chidsey (2001) is used, however other curves could be fit, but would not change the seismic response significantly. The only difference would be the amplitude strength of the reflections and scatters. From the above equations, velocities can be derived from the permeability measurements taken in the field (Appendix B).

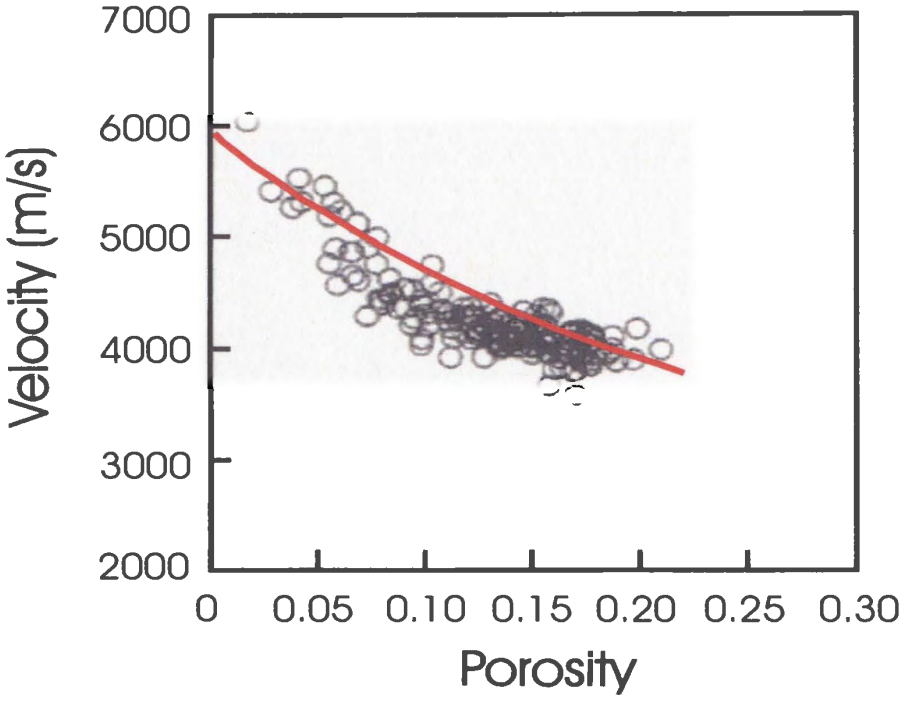

Figure 2.4: Velocity vs. porosity graph derived from laboratory measurements of plugs taken from the Ivie Creek case-study area (modified from Chidsey, 2001).

The permeability measurements extracted from the field are very finely sampled (~1.5cm), meaning numerous measurements could fall within a clinoform that are too finely sampled for detection by the cross-well seismic technique. Therefore, all velocities falling within a particular clinoform are averaged, and if a clinoform is sampled by more than one transect, then the average of those transects are averaged. If a clinoform is not sampled by a transect, then surrounding clinoforms are used to derive a velocity. This way a clinoform is represented by a single velocity, and effects from possibly erroneous permeability measurements are suppressed. Velocities for parasequence sets Kf-3 to Kf-7 are given a smoothly increasing velocity function with depth, since velocity information is not available for these layers. Figure 2.5 displays the final velocity model.

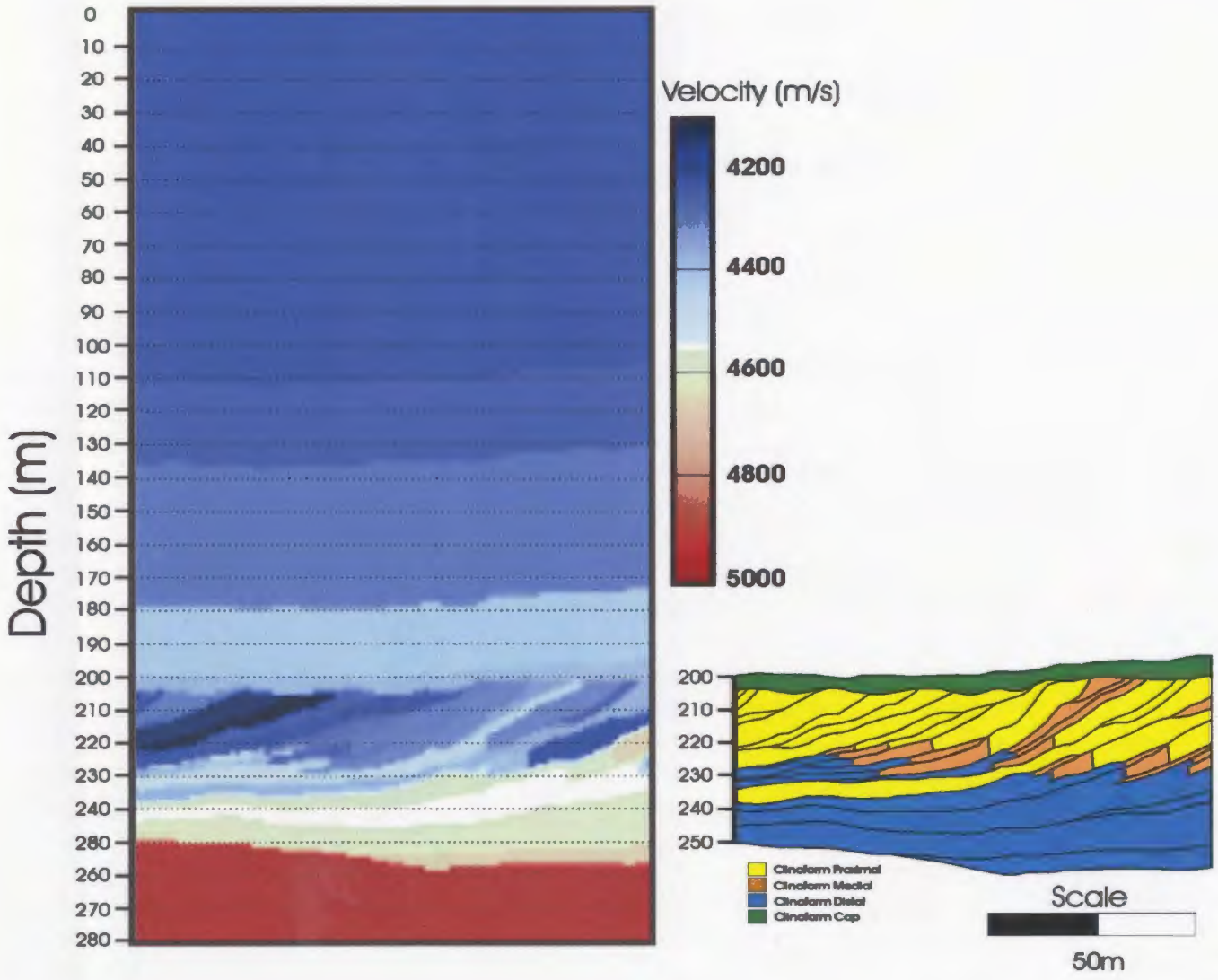

Figure 2.5: Velocity model and cross-section created from the Ivie Creek case-study area.

2.3 Models 2 and 3: White Rose Field, offshore Newfoundland

The second and third models are derived from a well and several cores in the White Rose Field on the Grand Banks, offshore Newfoundland and Labrador (Figure 2.6). The White Rose Field is the third largest field in the Jeanne d'Arc Basin and is expected to deliver approximately 200 – 250 million barrels of recoverable oil and contains approximately 2 trillion cubic feet of gas (Husky, 2001). A 250m section of the Ben Nevis Formation sandstones that constitutes the reservoir is the model for this study.

Figure 2.6: Bathymetry map showing the location of the White Rose Field offshore Newfoundland (modified from website http://www.budget.gov.nl.ca/budget2001/economy/whiteRose.htm).

The two models are used to address two specific issues concerning reservoir quality of the Ben Nevis Formation in the White Rose Field. The first issue concerns highly impermeable calcite-cemented concretionary intervals located in the reservoir interval that impede fluid flow. The lateral extent of these concretionary intervals is poorly understood due to the sparse sampling of drill cores and thickness of the intervals is below the resolution of surface seismic data. Within the short width of cores, 10 – 15 cm, concretions may pinch-out or terminate abruptly. With increased resolution using

cross-well seismic data these concretions may be resolved to improve reservoir characterization.

Another issue examined in the White Rose model is the distribution of reservoir heterogeneity within the intervals of relatively uncemented reservoir sandstones. Again, the sparse sampling of wells and the poor resolution of surface seismic data does not provide the necessary information to examine the small-scale heterogeneity of the reservoir. For this model, the porosity distribution is assumed to control the heterogeneities within the reservoir sandstone, and is considered to be the primary factor controlling velocity. Since the distribution of heterogeneities is explored inside the reservoir interval, the effect on velocities due to variations in fluid concentrations within the hydrocarbon-bearing formation is assumed to be negligible.

Porosity variations are controlled, in part, by the bedding of sedimentary layers, diagenetic processes, and fracturing. Bedding creates a thin and lenticular porosity distribution as different sorting and grain sizes give bed units a different porosity (Pittman, 1979). Diagenetic processes and fracturing creates a more globular, or low aspect ratio porosity distribution. As fluids percolate through a formation, the porosity can be enhanced by dissolving minerals or reduce porosity by stimulating the growth of minerals (Pittman, 1979). Fractures influence the porosity distribution by providing a path for fluid migration through the formation. Two end-member porosity distributions, porosity controlled by bedding and diagenetic effects, are examined to observe the effect they have on the seismic character within the reservoir interval.

2.3.1 Geological description of the White Rose Field

The White Rose Field is located in the northeastern portion of the Jeanne d'Arc Basin, offshore Newfoundland (Figure 2.6). The field exhibits a complex fault system and structural trend due to three episodes of rifting along the Atlantic passive margin (Enachescu, 1987). During the second rifting stage in the late Jurassic – early Cretaceous sands were eroded from paleo-topographic highs and were deposited as shoreface sands along a north-south trending shoreline. These sands created the main reservoir rock; a massive (> 300m thick) quartzose, well sorted, fine-grained sandstone with a relatively low average permeability (~100mD), identified as the Ben Nevis Formation of Aptian-Albian age (Husky, 2000).

At the metre-scale within the sandstones of the Ben Nevis Formation, there are several intervals of calcite cementation, identified as concretionary. The intervals are irregularly spaced and their lateral extents are unknown because observations are limited to sparse well cores (Figure 2.7). These calcite concretionary intervals generally correspond to calcite cements that nucleated on/around accumulations of worm tubes and shells, and range from centimetre to metre-scale (Normore, 2005).

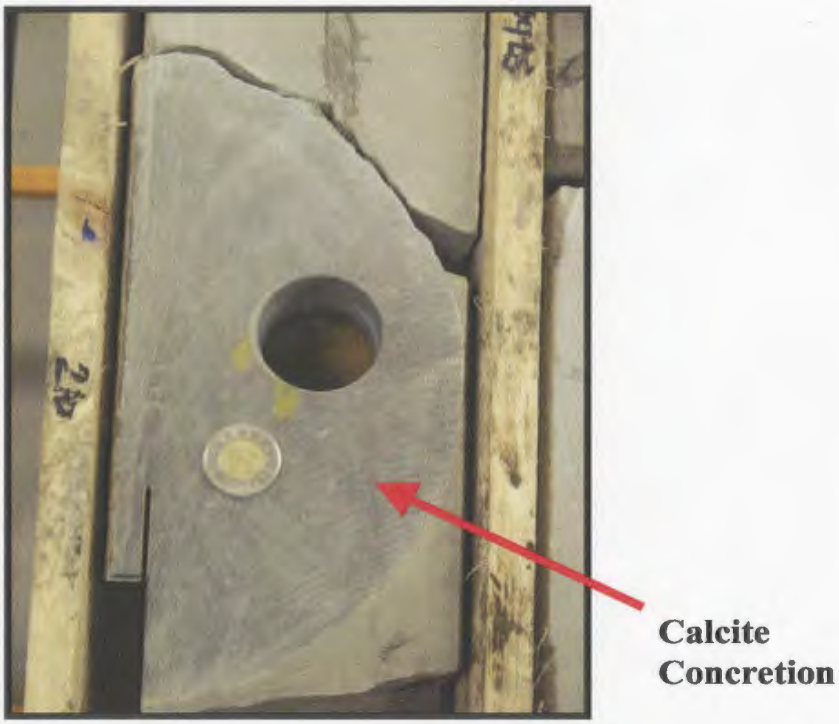

Figure 2.7: Example of a calcite concretion from a drill core taken from the White Rose Field (Normore, 2005).

2.3.2 Method of creating the model

The reservoir model is based on well data and core samples from the White Rose Field. Offshore wells are typically several kilometres apart from each other, making the distance too far for cross-well seismic data acquisition. Energy at the desired frequencies cannot be recorded at these distances and much of the reflected energy would be lost through the top and bottom of the rock column between the source and receiver well. To avoid these problems, two pseudo-wells 100m apart are created from one well covering 250m of the vertical geological section. Surface seismic data passing through the well show the stratigraphic layers to be roughly horizontal, so the layers between the two pseudo-wells are assumed to be horizontal also.

The next task was to digitize the stratigraphic column and sonic velocities contained in the well log. Well logs record data at the centimetre scale, which is beyond the detectable scale of cross-well seismic methods, so the well logs and stratigraphic column are decimated to every 0.5m, which capture almost all the layers in the stratigraphic column. Each stratigraphic layer is populated with interval velocities based on the sonic log, and all velocity measurements falling within a layer are averaged. The model is further modified to address the two reservoir issues mentioned above.

The lateral extent and thickness of concretionary layers are varied between the wells to examine the imaging capabilities of resolving layer terminations and given thicknesses. These concretionary intervals have anomalously high velocities compared to the surrounding sandstone, so strong reflections are produced, with an average reflection coefficient of ~0.09. Therefore, these concretionary layers should be easily identifiable in the seismic section and can enable reservoir engineers to improve reservoir models.

To investigate heterogeneous porosity variations within the reservoir interval, two end-member porosity distributions are examined: porosity controlled by bedding, and porosity controlled by diagenetic effects and fractures. Two models are created to examine each porosity distribution where porosity is assumed to be the main control on velocity. The hydrocarbon-bearing formation in each model contains a different stochastic velocity field representing the two types of porosity distribution. The range of velocities in the stochastic fields is derived from the range of velocities viewed in the sonic log. The first distribution is controlled by bedding so velocity variations are elongate in a horizontal direction and have high aspect ratios (Figure 2.8a).

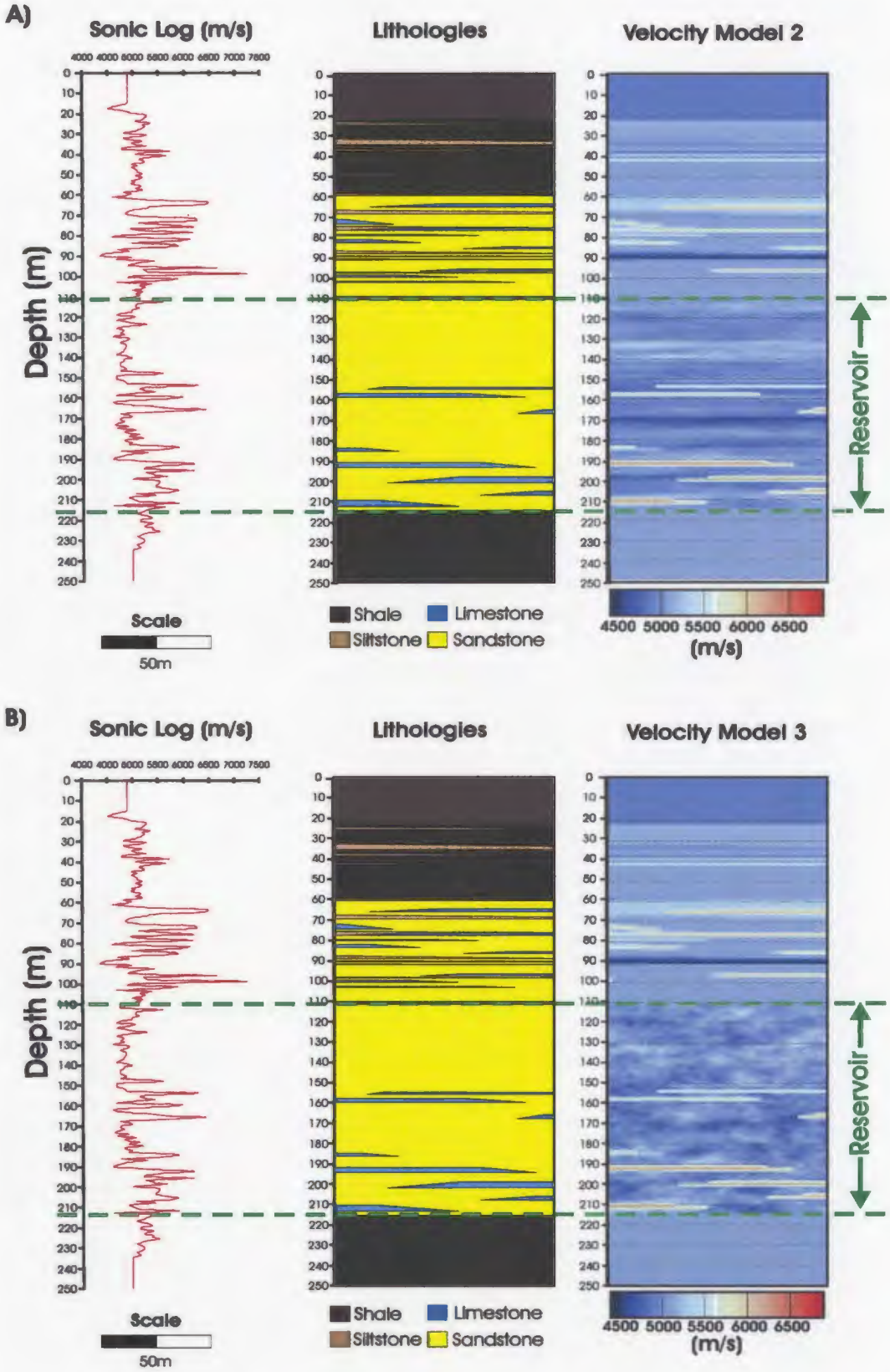

Figure 2.8: Display of the sonic log and lithologies taken from drill cores used to create velocity models 2 (A) and 3 (B).

The second porosity distribution is dominated by diagenetic effects, so velocity variations are modeled as short, subequant domains with low aspect ratios (Figure 2.8b) (please see Chapter 4 for more discussion of the stochastic velocity fields). These two different stochastic velocity fields should produce two different seismic responses that may not be interpretable, but geostatistical information can be extracted to provide high resolution descriptions of the reservoir to aid interpretation.

2.4 Preparation for ProMAX®

The three velocity models are used in *ProMAX®* to acquire the cross-well seismic data. In order to input the velocity models into *ProMAX®* the velocity models are converted into trace data, where the amplitudes are representative of the velocity, and output in SEG-Y format. Chapter 3 describes how these velocity models are used in *ProMAX®* to acquire the cross-well seismic data, and the processing of the data.

2.5 Discussion

This chapter describes the methods for constructing the three velocity models, which will be used to acquire synthetic cross-well seismic data. The first model is derived from permeability data acquired from the Ivie Creek case-study area, located in Utah, USA. The Ivie Creek case-study area contains a suite of dipping clinoform facies from a fluvial deltaic environment, which is the reservoir interval in the model. The second and third models are derived from sonic log measurements from a well in the subsurface of the White Rose Field, offshore Newfoundland. Two issues are examined in

these models. First, impermeable concretionary intervals observed in the well logs that impede the flow of hydrocarbons, are varied in vertical and lateral extent to evaluate the effectiveness of the cross-well seismic method for detecting these intervals. Second, a different stochastic velocity field is added to each of the models within the reservoir interval to simulate two end-member porosity variations: 1) long, high aspect ratio variations to represent porosity controlled by bedding, and 2) short, low aspect ratio variations to represent porosity controlled by diagenetic effects and influenced by fractures. All three velocity models contain reservoir features that are critical to the understanding of the corresponding reservoirs.

The three models are created to attempt representation of realistic reservoir scenarios. The first model is derived from reservoir analogue outcrops for both land and offshore reservoirs, while the second model is derived from subsurface offshore reservoir data. Acquisition of cross-well seismic data is more commonly done onshore then offshore, especially in the tar sands where numerous vertical wells are readily available at small distances from each other (Liu and West, 1998) (Paulsson, et al., 1994) (Khalil, et al., 1993). There are a limited number of studies concerning offshore cross-well seismic data acquisition (Sheline, 1998). Development wells are required as the source and receiver wells for offshore cross-well seismic acquisition because only these wells are close enough for cross-well seismic acquisition, whereas exploration wells tend to be spaced several kilometres apart. An issue using offshore development wells is that they tend to be deviated that complicates the arrangement of the wavefield components (P- and S-waves) arriving at the receivers. However, retrieving the correct components is

routinely done in VSP data, and should not be an issue with the cross-well seismic geometry. VSPs could provide a viable alternative to cross-well seismic surveys since only one well is required, but VSP data have a lower frequency content and less information than cross-well seismic data. Therefore, it is within reason to evaluate the cross-well seismic technique using offshore reservoir data to assess the benefits for interpretation and reservoir characterization.

Chapter 3

Cross-well Seismic Processing

3.1 Introduction

Cross-well seismic data has been proven as a viable resource for high resolution imaging of reservoir features, through acquisition of high frequency data directly at the reservoir level. Both sources and receivers are located in opposing boreholes avoiding near-surface effects, allowing the recording of high frequency data. The recorded data contains a more complicated suite of arrivals than those from other seismic techniques. Therefore, a more complex processing flow is required to produce reservoir images, which differs considerably from a conventional surface seismic processing flow and even a vertical seismic profile (VSP) processing flow.

The modern, full waveform, cross-well seismic data processing flow was developed by Lazaratos (1993) with extensive analysis on resolution issues. Following this thesis, papers were released on acquisition (Harris et al., 1995), wavefield separation (Rowbotham and Goulty, 1994) (Rector et al., 1994) (Rector et al., 1995), reflection imaging (Lazaratos et al., 1995), migration (Byun, et al., 2002), and technical difficulties (Lazaratos et al., 1993) (Byun, 1999). There are a limited number of case studies that demonstrate the cross-well seismic technique. Some examples are Sheline et al. (1998), Parra, et al. (1998), and Dong and Marion (2005), but the most extensive case study is a four part paper by Harris et al. (1995), Lazaratos et al. (1995), Rector et al. (1995), and Van Schaack et al. (1995).

This thesis utilizes a simplified version of the processing flow developed by Lazaratos (1993). The synthetic dataset for this study only records P-waves, removing the need to separate S-waves, which tend to scatter more then P-waves and have lower frequencies. Since this is a 2D acoustic modeling study the data isn't contaminated with incoherent noise, tube waves, and energy arriving out of the plane of the source and receiver well. Without these details a simplified processing flow is implemented consisting of data generation, wavefield separation, cross-well to CDP domain transformation, and transformation to incident angle domain (Figure 3.1). The processing is carried out using the VSP package in *ProMAX*® except for calculating the incident angles, which is performed by user-defined programs.

3.2 Data Generation

The synthetic cross-well seismic data are acquired using the 2D second-order acoustic finite difference modeling operation in *ProMax*®. The modeling routine creates a grid using a velocity model of rectangular grid points, through which a compressional wave is propagated from the source through each grid point to the receivers. As long as the grid points remain sufficiently close, rapid lateral velocity variations are easily accounted for (*ProMAX*® VSP Reference).

The finite difference modeling is one of the most compute intensive operations because of the high frequencies used to simulate cross-well seismic data. The run-time is extremely sensitive to the frequency parameter, which increases by 2^3 as the frequency is

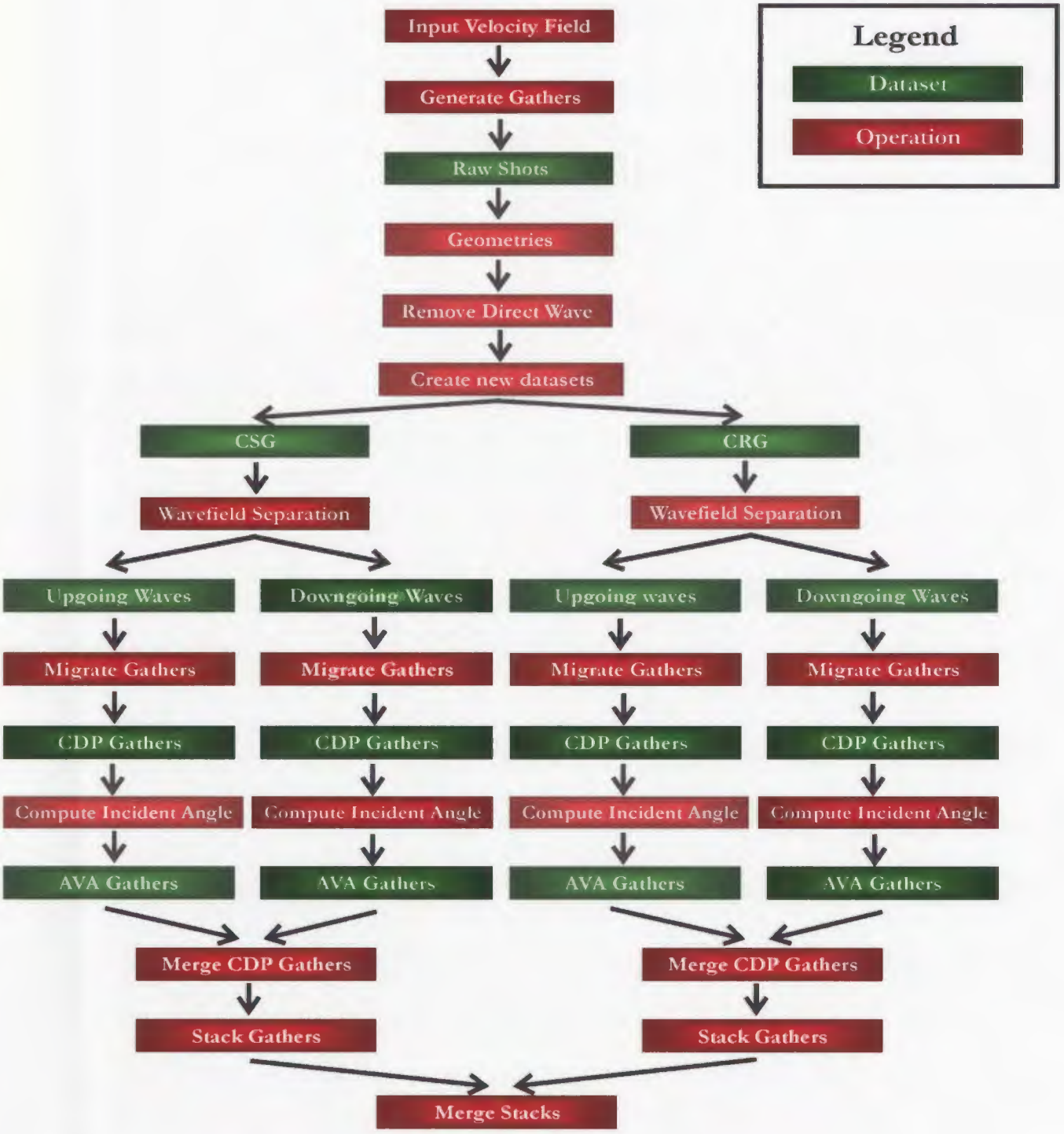

Figure 3.1: Cross-well seismic data processing flow used in this study.

increased, since the number of grid points doubles in the two spatial dimensions to avoid grid dispersion, and time sampling doubles to insure stability.

High frequencies are needed to adequately image small-scale heterogeneous variations and to avoid numerical noise, so smaller grid spacing is needed. A grid adjustment parameter is included so the criteria is satisfied, according to the *ProMAX®* VSP reference, that there should be an average of 7 grid points per wavelength, with an absolute minimum of 5, for the lowest velocity in the model at the peak frequency.

3.2.1 Model 1

The acquisition geometry for model 1 is displayed in figure 3.2. The survey is acquired through a velocity model that extended 280m vertically and 125m horizontally (figure 2.5). Sources are spaced 2m apart for a total of 140 shot locations, and the receiver spacing is 0.5m totaling 560 receivers. The source and receiver configurations are chosen to be practical, but also to avoid spatial aliasing. A zero phase Ricker source wavelet, with a peak frequency of 1000Hz and maximum of 3000Hz, is chosen so small scale variations incorporated into the model could be sampled, and is analogous to the frequencies obtained in previous studies. Energy released from each shot is recorded for 200ms using a 1000 CDP buffer on the edges of the velocity field to ensure strong reflections from the top of the model did not contaminate primary reflections. The velocity model is further adjusted by increasing the number of grid points per wavelength by 1.22 times to avoid numerical noise. Figure 3.3 displays a raw common shot gather and common receiver gather.

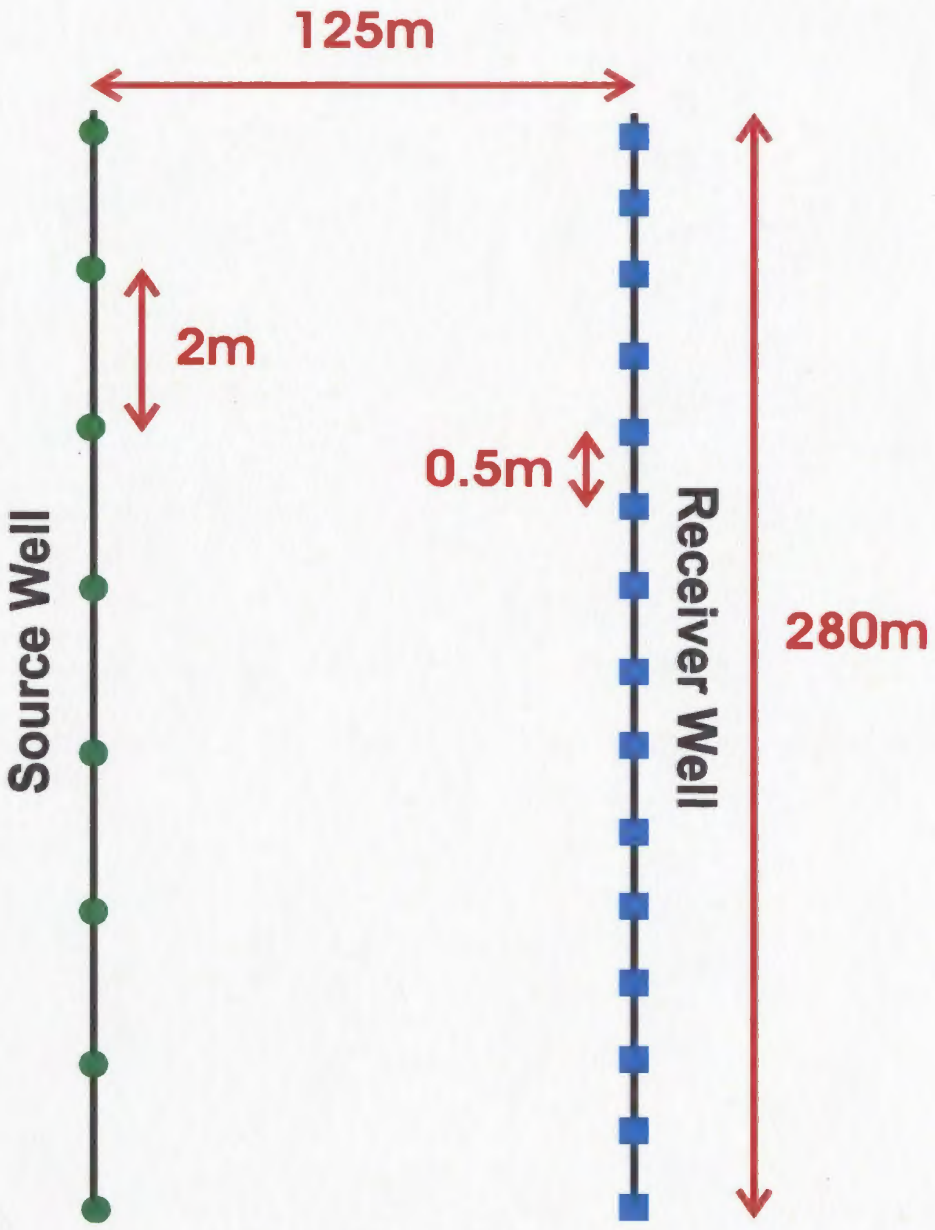

Figure 3.2: Schematic of acquisition geometry for model 1.

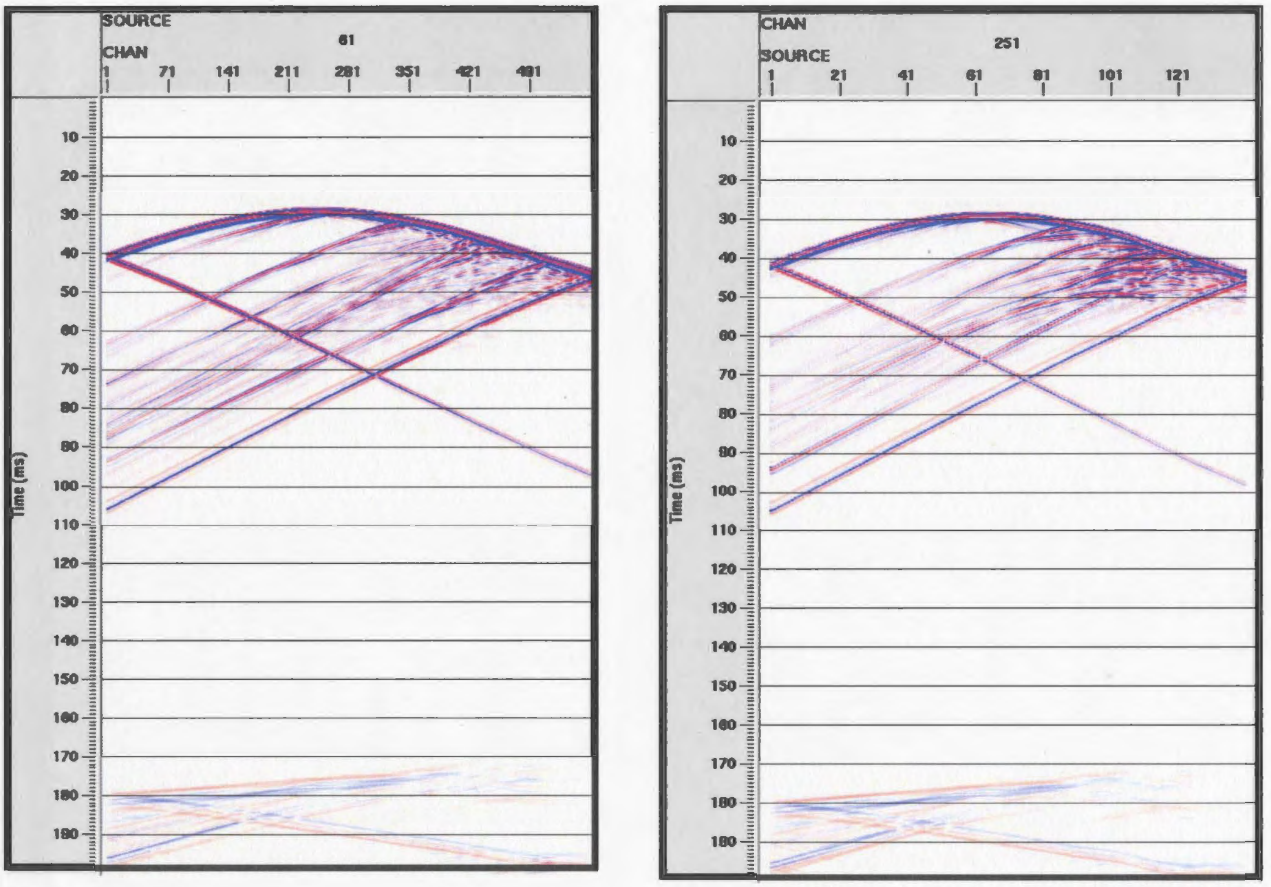

Figure 3.3: Example of a common shot gather (left) and common receiver gather (right) from model 1.

3.2.2 Models 2 and 3

Models 2 and 3 have identical parameterization throughout the processing flow, so they are presented together in the chapter, and only examples from model 2 are shown. The differences between models 2 and 3 are examined in Chapter 4.

Figure 3.4 shows the acquisition geometry to acquire surveys through models 2 and 3. The velocity models extend 250m vertically and 100m horizontally (figure 2.9a and 2.9b), and are finely sampled so a grid adjustment factor is not necessary. The survey geometry consists of 125 shots spaced 2m apart and 500 receivers spaced 0.5m apart. A zero phase Ricker source wavelet, with a peak frequency of 1000Hz and maximum of 3000Hz, is propagated for 200ms through the velocity models using a 1000 CDP buffer. A common shot gather and common receiver gather are displayed in Figure 3.5.

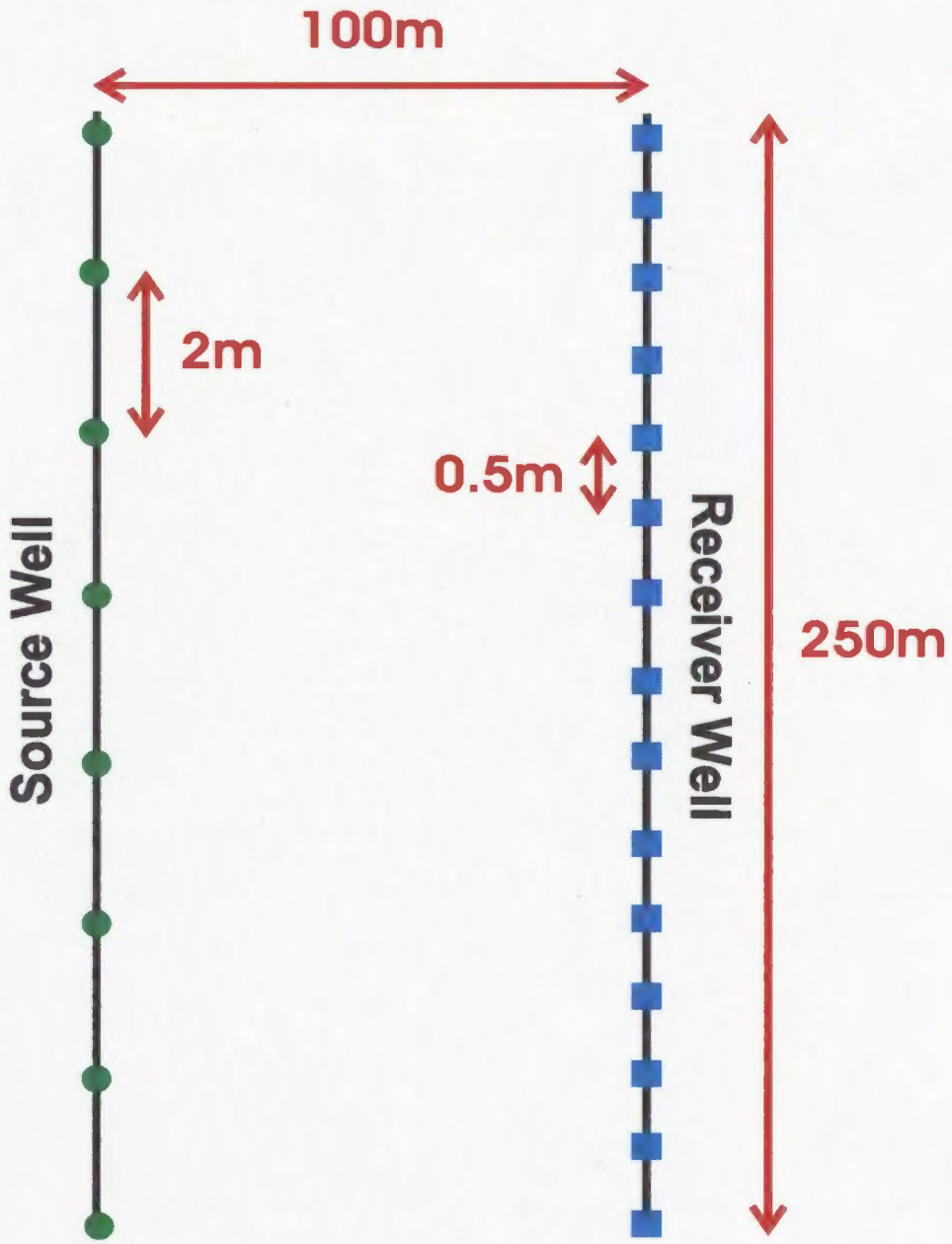

Figure 3.4: Schematic of acquisition geometry for models 2 and 3.

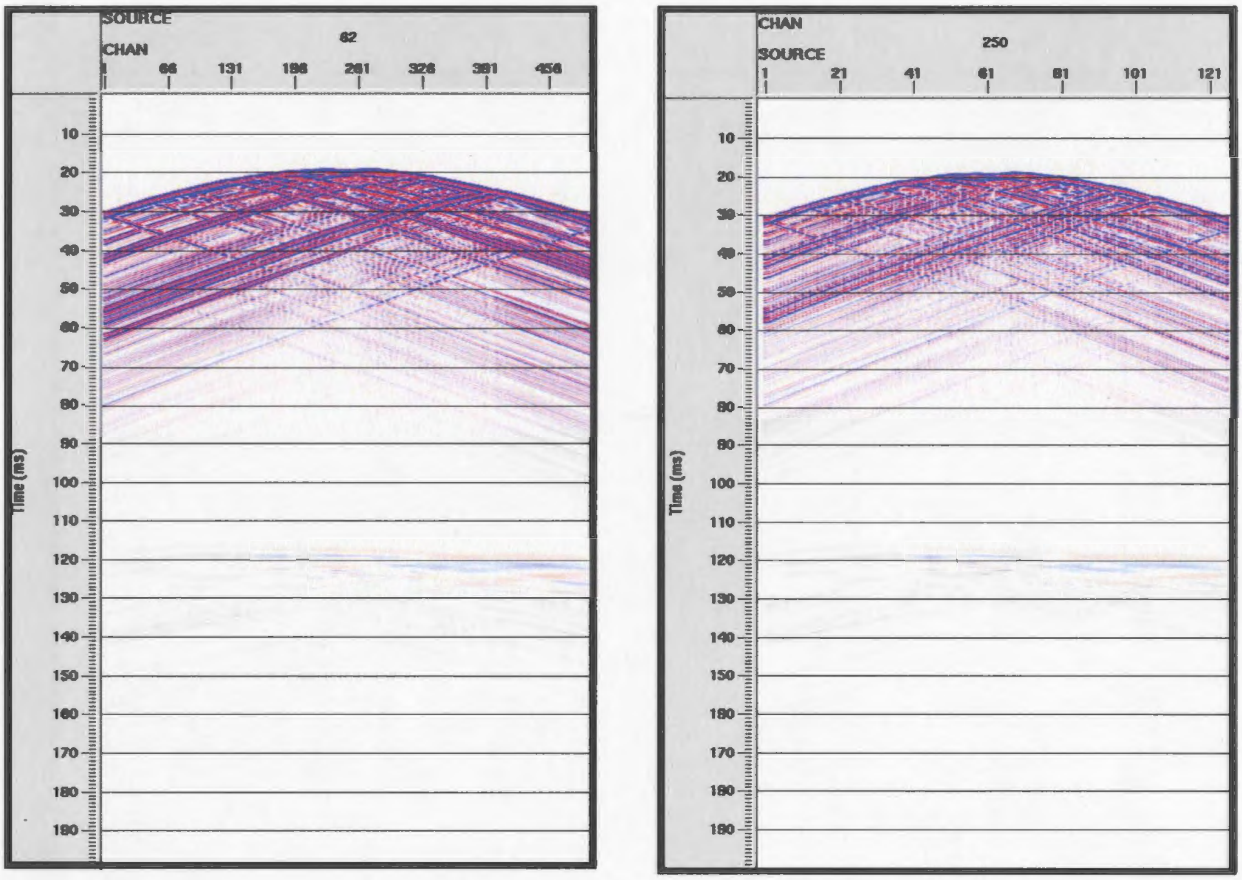

Figure 3.5: Example of a common shot gather (left) and common receiver gather (right) from model 2.

3.3 Wavefield Separation

The recorded wavefield contains different modes of energy propagation, comprised of direct waves, reflected waves, and multiples (figure 3.6). Direct waves travel across the region between the wells, and are refracted according to velocity variations. The reflected wavefield contains the information for imaging geological features between the boreholes. Reflections are recorded as upgoing waves from impedance contrasts located below the source, and downgoing waves from impedance contrasts located above the source. Within a visco-elastic or real dataset, the wavefield is complicated even further through conversions of P- and S- waves, but in this study only compression waves are used.

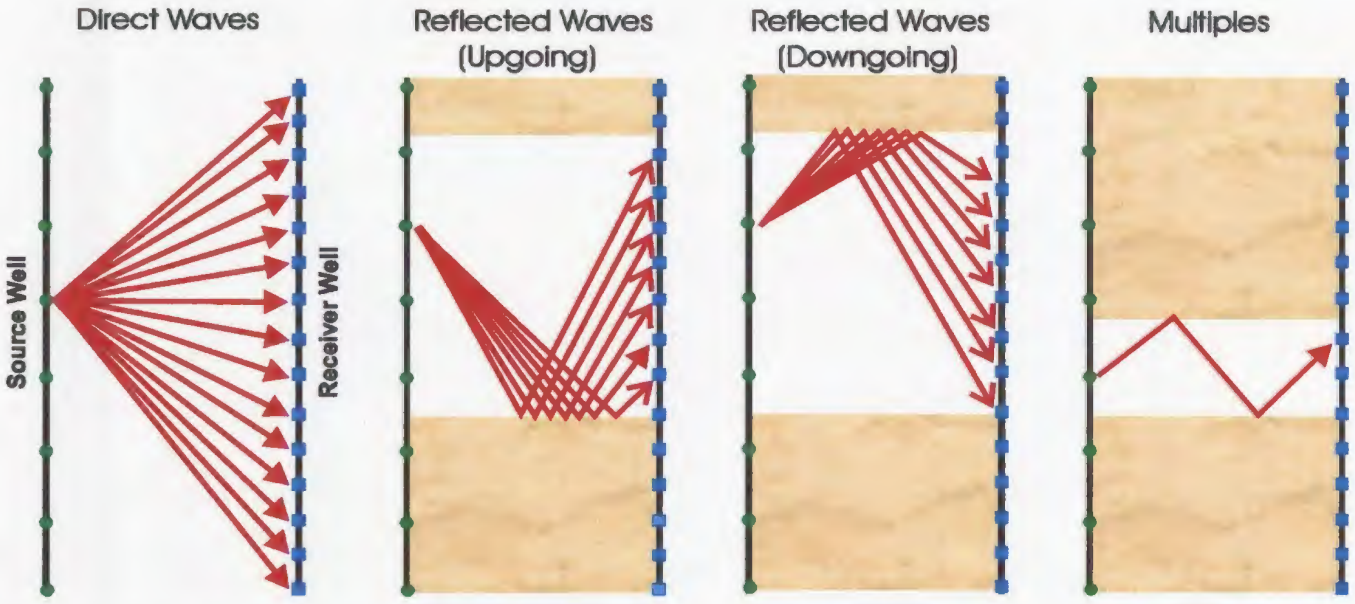

Figure 3.6: Schematic displaying the types of arrivals contained within the cross-well seismic data for this study.

With all the arrivals contained in the full wavefield, the first step before processing the data is to identify all the constituent modes followed by separation. Three sorting domains are used for identification and separation; common shot domain, common receiver domain, and common offset domain (offset refers to the difference in depth between shot and receiver (figure 3.7).

The first arrival removed is the direct wave as it is of no interest in this study. When working with real data however, the direct waves are needed to obtain an inter-well velocity field estimate through tomography, but in this case the velocity models are known.

The removal of direct waves in cross-well seismic data is more challenging then in surface seismic processing. In surface seismic data, reflections are normally sufficiently separated in time so direct waves can be muted, or the dip of direct waves are relatively constant and significantly different from reflections for removal with an F-K filter. Cross-well seismic data only records a few hundred milliseconds of data and with the complex suite of arrivals, interference occurs making muting undesirable. The removal of direct waves through F-K filtering is not practical because the apparent velocity of the direct wave velocity is continuously changing with different shot locations. The most effective domain to distinguish and separate the direct wave from reflections, and remove multiples, is the common offset domain (figure 3.8). In this domain direct waves and multiples have almost no moveout and reflections have twice the moveout compared to the other domains (Rector et al., 1994). These characteristics make the

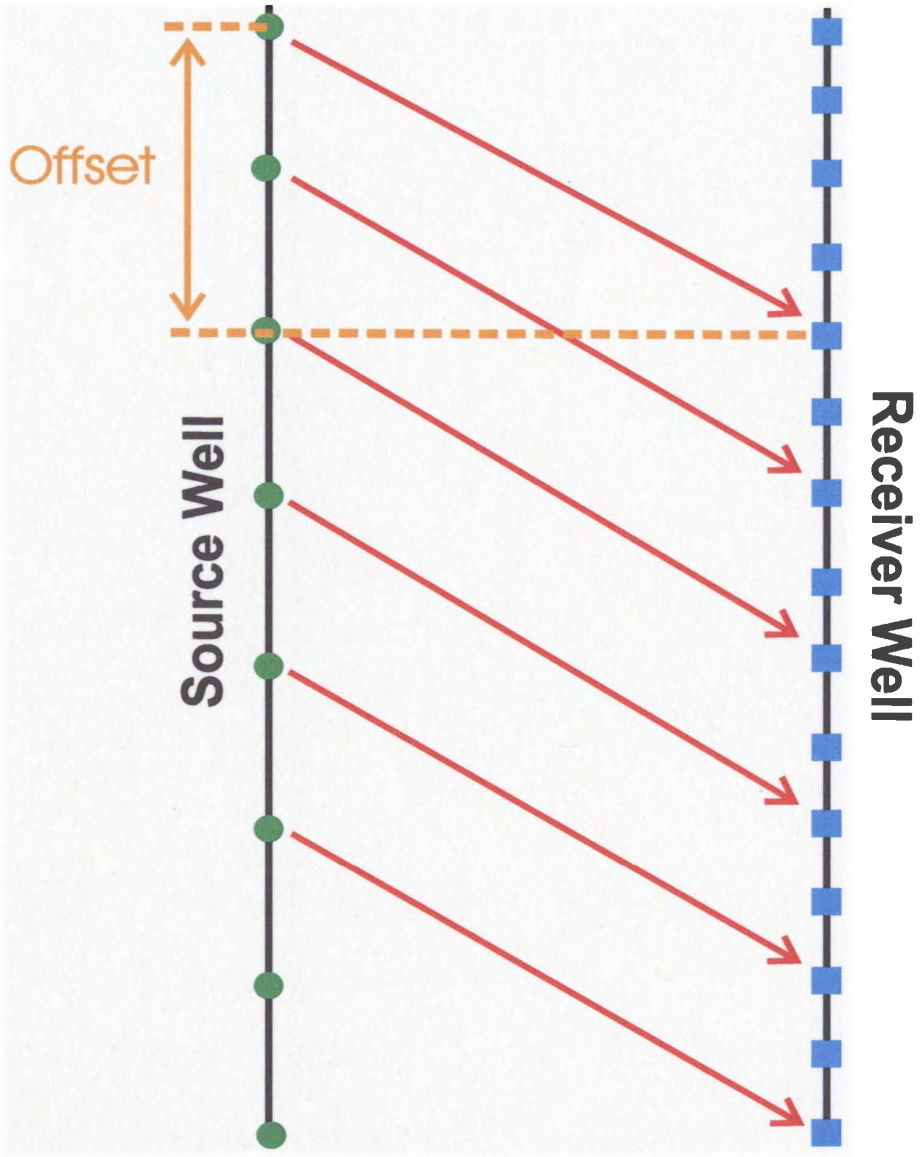

Figure 3.7: Schematic demonstrating the geometry of a common offset gather. Offset represents the vertical distance between source and receiver.

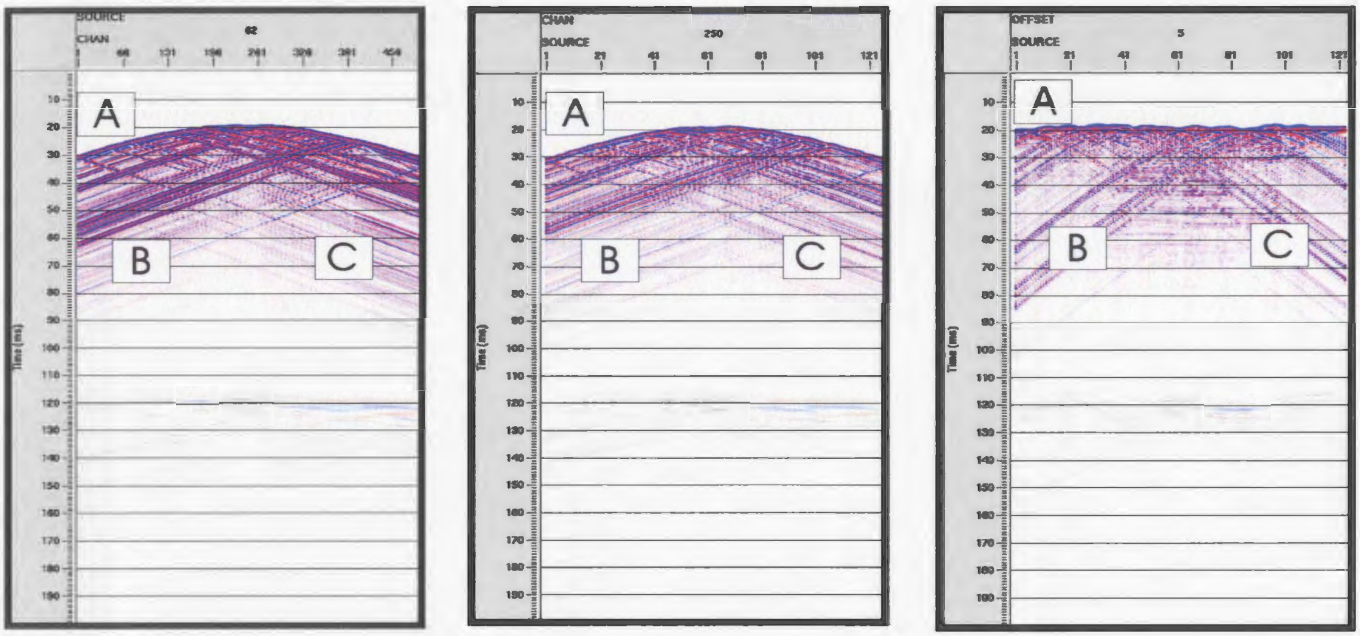

Figure 3.8: Example of a common shot gather (left) and common receiver gather (middle), and common offset gather (right), from model 2. The letters identify the arrival types; A) direct wave, B) upgoing reflected waves, C) downgoing reflected waves.

direct wave removal procedure in the common offset domain more effective then other sorting domains. Removing the direct wave involves,

1) Sorting data to common offset domain
2) Flattening the direct wave based on first break picks and normalizing each trace based on the RMS direct arrival amplitude.
3) Creating a mixed version of the dataset from step 2. The number of traces to mix depends on the longest wavelength of the reflections in the common offset domain, with the direct wave aligned.
4) Subtracting the two datasets in steps 2 and 3, and de-aligning the data.

Trace normalization in step 2, is not applied because normalization is required for shot energy variations, but shot energy is nearly constant for synthetic data.

Once the direct wave and multiples are removed common receiver gathers, along with common shot gathers, are created. The two datasets are needed for even distribution of reflection energy throughout the surveyed area. Common shot gathers sample features close to the receiver well and common receiver gathers sample features close to the source well (figure 3.9).

According to Rector et al. (1995), the next steps are attenuation of receiver well reflections and enhancement of source well reflections for common shot gathers, and vice versa for common receiver gathers. With real data these reflections would be substantially attenuated because of the complex wavefield, and reflections near the source well (or receiver well) have moveouts similar to the direct wave. However, with the limited wavefield and noise free data in this study, these reflections are still clearly visible even after removing the direct wave.

The separation of upgoing and downgoing waves within each of the two datasets using an F-K filter is the next stage. However, for the three surveys there are considerably fewer traces within a common receiver gather then a common shot gather, since there are more receivers then sources. Therefore, the common receiver gathers are spatially aliased prohibiting the two datasets from being filtered with the same frequency range in F-K space. Since the two datasets have to be later merged, the common receiver gathers are interpolated using the Beam-Steer Trace Interpolation to match the trace spacing of the common shot gathers. The Beam-Steer Trace Interpolation is a space-time adaptive signal analysis method for interpolating seismic traces (*ProMAX*® VSP Reference). The method uses an aperture of live traces that slides across the data,

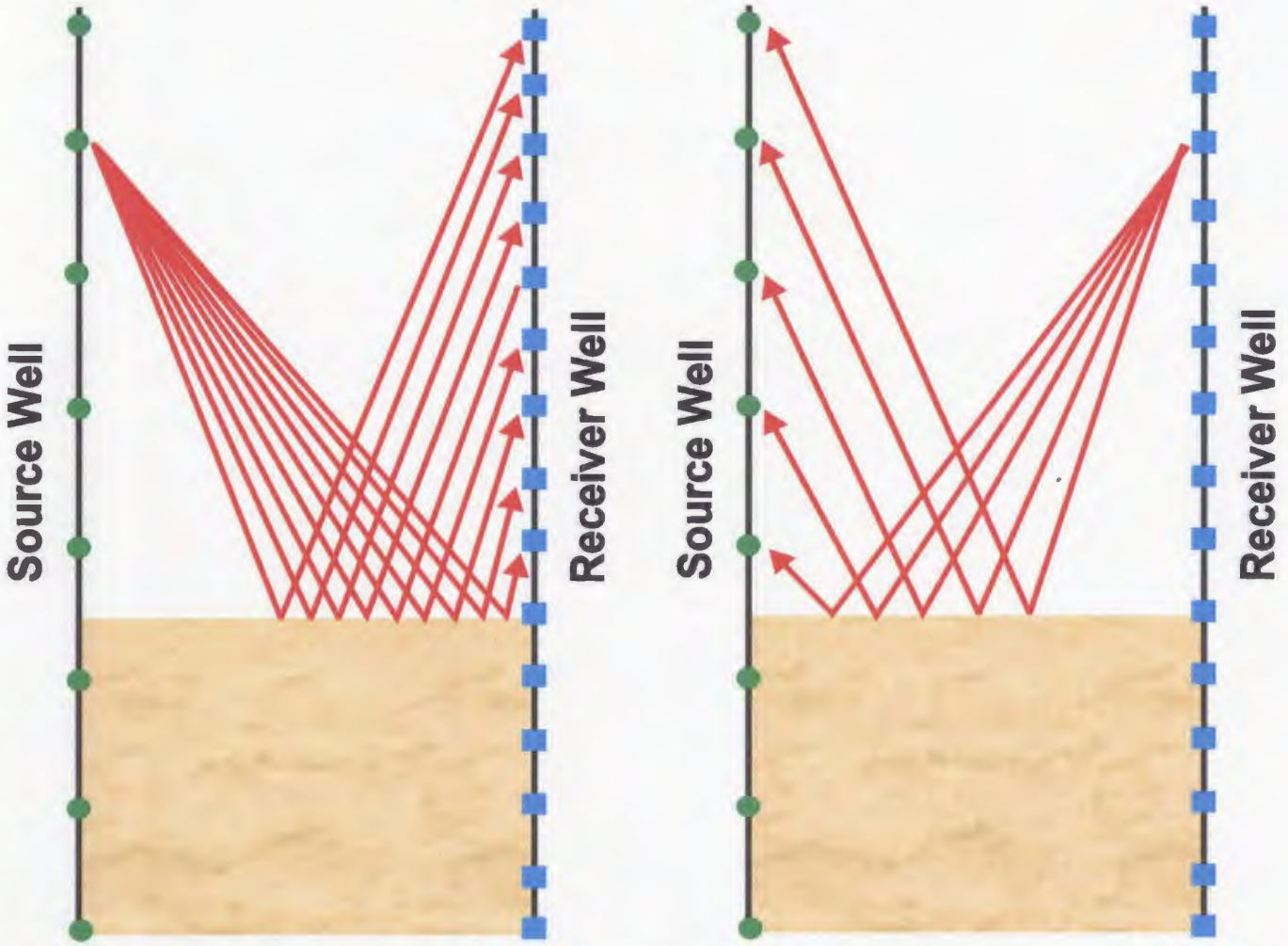

Figure 3.9: Schematic of the ray distribution for common shot gathers (left) and common receiver gathers (right). Notice how common shot gathers sample features close to the receiver well and common receiver gathers sample features to the source well.

interpolating between the traces along the way. There is a 50% overlap of the apertures, and traces are only interpolated using the inside half of the aperture. Interpolation is performed within the Tau-P domain where each transformed sample is weighted based on coherency measure. Other interpolation operations in *ProMAX*® were tried, such as the Fourier Interpolation and F-X Interpolation, but as shown in figure 3.10, the Beam-Steer Trace Interpolation produces the cleanest result.

Once interpolated so the common shot and receiver gathers have similar F-K spectrums, a F-K filter defined by a polygon in F-K space is applied to separate upgoing and downgoing waves.

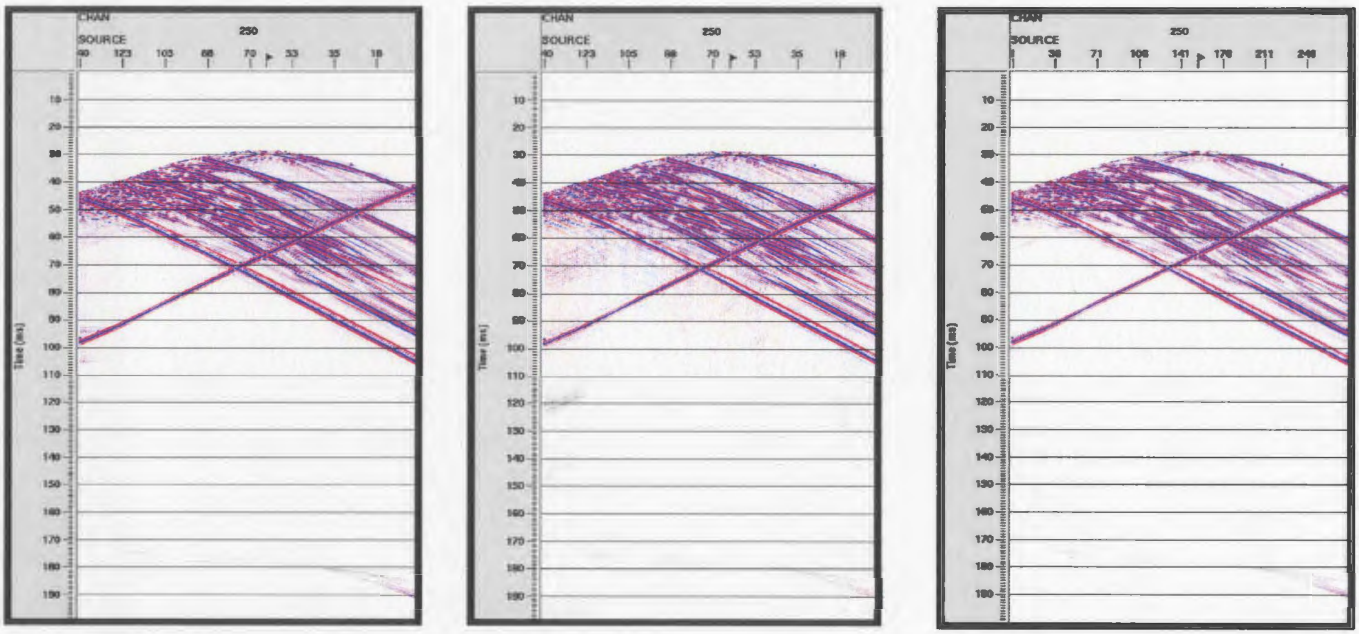

Figure 3.10: Interpolation test results from Fourier Trace Interpolation (left), F-X Trace Interpolation (middle), and Beam-Steer Trace Interpolation (right). The Beam-Steer Trace Interpolation produces the cleanest result.

3.3.1 Model 1

The removal of direct waves involves subtracting a 3-trace median mix common offset gather dataset, aligned according to the first breaks, from an unmixed aligned common offset gather dataset (figure 3.11). A 3-trace mix is chosen because the longest horizontal wavelength is determined to be 6m, measured from the reflection with the fastest velocity (Rector et al., 1995). A common shot gather with and without the direct wave and multiples is shown in figure 3.12.

Once the direct wave and multiples are removed, the common receiver gathers are created along with the common shot gathers. The FK spectra from a common shot and receiver gather are displayed in figure 3.13. The common receiver gather is noticeably aliased compared to the common shot gather, so the common receiver gathers are interpolated using the Beam-Steer Trace Interpolation from a 2m to 0.5m spacing to match the common shot gather trace spacing (figure 3.14). The FK spectra of the common shot and receiver gathers are now similar, allowing for upgoing and downgoing wavefield separation. Downgoing events are separated by accepting velocities greater then 4000m/s, with a maximum frequency of 3000Hz, and upoing events are separated by accepting events with velocities less then -4000m/s with the same frequency (figure 3.15). The two datasets are now prepared for transformation into the CDP domain.

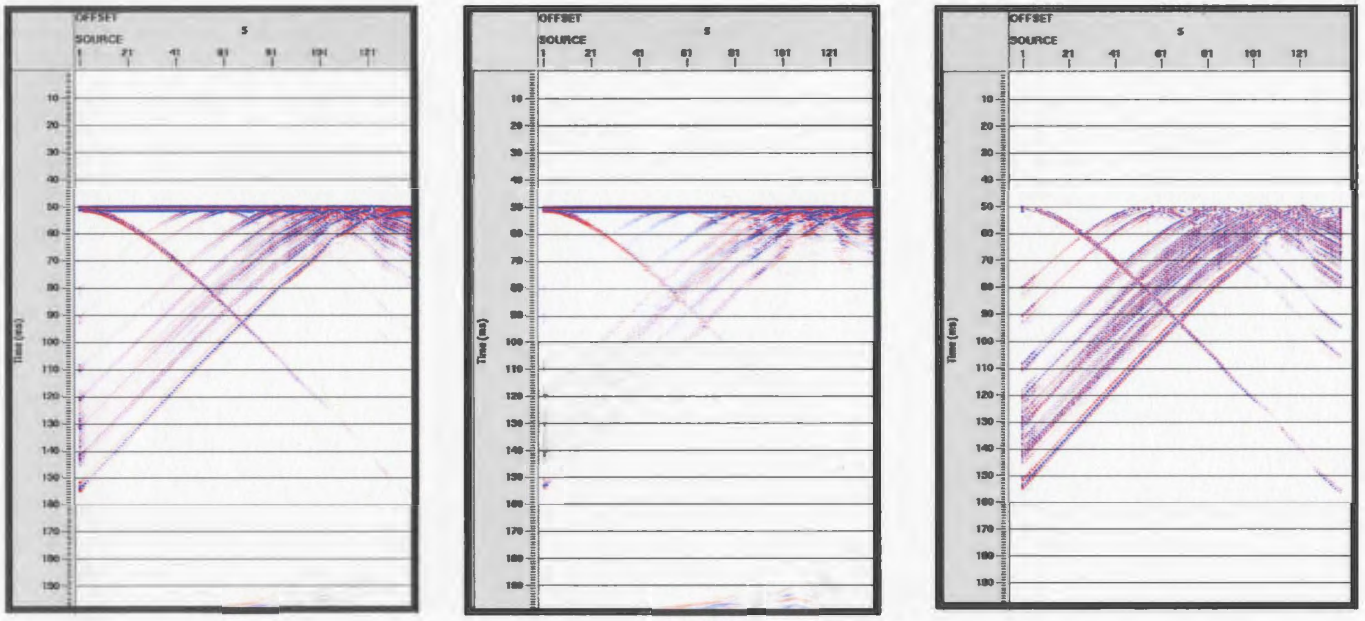

Figure 3.11: The datasets involved in removing the direct wave for model 1. The mixed dataset (middle) is subtracted from the unmixed dataset (left), resulting in a datasets with no direct wave (right).

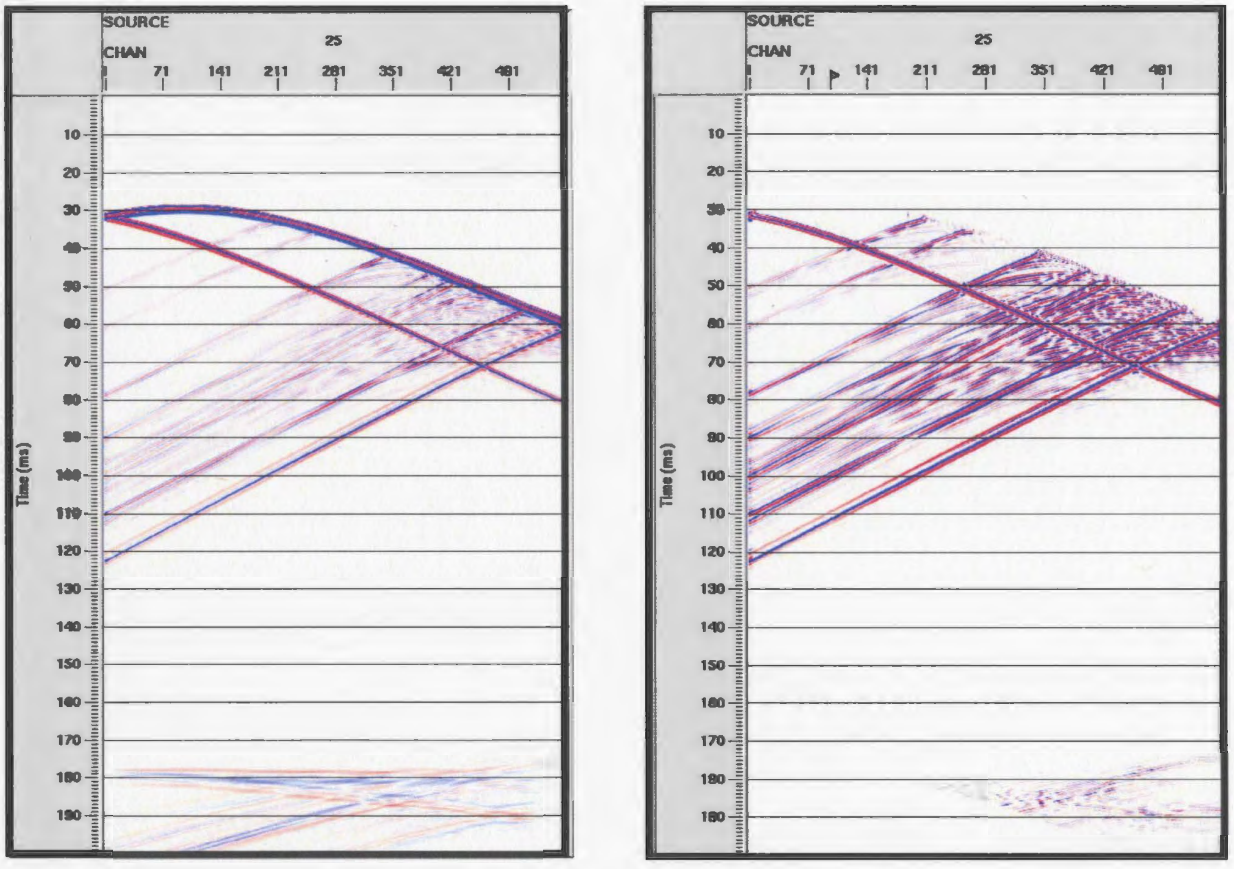

Figure 3.12: A common shot gather from model 1 with the direct wave (left) and without the direct wave (right).

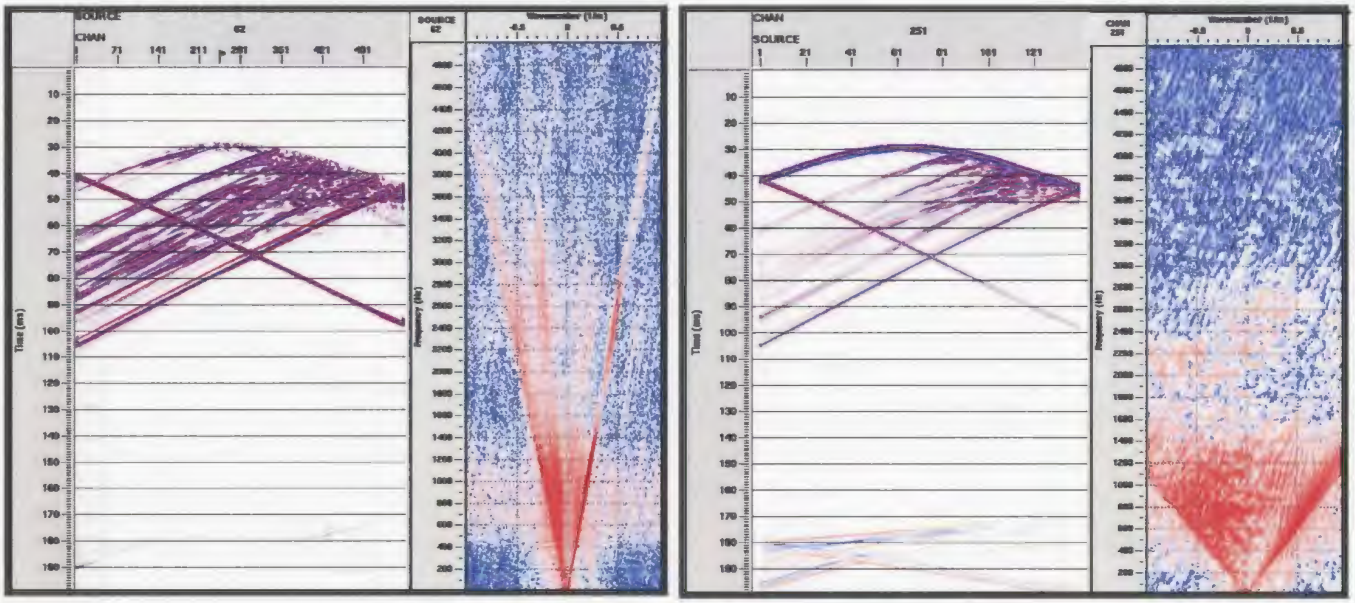

Figure 3.13: A common shot gather (left) and common receiver gather (right) with their respective F-K spectra for model 1.

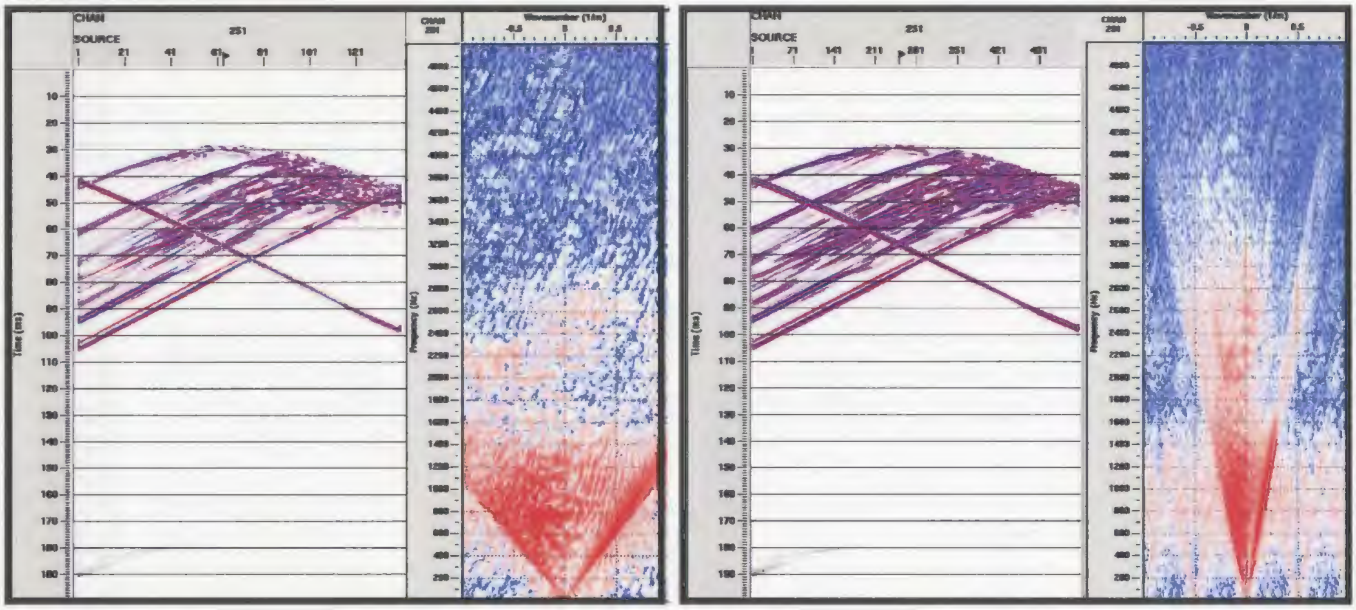

Figure 3.14: An uninterpolated (left) and interpolated (right) common receiver gather with their respective F-K spectra. The gathers are interpolated from a 2m to 0.5m trace spacing.

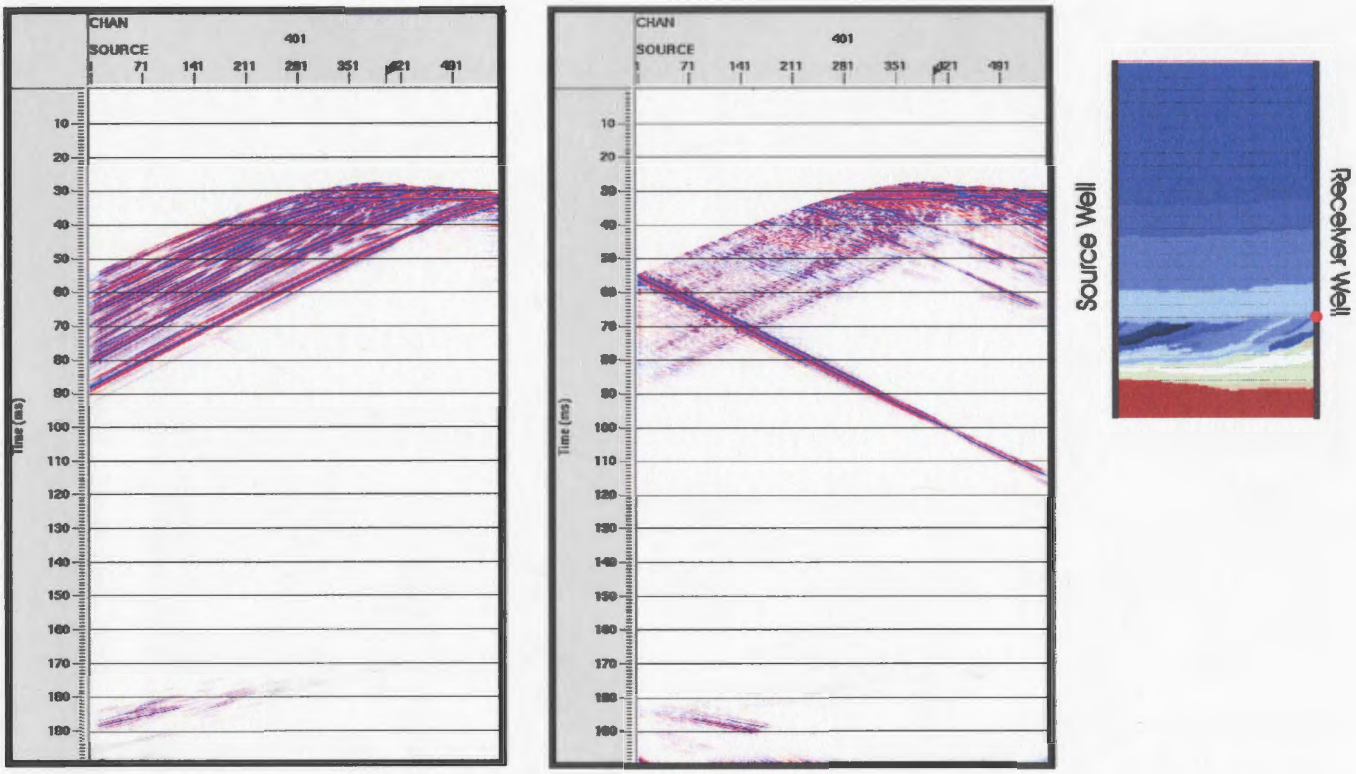

Figure 3.15: Separated upgoing (left) and downgoing (right) reflections of a common receiver gather from model 1. Red dot on velocity model displays location of common receiver gather.

3.3.2 Models 2 and 3

The removal of direct waves consisted of a 5-trace median mix dataset (longest horizontal wavelength is 8m) subtracted from the unmixed dataset, both sorted in the common offset domain and aligned according to the first break picks (figure 3.16). The resulting dataset is de-aligned and sorted back into the common shot domain (figure 3.17).

Next, the common receiver gathers are created and interpolated from 2m to 0.5m trace spacing to avoid aliasing and match the trace spacing of the common shot gathers (figure 3.18). An F-K filter is then applied to both datasets, using a velocity greater than 3500m/s to capture the downgoing waves, and velocities less than -3500m/s to capture the upgoing events, both using a maximum frequency of 3500Hz (figure 3.19). Upgoing and downgoing datasets are now prepared for transforming to the CDP domain.

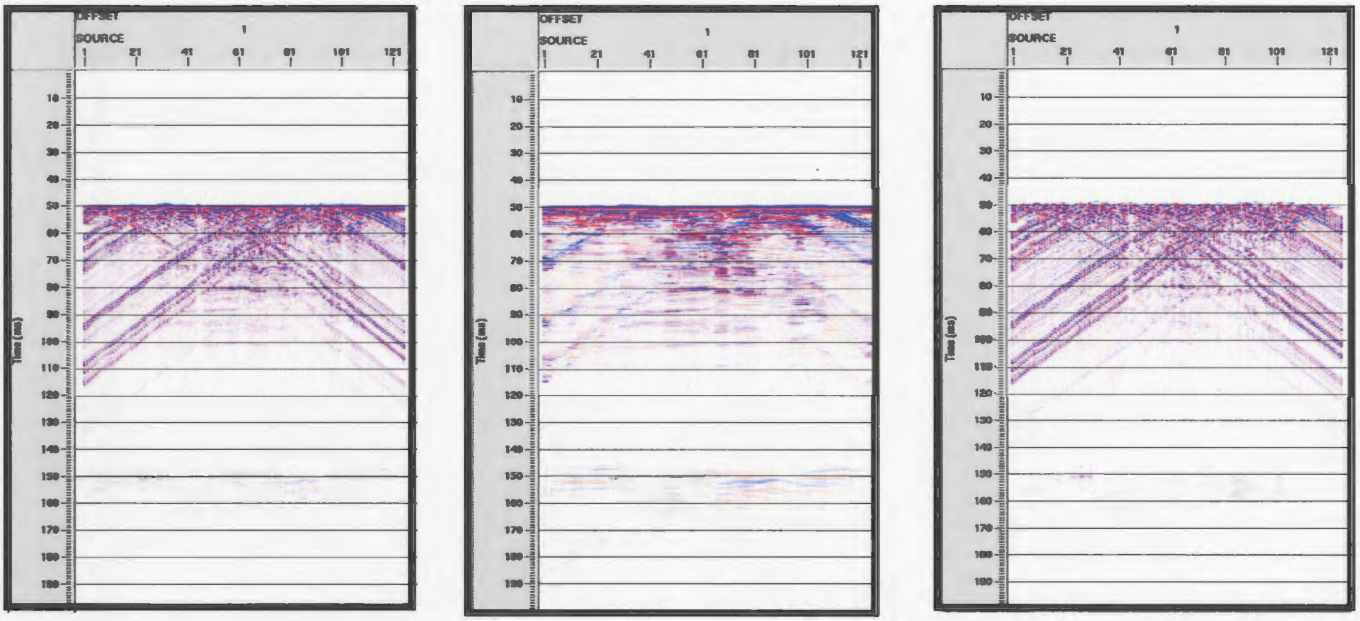

Figure 3.16: The datasets involved in removing the direct wave from model 2. The mixed dataset (middle) is subtracted from the unmixed dataset (left), resulting in a datasets with no direct wave (right).

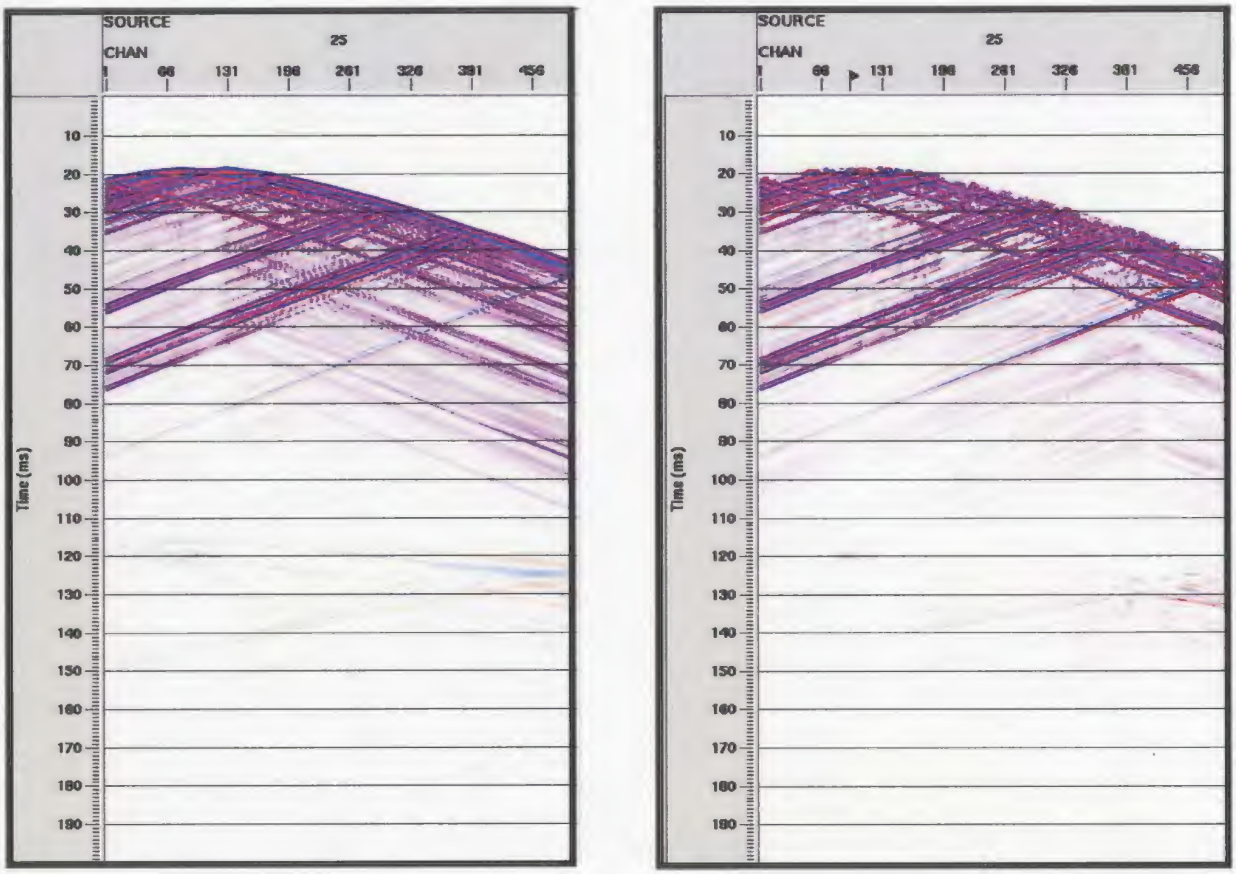

Figure 3.17: A common shot gather from model 2 with the direct wave (left) and without the direct (right).

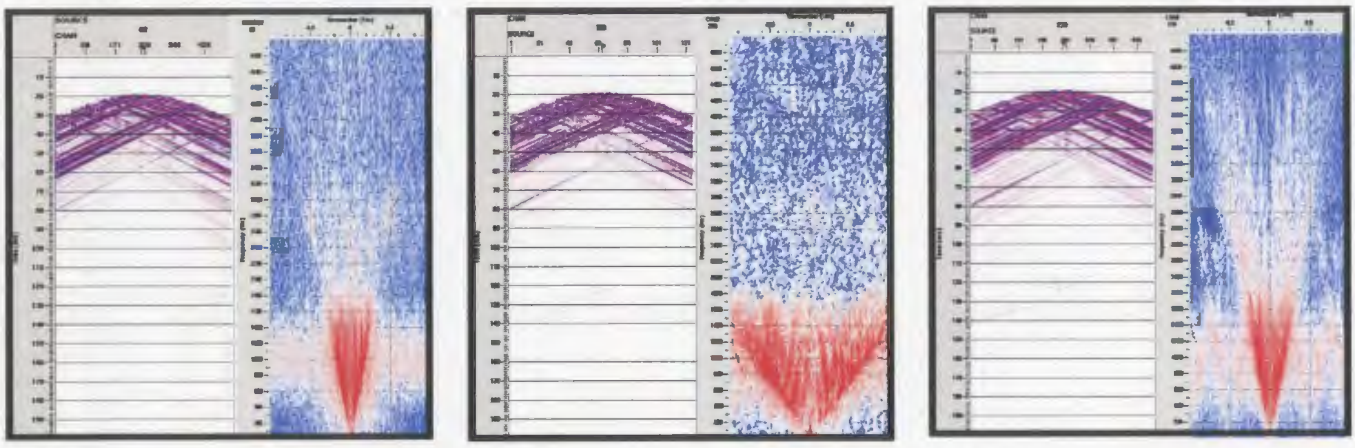

Figure 3.18: A common shot gather (left), a common receiver gather (middle), and a common receiver interpolated from 2m to 0.5m trace spacing (right), all displayed with their F-K spectra.

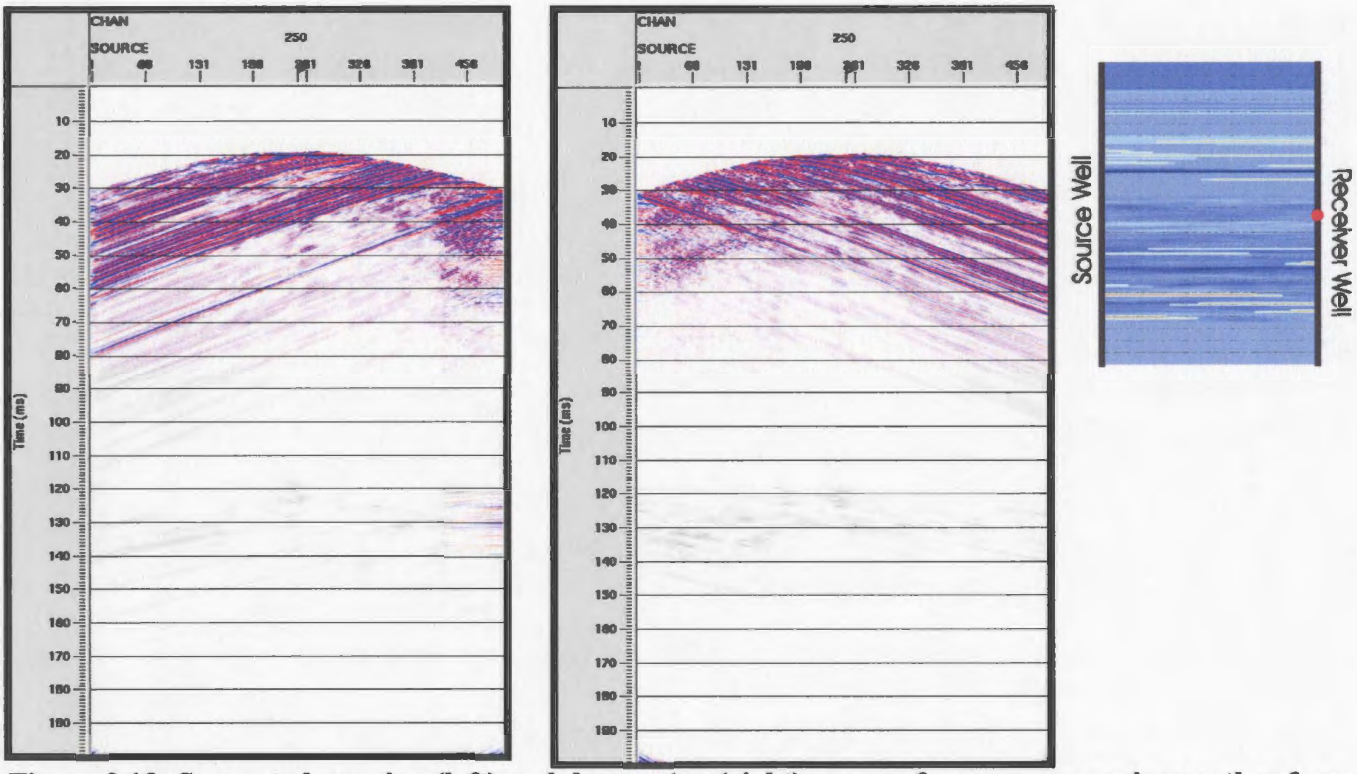

Figure 3.19: Separated upgoing (left) and downgoing (right) waves of a common receiver gather from model 2. Red dot on velocity model displays location of common receiver gather.

3.4 Cross-well domain to CDP domain transform

The four datasets in the cross-well domain have little physical meaning because the data in its present state cannot be used to produce an image of the subsurface. The data requires transformation to the common depth point domain (CDP), where the data can be stacked to produce a subsurface image. Previous studies have used the VSP-CDP mapping technique, which is a point-to-point transformation that transfers each point in the cross-well domain to a point in the CDP domain (Lazaratos, 1993).

For this study, the mapping routine is not used, but the VSP Kirchhoff migration in *ProMAX*® is used instead. The migration computes the depth between the source and receiver well at which a reflection occurs by computing traveltime maps that relate the time, amplitude, arrival angle of a ray at the point, and takeoff angle of the ray at its origin for each source and receiver to each subsurface point (*ProMAX*® VSP Reference). Traveltime maps are created by calculating the traveltimes from each source (or receiver) to each receiver (or source) through a velocity field using maximum amplitude raytracing. This means that if a point in the subsurface is sampled by more then one arrival, then the traveltime with the maximum amplitude is used (*Promax*® VSP Reference). The VSP Kirchhoff Migration is parameterized to mimic a point-to-point transformation by limiting the migration aperture to almost zero (+/- 0.5m). Instead of the energy spreading out over an ellipse, the energy is concentrated at the computed position in the subsurface from the traveltime maps (Figure 3.20). For a detailed description of the theory behind the wave-field extrapolation and imaging principle see Dillon (1988).

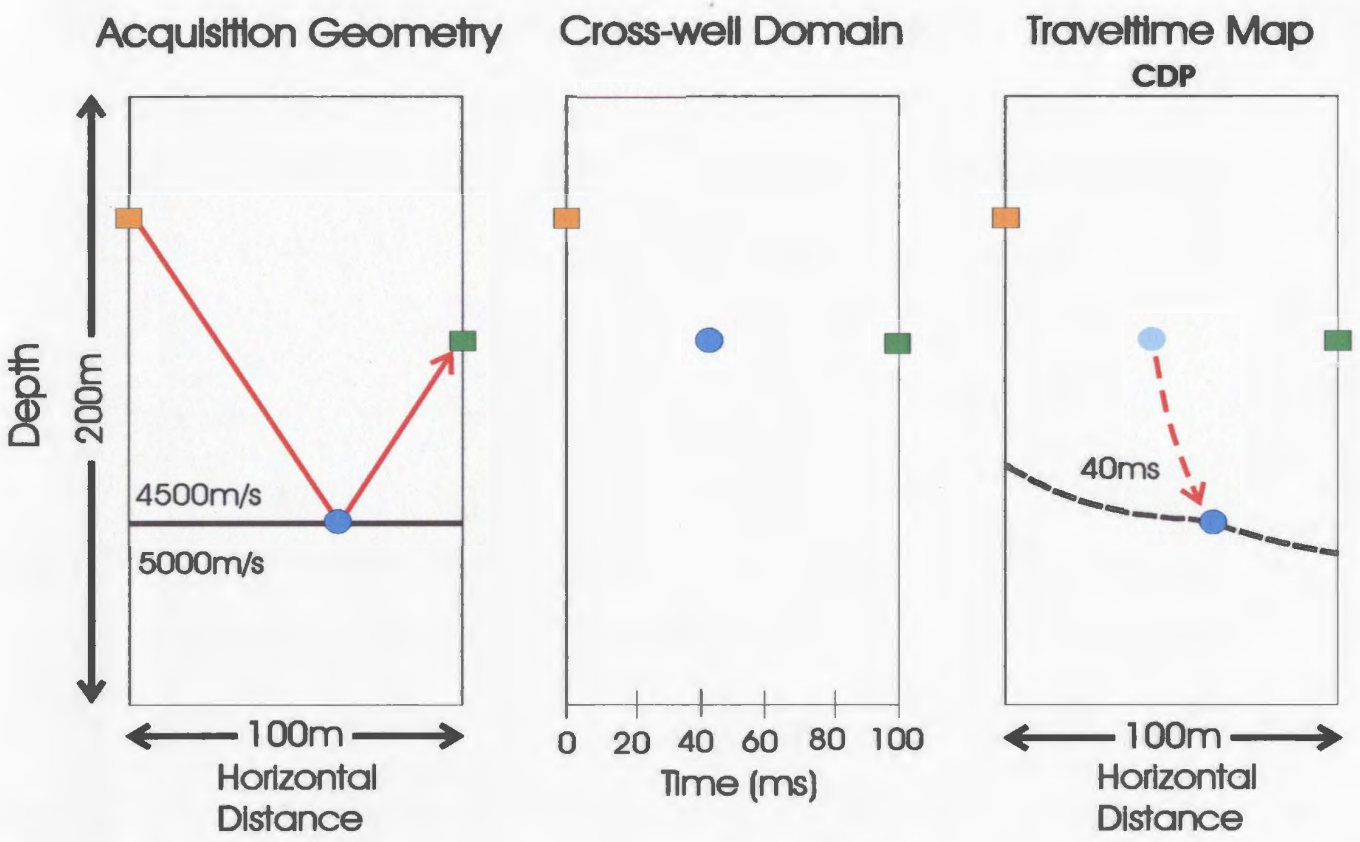

Figure 3.20: Schematic diagram showing the raypath for a reflection point in a cross-well survey (left), the reflection point's corresponding position in the cross-well domain (middle), and the traveltime isochron within the traveltime map for the combined source and receiver traveltimes, which the reflection point is mapped onto at the appropriate CDP. Source location is displayed in orange, receiver location in green, and reflection point in blue.

There are a couple advantages to using a migration over the VSP-CDP mapping technique. The migration does not require an estimate of the dip to image dipping reflectors, whereas the VSP-CDP mapping does. If the dip differs from the true dip during mapping, then samples can be mapped to an incorrect spatial location.

The mapping routine also induces a wavelet stretch, similar to NMO stretch, on the data during transformation, since mapping is essentially a global stretch to the data (Lazaratos, 1993). Migration does not cause wavelet stretch, hence improving resolution. Both

techniques, however, are limited in their lateral resolution because of their inability to collapse the Fresnel zone (Appendix A).

The VSP Kirchhoff migration of the upgoing and downgoing, shot and receiver gathers (four datasets) is executed in an unconventional fashion. Normally, the whole dataset is input into the VSP Kirchhoff Migration operation and the result is a complete, stacked depth section, but in this study individual shot and receiver gathers are migrated separately. Both methods produce the same result, but quality control is improved if shots and receiver gathers are migrated individually. CDP gathers can be generated by resorting the migrated gathers by CDP location and shot (or receiver) location, which allows for removal of unwanted energy such as incoherent energy. CDP gathers can also be transformed into amplitude vs. angle (AVA) gathers, through computing the incident angle, to determine the angles that are incorporated into the stack. Incident angle computation is discussed more in the next section.

Only certain shot and receiver gathers from each of the four datasets are chosen for migration. For the upgoing shot and receiver datasets, only shot and receiver locations within the top half of the section are migrated, and only shot and receiver locations within the bottom half of the survey are migrated for downgoing shot and receiver datasets. Gathers are not migrated because shot or receiver locations of upgoing gathers image fewer reflectors as they increase in depth (decrease in depth for downgoing gathers) and unwanted wide angle reflections are produced.

3.4.1 Model 1

A list of the migrated shot and receiver gathers is displayed in Table 3.1. Since the heterogeneous zone is located at the bottom of the velocity model, the migration effort is concentrated on the upgoing shot and receiver gathers. An example of an upgoing common receiver gather transformed to the CDP domain is displayed in figure 3.21. Once all the gathers are migrated, they are merged together and sorted based on CDP and shot or receiver within each of the four separate datasets.

These gathers are now ready to be transformed to AVA gathers, but the following steps can be used to produce a preliminary stack. The migrated common shot and receiver gathers each have an upgoing and downgoing component, which need to be merged together. First a 180° phase shift between the upgoing and downgoing components is corrected for, and then they are merged together (figure 3.22). A merged dataset now exists for the migrated common shot gathers and one for the migrated common receiver gathers. These two datasets are stacked separately, and then the two stacked sections are merged together creating a complete stacked section (figure 3.23).

Dataset	Shot or Receiver Gathers Migrated	Depth of Shot or Receiver Gathers Migrated (m)
Upgoing Common Shot Gathers	1 – 90 (1)	0 – 178 (2)
Downgoing Common Shot Gathers	91 – 140 (1)	180 – 278 (2)
Upgoing Common Receiver Gathers	1 – 401 (2)	0 – 200 (1)
Downgoing Common Receiver Gathers	301 – 559 (2)	150 – 279 (1)

Table 3.1: The shot and receiver gathers chosen to be migrated and the depth of each gather for upgoing and downgoing, shot and receiver gathers for model 1.

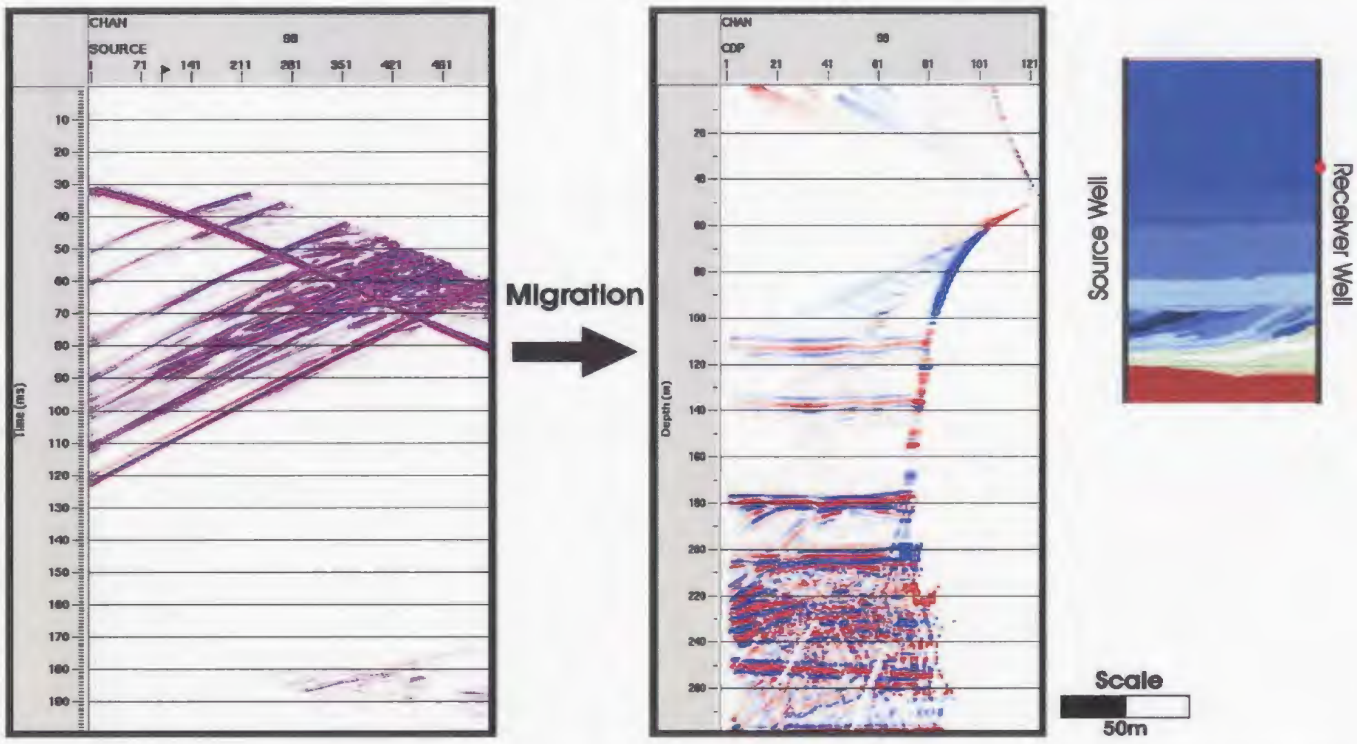

Figure 3.21: A common receiver gather and the result when the VSP Kirchhoff Migration is applied, from model 1. Red dot on velocity model displays location of common receiver gather.

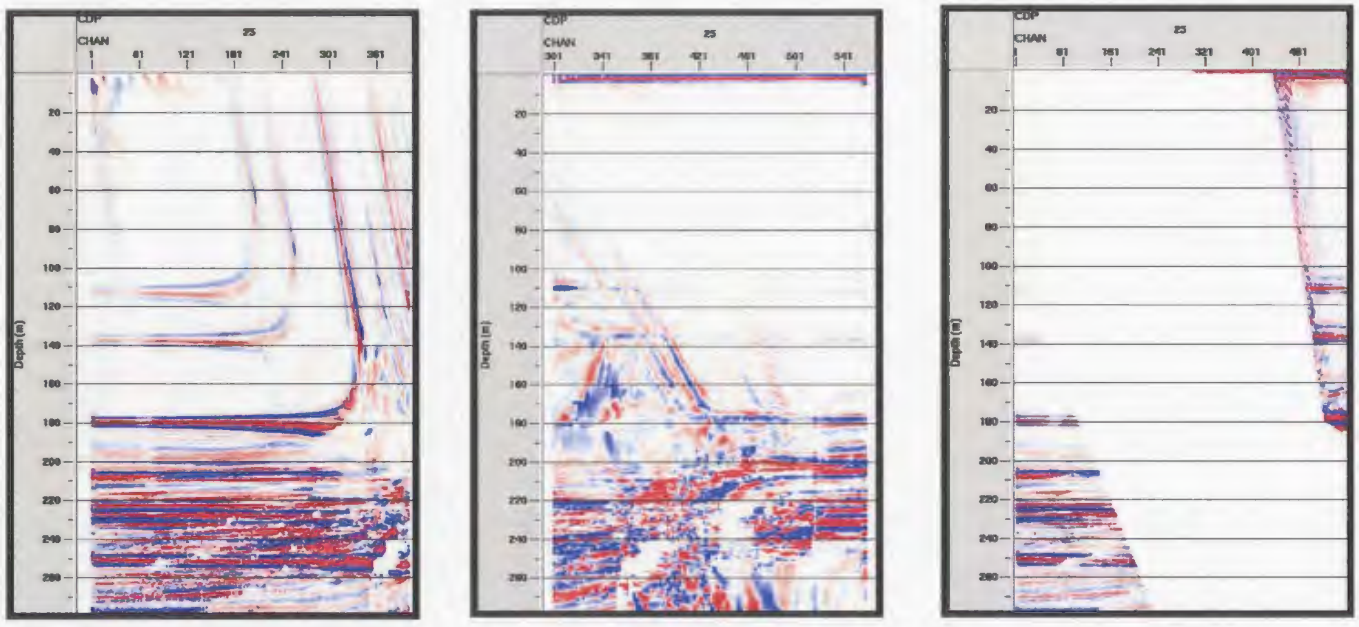

Figure 3.22: Migrated upgoing (left) and downgoing (middle) gathers and the merged result (right) from model 1. Before the datasets were merged the two datasets were muted to remove noise.

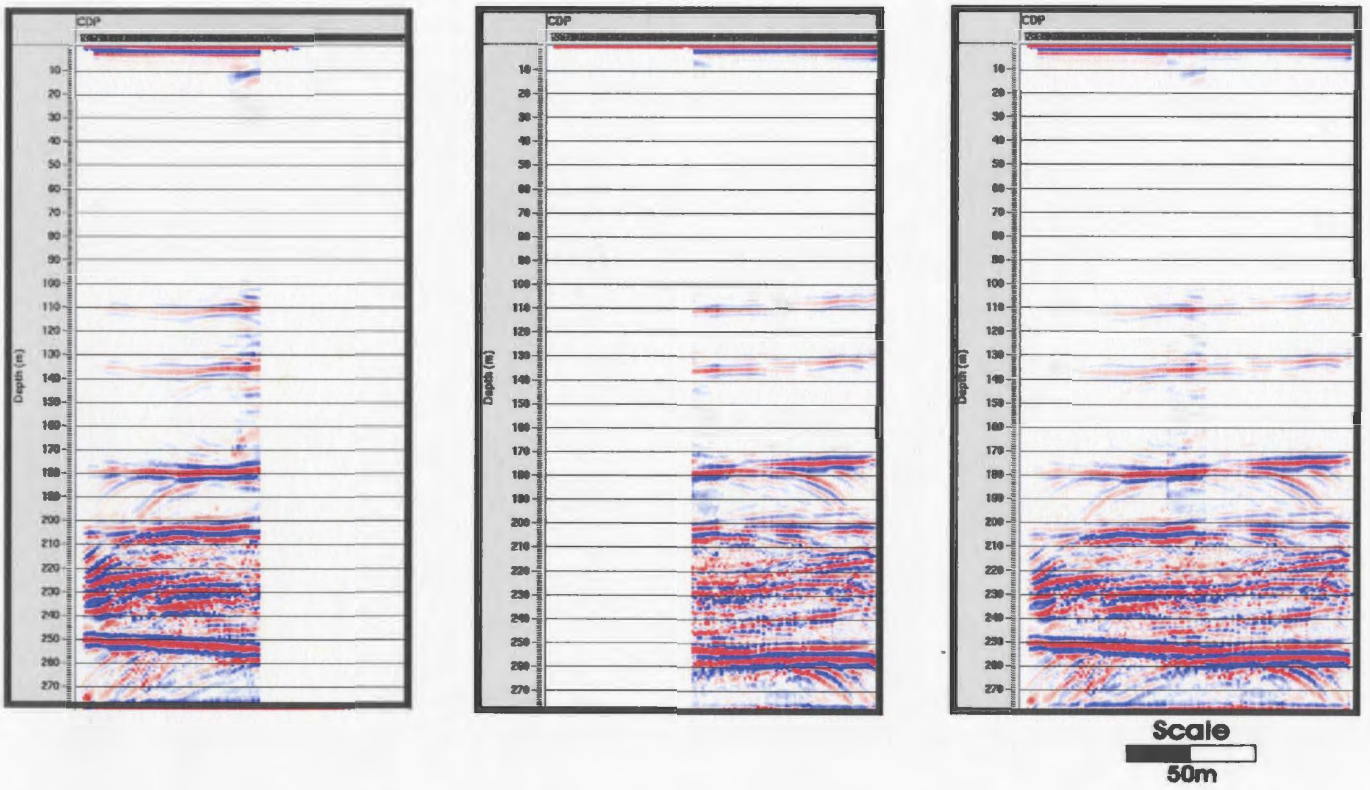

Figure 3.23: A stack of the migrated common receiver gathers (left), a stack of the migrated common shot gathers (middle), and the two stacks merged together (right) of model 1.

3.4.2 Models 2 and 3

The gathers for these models are migrated using a smooth version of the velocity field used for generating the original synthetic dataset. The velocity field is decimated from a 0.25m x 0.25m to a 2 x 2m grid (figure 3.24), producing a smooth velocity field more realistic to a tomographic result used in real data studies. By using a smoothed velocity field the computation time is significantly reduced, with minimal differences in data quality from tests using an unsmoothed velocity field.

Migration is performed on the gathers listed in Table 3.2. An example of an upgoing common receiver gather transformed to the CDP domain is displayed in figure 3.25. The gathers are now ready for calculation of the incident angles, but the same steps are taken here as in model 1 to create a preliminary stack. The gathers are merged together (figure 3.26), the individual migrated common shot and receive gathers are stacked, and the stacks are merged together figure 3.27.

Dataset	Shot or Receiver Gathers Migrated	Depth of Shot or Receiver Gathers Migrated (m)
Upgoing Common Shot Gathers	1 – 63 (increment 1)	0 – 134 (increment 2)
Downgoing Common Shot Gathers	64 – 125 (increment 1)	136 – 250 (increment 2)
Upgoing Common Receiver Gathers	1 – 249 (increment 2)	0 – 124 (increment 1)
Downgoing Common Receiver Gathers	251 – 499 (increment 2)	126 – 250 (increment 1)

Table 3.2: The shot and receiver gathers chosen to be migrated and the depth of each gather for upgoing and downgoing, shot and receiver gathers for models 2 and 3.

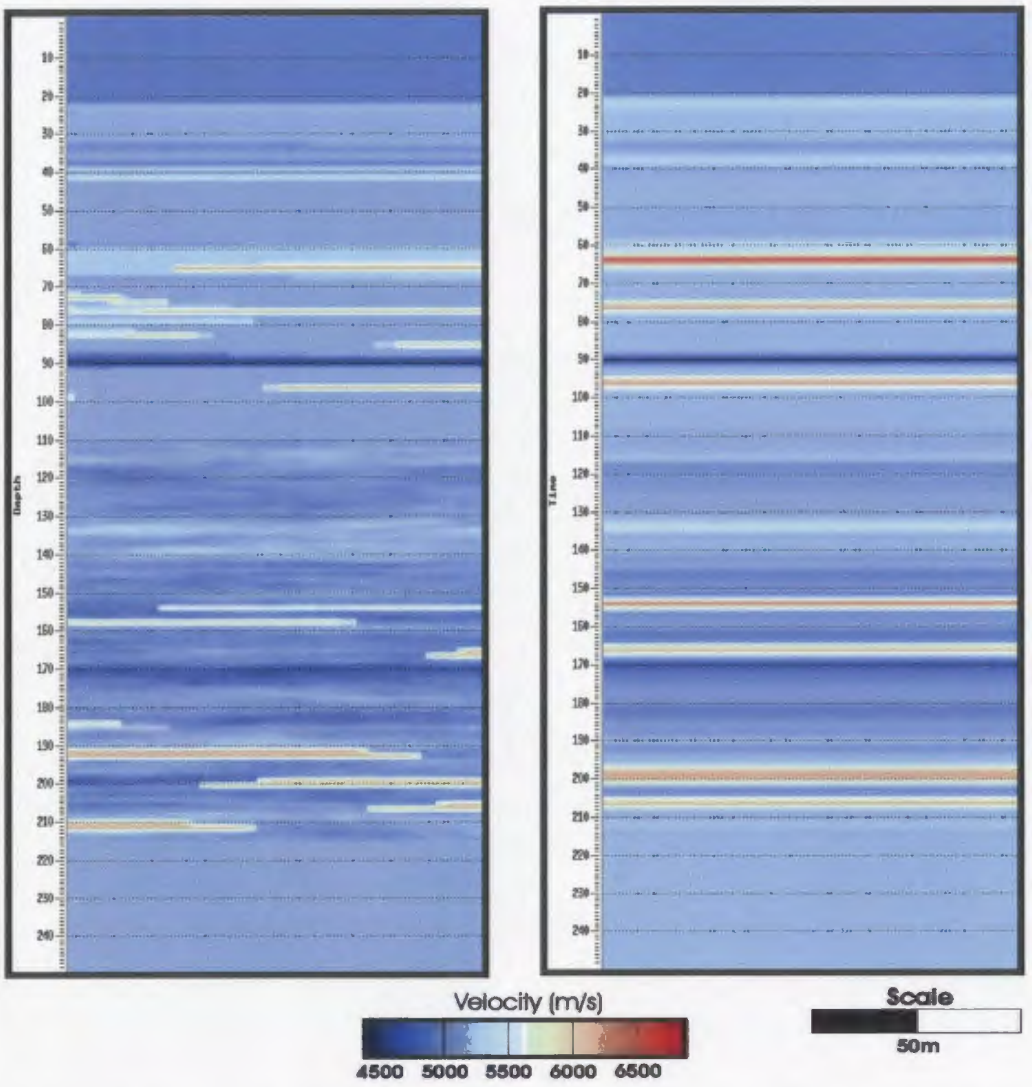

Figure 3.24: Before (left) and after (right) smoothing the velocity field for migration for model 2.

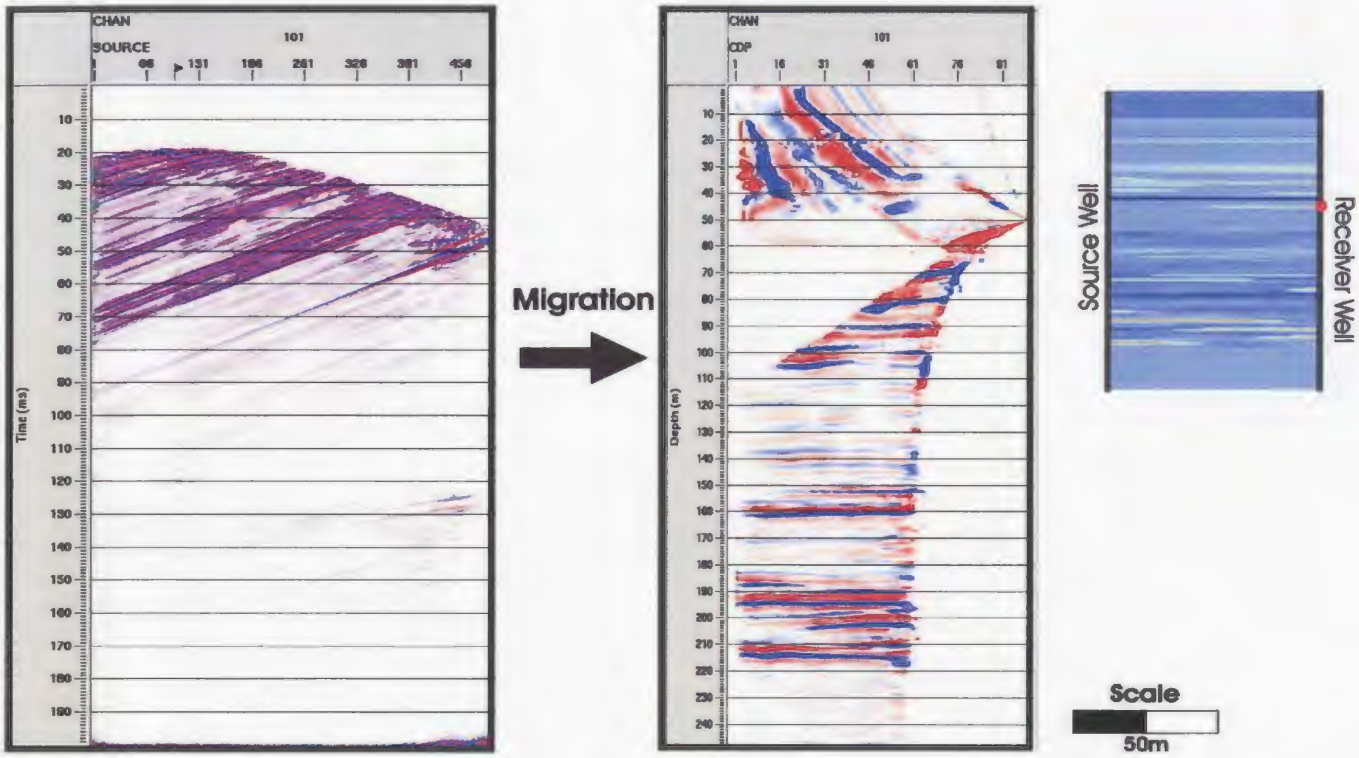

Figure 3.25: A common receiver gather and the result when the VSP Kirchhoff Migration is applied, from model 2. Red dot on velocity model displays location of common receiver gather.

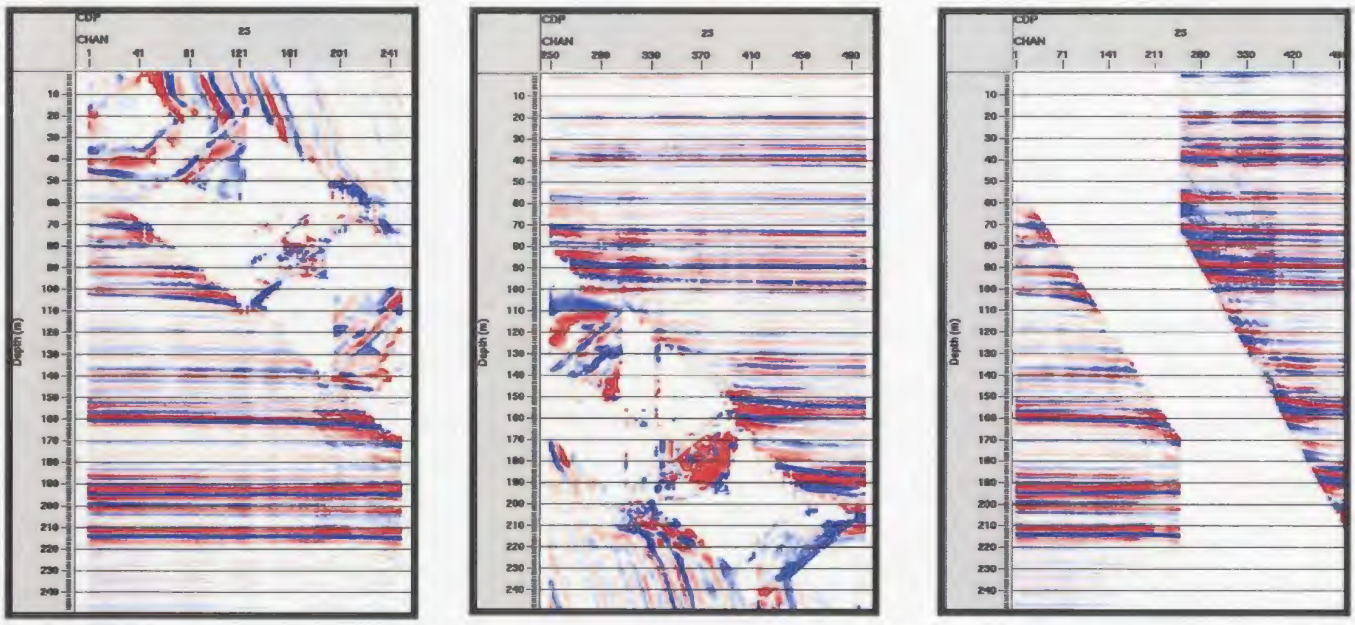

Figure 3.26: Migrated upgoing (left) and downgoing (middle) gathers and the merged result (right) from model 2. Before the datasets were merged the two datasets were muted to remove noise.

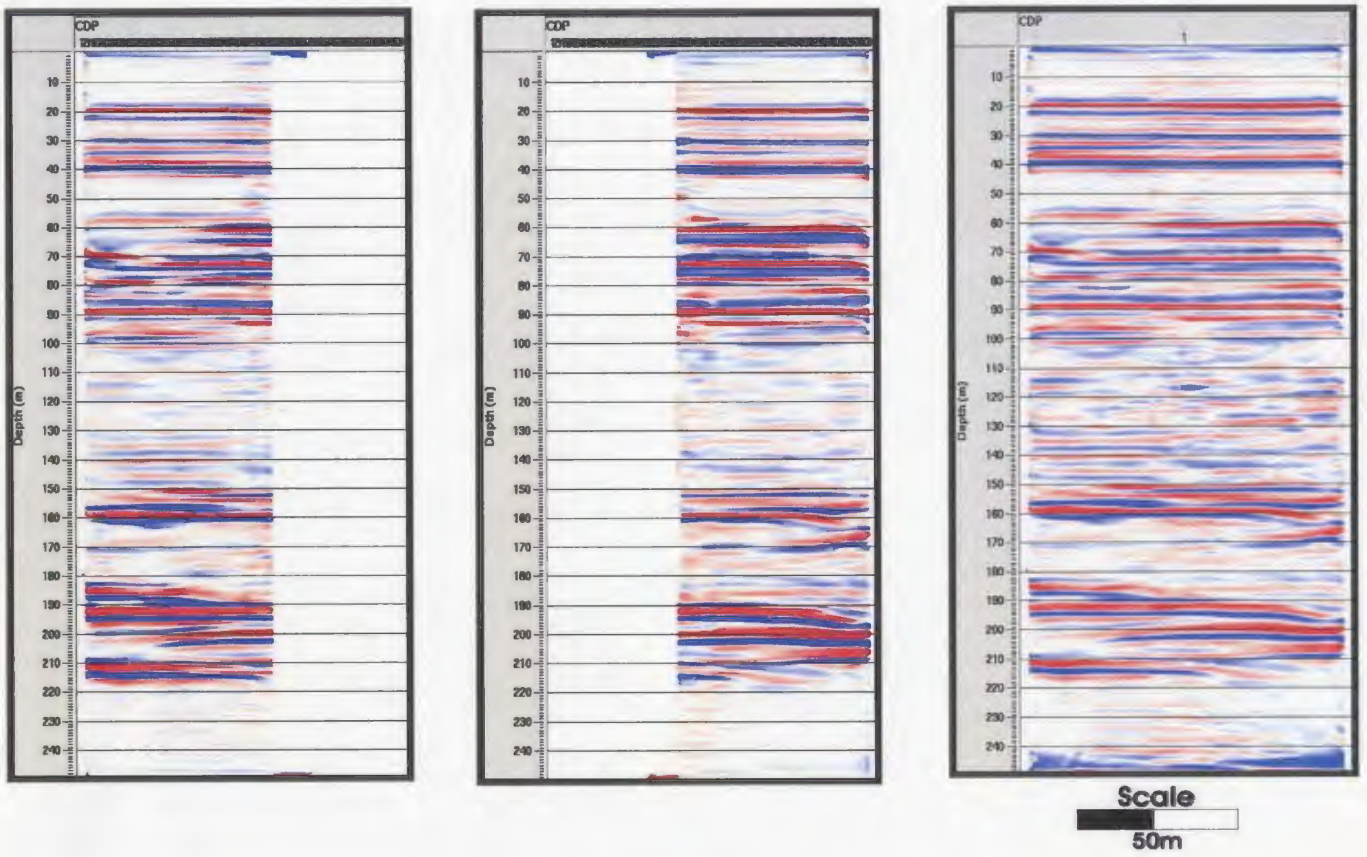

Figure 3.27: Stacked common receiver gathers (left), and stacked common shot gathers (middle), and merged result from the two stacks (right) from model 2.

3.5 Computing Incident Angles

The CDP gathers can produce an image of the subsurface, but the gathers themselves have little meaning. Currently, the secondary sort of the CDP gathers is shot or receiver location, which is meaningless in the CDP domain. A more useful and meaningful way of examining the data is to calculate incident angles and transforming each gather to an Amplitude vs. Angle (AVA) gather, where the primary sort is CDP and the secondary sort is incident angle (Lazaratos et al., 1995). The transformation of data involves operating on each gather individually, where every sample, in every trace, is used to calculate an incident angle based on shot and receiver location, and reflection point location. Once an incident angle has been calculated for all samples in a gather, the samples are rearranged and new traces are created where the samples in each trace have the same incident angle. By using AVA gathers the wide angle reflections are easily identified, where most of the unwanted energy resides (Byun, 1999), and can be edited to improve stack quality.

The incident angles are calculated on a sample by sample basis using the formula,

$$\theta = \tan^{-1}(X / Y_2 - Y_1)$$

where, X is the horizontal distance the reflection point is away from the source or receiver hole, Y_2 is the depth of the shot or receiver, and Y_1 is the depth of reflection point (figure 3.28). The approach applied here assumes straight ray paths and horizontal reflectors, but an algorithm that raytraces may deliver more reliable results. However, due to the short travel paths and the fact there isn't a gradual increase in velocity, but a

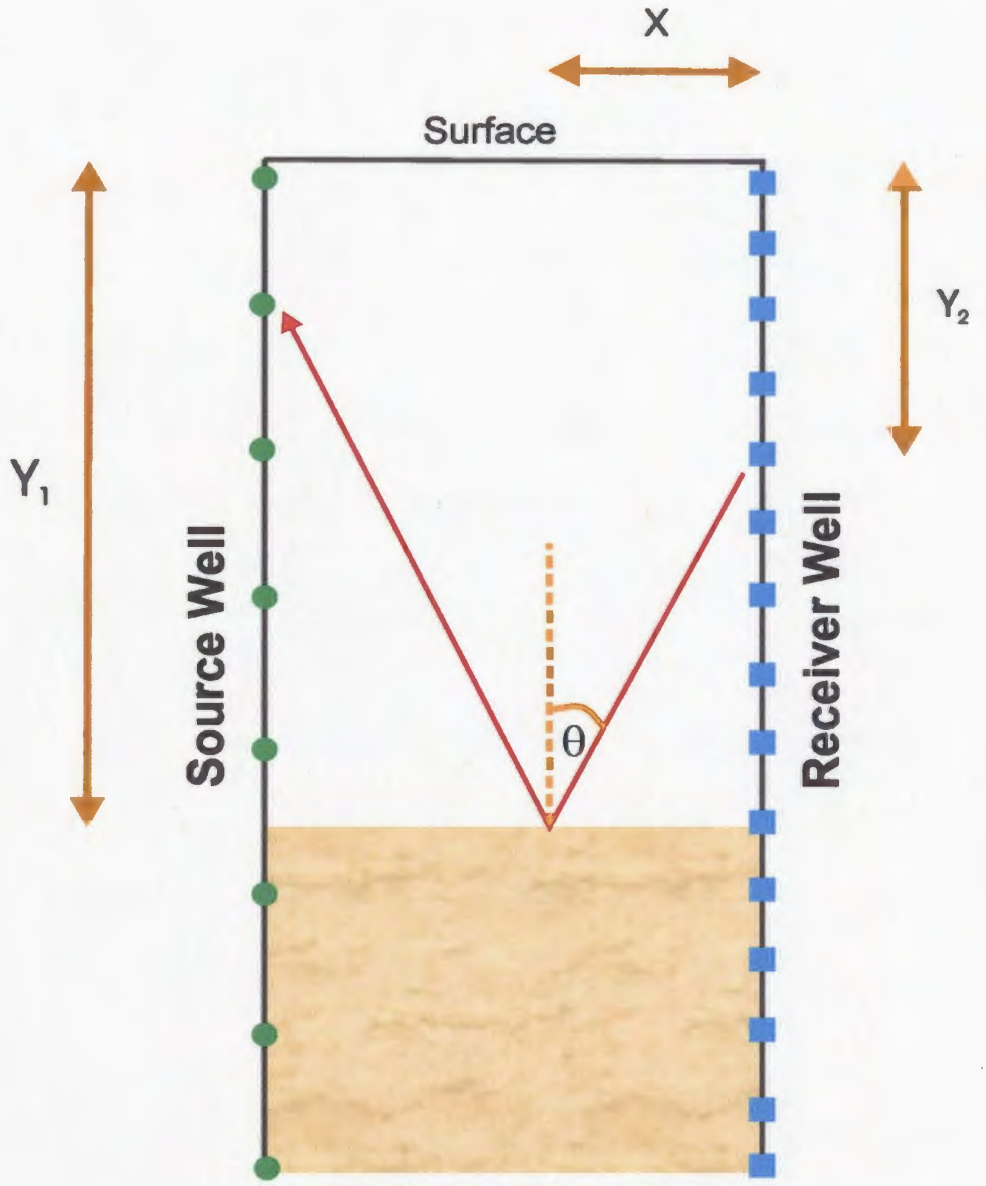

Figure 3.28: Geometry of incident angle calculations for common receiver gathers. θ is the incident angle, Y1 is the depth of reflection, X is the distance from the receiver well (distance from source well for common shot gathers), and Y2 is the depth of receiver (or shot for common shot gathers).

more variable distribution of velocity increases and decreases of very thin beds, the assumption of straight rays should deliver reliable results.

The functionality to transform the data to incident angles does not exist in *ProMAX*® so the data is exported into user-defined programs to perform the calculations. The data is exported from *ProMAX*® in SEG-Y format, and is converted into ASCII format to calculate the incident angles and rearranged into AVA gathers. The data is then converted back into SEG-Y format for input back into *ProMAX*®.

3.5.1 Model 1

Figure 3.29 shows an AVA gather from a CDP gather calculated from upgoing waves. As predicted by Byun (1999), with increasing angle of incidence the wavelet becomes broader and a phase shift occurs. By using these gathers, a mute function to remove unwanted energy is applied and angles greater than 45^{o} are eliminated to avoid wide-angle effects that would degrade the stack. Once the datasets are edited, a stack is produced in the same manner as to produce a stack after converting to CDP gathers in section 2.4. The upgoing and downgoing datasets for the common shot and receiver gathers are merged together and stacked, and these two stacks are then merged to produce an image of the subsurface figure 3.30.

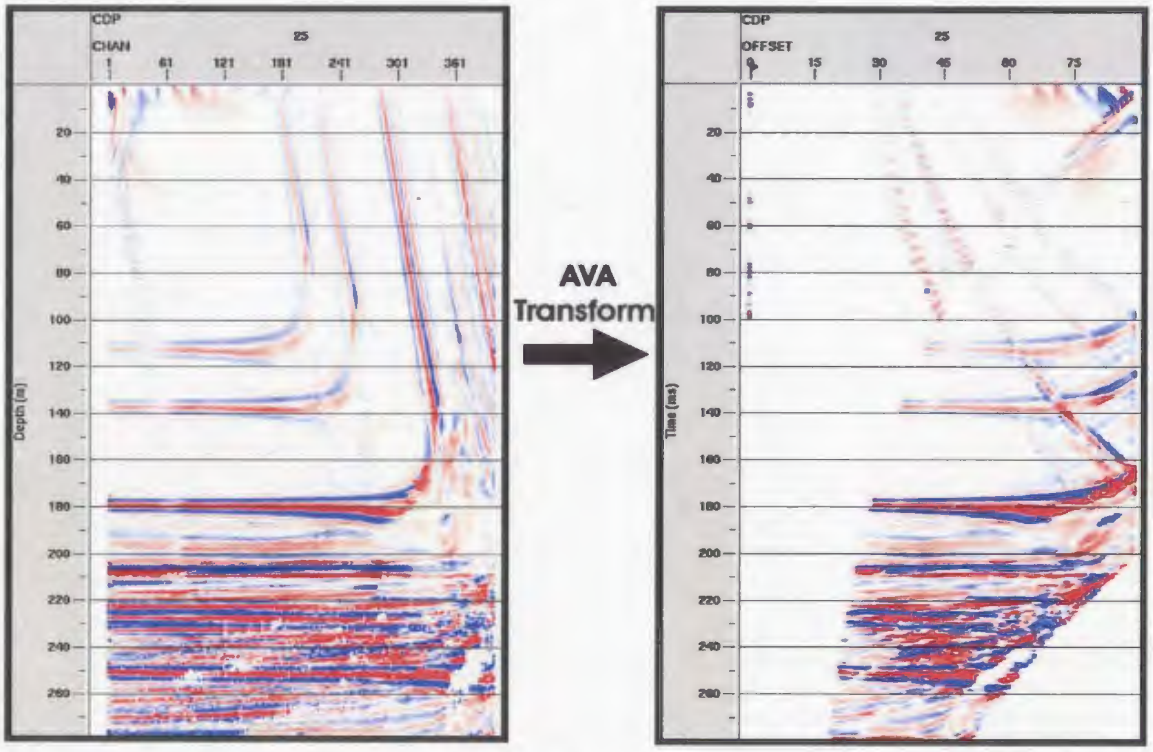

Figure 3.29: Example of transformation from CDP – receiver location domain to the CDP – incident angle domain of model 1.

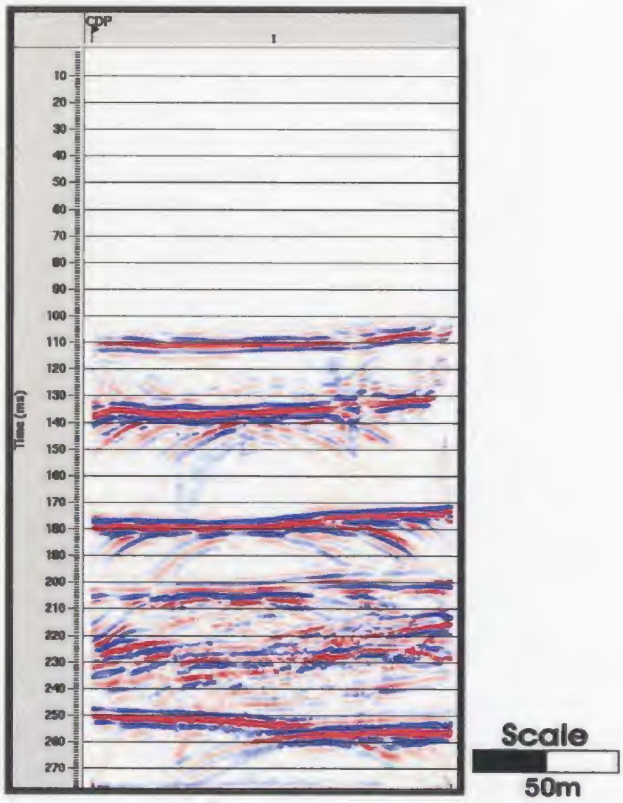

Figure 3.30: Resulting stack from the AVA gathers for model 1.

3.5.2 Models 2 and 3

An example of the transformation to AVA gathers is displayed in (Figure 3.31). The gathers are muted to remove unwanted energy and angles greater than 45^{o} are eliminated. The upgoing and downgoing, common receiver gathers and common shot gathers are merged together, the datasets are stacked, and the two stacks are merged to produce the final stack (Figure 3.32).

3.6 Post-Stack Processing

The stacks in figures 3.20 and 3.32 both contain diffractions since the limited aperture parameterization of the VSP Kirchhoff Migration prevented them from being collapsed. Diffractions interfere with reflections that can cause erroneous interpretations of the reservoir, and degrade geostatistical information extracted from heterogeneous zones, performed in the next chapter. To remove the diffractions a mild trace mix is used. Ideally, a post-stack migration is warranted, but with a small inter-well distance (Model 1 125m and Models 2 and 3 100m) a large aperture cannot be used because of excessive smearing, and the 2-D migrations in *ProMAX*® assume shot and receivers are at the surface, but the shots and receivers are located downhole for cross-well seismic surveys. Post-stack cross-well migrations do exist however (Byun et al., 2002), but are unavailable for this study.

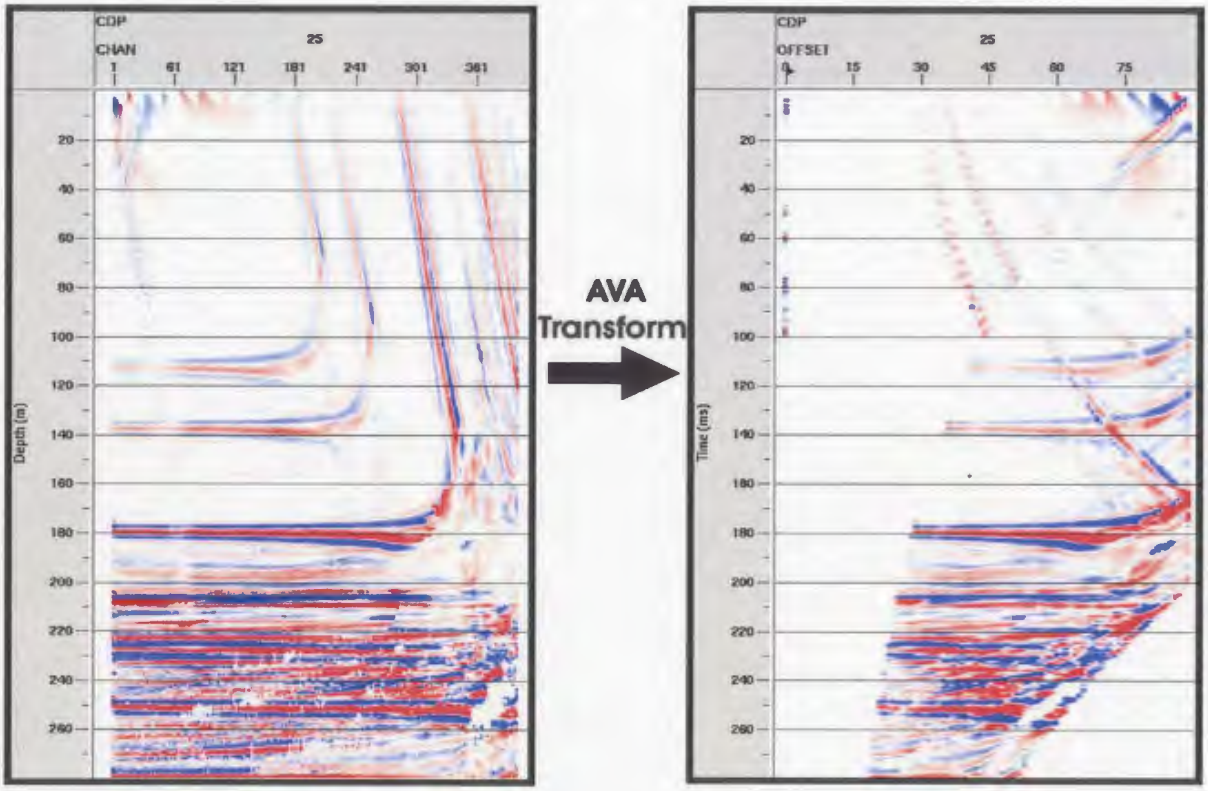

Figure 3.31: Example of transformation from CDP – receiver location domain to the CDP – incident angle domain from model 2.

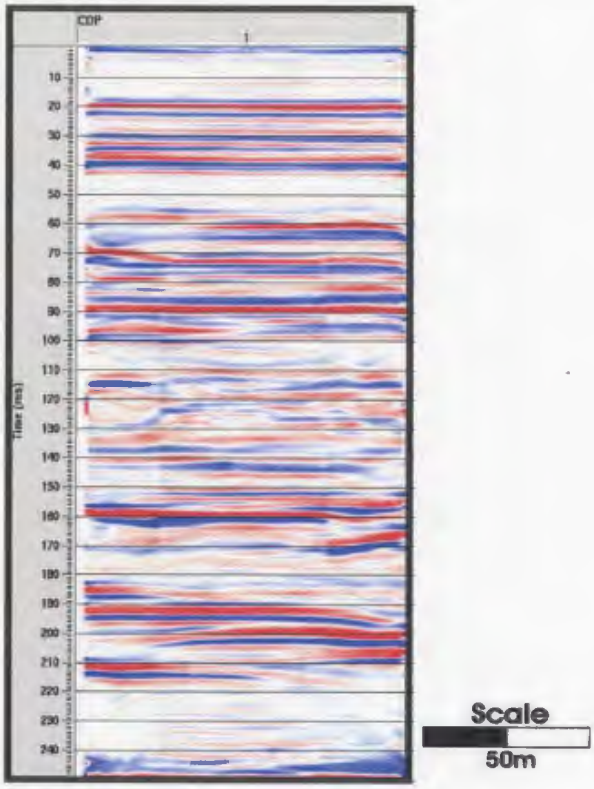

Figure 3.32: Resulting stack from the AVA gathers for model 2.

3.6.1 Model 1

Figure 3.33 displays the mixed result along with the input stack. A 3-trace mix successfully removes diffractions, but the stack is now smeared. The general dip of the heterogeneous zone is still visible, but some of the smaller reflections from the steeply dipping layers have been lost. However, diffractions do not contaminate the heterogeneous zone now, especially at CDP 5 - 10 and between depths 205 – 225m. The trace mixed version is used to extract the geostatistics because the statistics will reflect variations in the reflections, and not of diffractions

3.6.2 Model 2 and 3

A 3-trace mix is also used for models 2 and 3 and the result is displayed in figure 3.34. The trace mix produces a cleaner stack without excessive smearing, and terminations of the concretionary intervals are consistent with the input stack. The comparison between this result to the result from model 1 suggest that cleaning a stack with a trace mix works best when used with flat, horizontal layers.

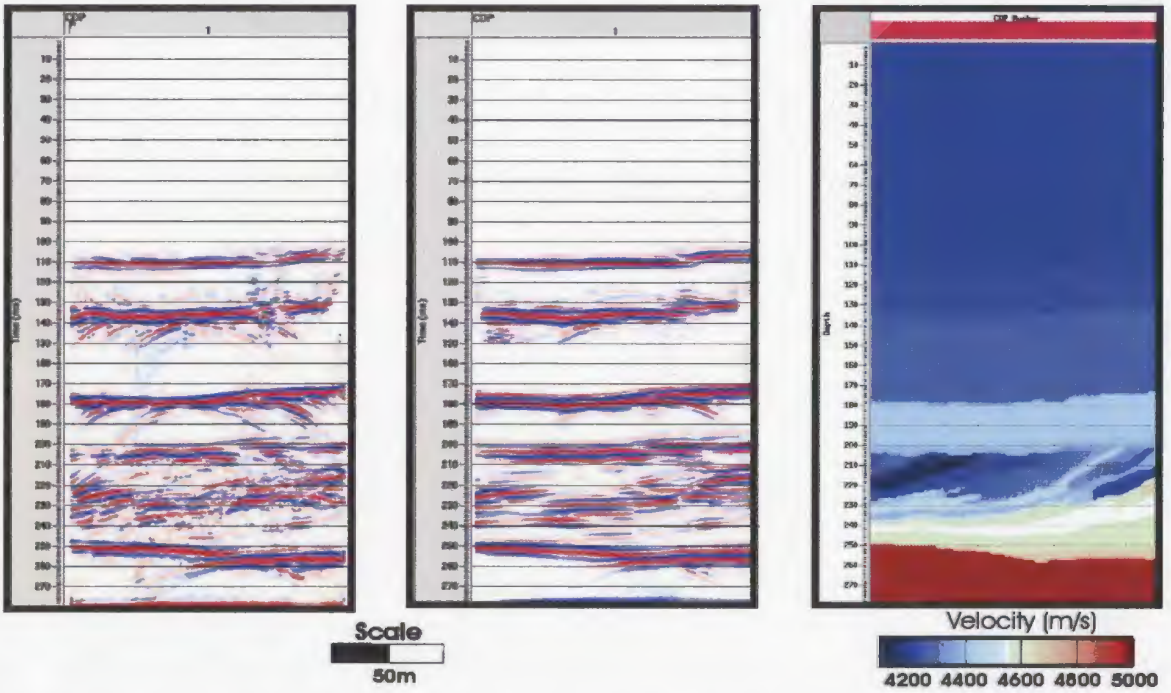

Figure 3.33: The stack produced from AVA gathers (left), and the AVA stack with a 3-trace mix applied (middle) of model 1. At the right is the velocity model used to create the cross-well seismic data.

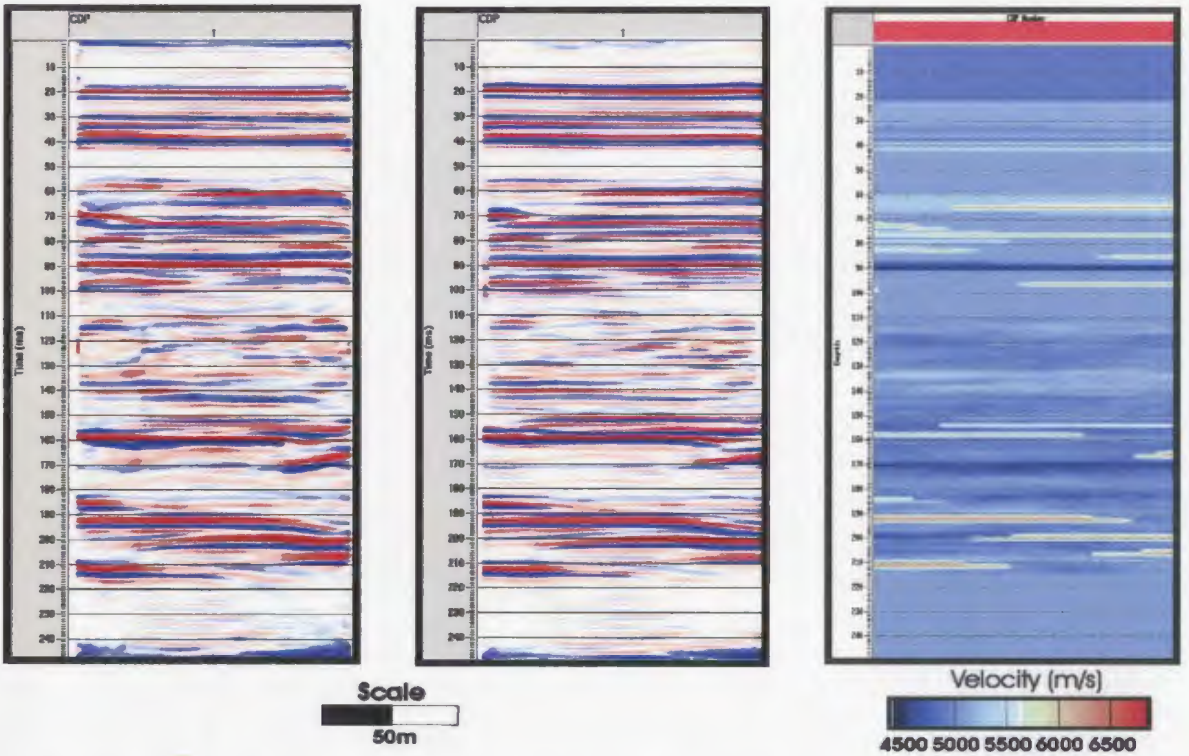

Figure 3.34: The stack produced from AVA gathers (left), and the AVA stack with a 3-trace mix applied (middle) of model 2. At the right is the velocity model used to create the cross-well seismic data.

3.7 Discussion

The processing flow described in this chapter is a simplified version of a flow used on real cross-well seismic data. The processing flow consists of creating the synthetic data, wavefield separation, transforming the data from the cross-well domain to the CDP domain, transformation to amplitude vs. angle (AVA) gathers, and post-stack processing. Two major processing issues are avoided due to the use of synthetic datasets. First, tomography was not needed to generate velocity models, since velocity models are used to create the data. Second, separating different modes of energy (P- and S-waves) is not necessary since this was an acoustic modeling study. Without these factors, a simplified processing flow is used, and cleaner images of the models are produced.

Knowing the velocity model is advantageous for producing an image of the subsurface using cross-well seismic data. Velocities are used mainly for transforming the data from the cross-well domain to the CDP domain. A tomographic result will only deliver a rough estimate of the velocity model between the two wells, which may produce inaccurate traveltime maps and introduce error in the cross-well to CDP transformation in both methods of transformation. Velocity picking can be done after transformation to improve the tomographic result (Lazaratos et al., 1995), but that may include doing multiple transformations leading to increased computation time. Knowing the velocity model is an advantage for this study, but for a real data study the velocity model will not be known, except at the well locations.

Without converted waves the wavefield is less complex, enabling a simplified processing flow. The processing time is reduced since the different modes of energy do

not require identification and separation, and with simplified gathers (and no noise) a more coherent P-wave stack can be produced. When using real cross-well data, the S-wave data are beneficial because it can provide additional information about the reservoir, and are easier to extract from the total wavefield because they do not contend with transmitted interference like the P-waves do (Rector et al., 1995). However, the P-wave arrivals have higher frequency content. For example, from Lazaratos et al. (1995) the P-wave reflections contained frequencies above 1600Hz and the S-wave reflections contained frequencies above 1100Hz. For the objectives of this study the P-wave data were suitable, but when using real data, both P- and S-wave data would be used for analysis.

Chapter 4

Statistical Analysis

4.1 Introduction

The seismic data produced in the previous chapter provides high resolution images of the velocity models created in chapter 2. The cross-well processing routine is able to image small-scale vertical and horizontal details incorporated into the models. Coherent features resulting from specular reflections are used to visually interpret the data, while incoherent features shorter than the Fresnel zone are represented by a complex scattered image. The scattered image cannot be easily interpreted visually, so an alternative method is needed for deriving information from the wavefield. The extraction of spatial statistics from the seismic section can provide information about the scale and distribution of sub-Fresnel zone heterogeneity and improve the understanding of reservoir features.

4.2 Statistical Method

To explore the statistical properties of heterogeneity represented by the seismic signature of the reservoir models, a method of estimating the scaling properties of the reflection wavefield is adapted from studies of crustal environments (Hollinger and Levander, 1992; Hurich 2003; Hurich and Kocurko, 2000). The method is based on the idea that the scattered seismic wavefield carries a band limited version of the acoustic impedance field that represents the reservoir. The analysis involves determining the

statistical characteristics of heterogeneity sampled by seismic waves by comparing the autocorrelation or power spectrum of the wavefield with that of the von Karman distribution. The von Karman distribution is designed to describe self similar (power law) media (Frankel and Clayton, 1986) using the parameters variance, correlation length, and Hurst number (Hurich and Kocurko, 2000). The spatial statistics of the seismic data are determined using the autocorrelation of a windowed data sample, which is then fit to a theoretical von Karman model using a least squares approach. The fitting process results in estimates of variance, correlation length, and Hurst number. Variance describes the variability of amplitudes within the data. The correlation length represents the lateral scale length beyond which heterogeneity is uncorrelated (Figure 4.1). For scale lengths smaller then the correlation length the distribution of scales is represented by a power law and is self-similar. The Hurst number is the exponent of the power law and describes the completeness of the range of scale lengths within the data, with the correlation length being the largest (Figure 4.1). As the Hurst number tends to zero, the completeness of the range of scale lengths increases, which indicates a 'rougher' seismic response because a larger range of scale lengths is contained within a seismic event(s) (Hurich, 2003). These parameters provide information concerning the scales and the scaling properties of features within the reflection wavefield of the reservoir models.

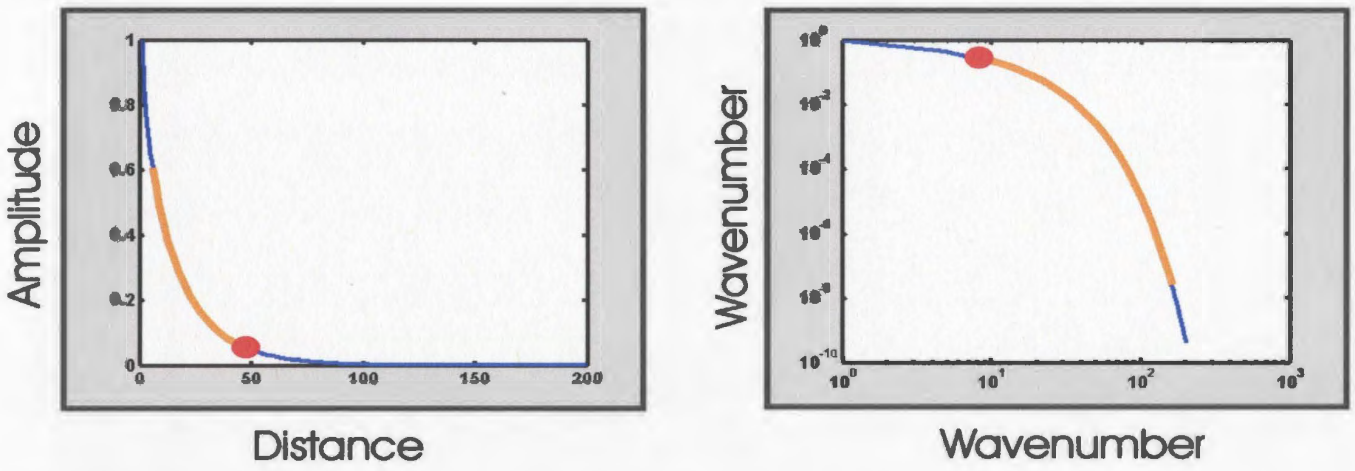

Figure 4.1: Graphs displaying the autocorrelation function of a sliding window of data, shown in amplitude – distance space (left) and in wavenumber – wavenumber space (right). The red dot indicates the correlation length where the distribution is no longer represented by a Power Law distribution, and the orange line curve before the red dot outlines the slope of the power law distribution that represents the Hurst number.

The range of scales of the detected reservoir heterogeneities is dependant on the frequencies used to acquire the seismic data. This study uses much higher frequencies (>1000Hz) than conventional surface seismic data, therefore the scale of features for which spatial statistics are derived are much smaller (a metre apart vertically and as small as a few metres horizontally) (Appendix A) than seen in previous studies (Hollinger and Levander, 1992; Hurich and Kocurko, 2000). However, this study deals with synthetic data absent of noise, tube waves, and converted waves, all which would potentially decrease resolution and lower the ability to extract statistical information about the spatial distribution of reservoir features. Therefore, the quality of the statistics would be dependant on the ability of the cross-well seismic processing to remove unwanted events in the wavefield and successfully separate the P- and S-wave components. The wavefields in this study only contain compressional waves and no noise, so the

effectiveness of extracting spatial statistics should be primarily a factor of the technique, and not of the data or processing quality.

The spatial statistics are extracted from the seismic data using two methods. The first method extracts measurements using a window that extends the full inter-well distance and can vary vertically, which provides an average estimate of the correlation length and Hurst number. The second method maps the variation in heterogeneity within the reservoir by extracting parameter estimates for a sliding window passing through the seismic section. For each window the correlation length, Hurst number, and power are estimated, and the resolution of the mapping is a function of window size. Resolution is increased by decreasing the window size, but if the window is too small insufficient data samples are included in the autocorrelation resulting in unreliable estimates. However, if the window is made too big the results may become smeared producing a loss of resolution. Therefore, the choice of window sizes for this study was based on the stability of the statistical results at the appropriate resolution. By comparing these two methods an evaluation of the reliability of the measurements can be made.

Section 4.3 Analysis

Section 4.3.1 Model 1

Model 1 contains four thick layers overlying a heterogeneous zone containing a suite of clinoforms representing the reservoir interval, followed by another thick layer (Figure 4.2). The reservoir interval extends from 205m to 245m and gently dips to the left. Clinoforms displayed in the velocity model range in thickness from less than 1m to

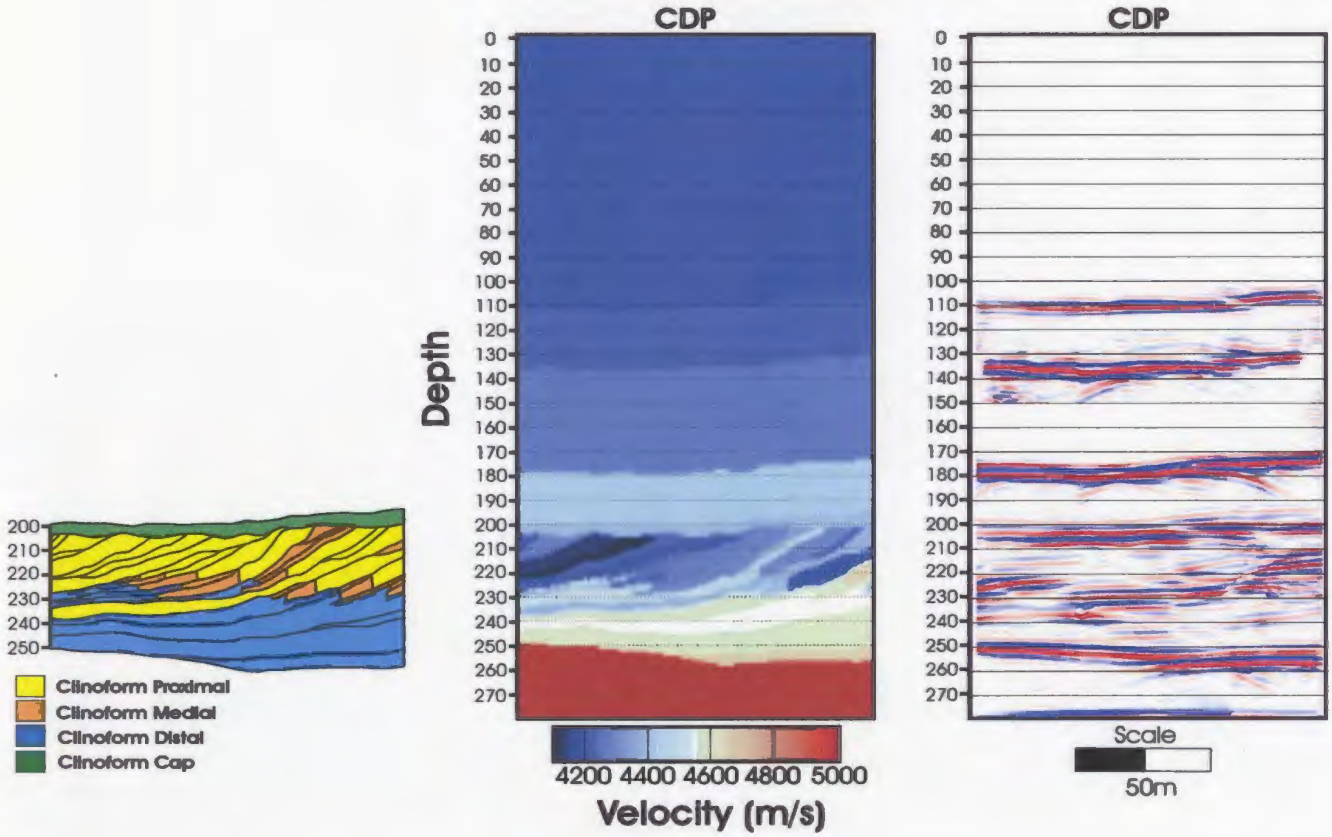

Figure 4.2: Clinoform lithologies, velocity model, and the corresponding cross-well seismic stacked data for model 1.

10m, and extend 5 – 125m in length. A comparison of the seismic data with the velocity model shows that not every clinoform is resolved because some are too small to be imaged and/or the velocity contrast is too small to produce a noticeable reflection. Even though not all the clinoforms can be imaged, the dominant trend of the layers is captured and the division between the three main clinoform packages (clinoform cap, proximal, and distal) can be identified. Statistical analysis is used to derive more information about the reservoir interval to aid interpretation.

Maps of power, correlation length, and Hurst number displayed in figure 4.3 are used to help understand the distribution of reflections. The maps are computed using a window 50m in length and 10m vertically moved through the section every 2m horizontally and every 1m vertically, while accounting for the dip of reflections. Each pixel in the maps represents a sample of seismic data the size of the analysis window. Measurements of the correlation length and Hurst number are also made on the whole reservoir interval. These measurements provide additional information for interpretation of the scattered wavefield.

The power map (Figure 4.3a) is a measure of the combination of amplitude, number of cycles, and coherency of the wavefield within the mapping window. The boundaries of the thick layers and the top and bottom of the reservoir interval display the highest amplitudes. There is also a higher amplitude area that runs through the middle of the reservoir interval at a depth of 220 – 230m and power value of ~4000, marking a strong impedance boundary within the clinoform package.

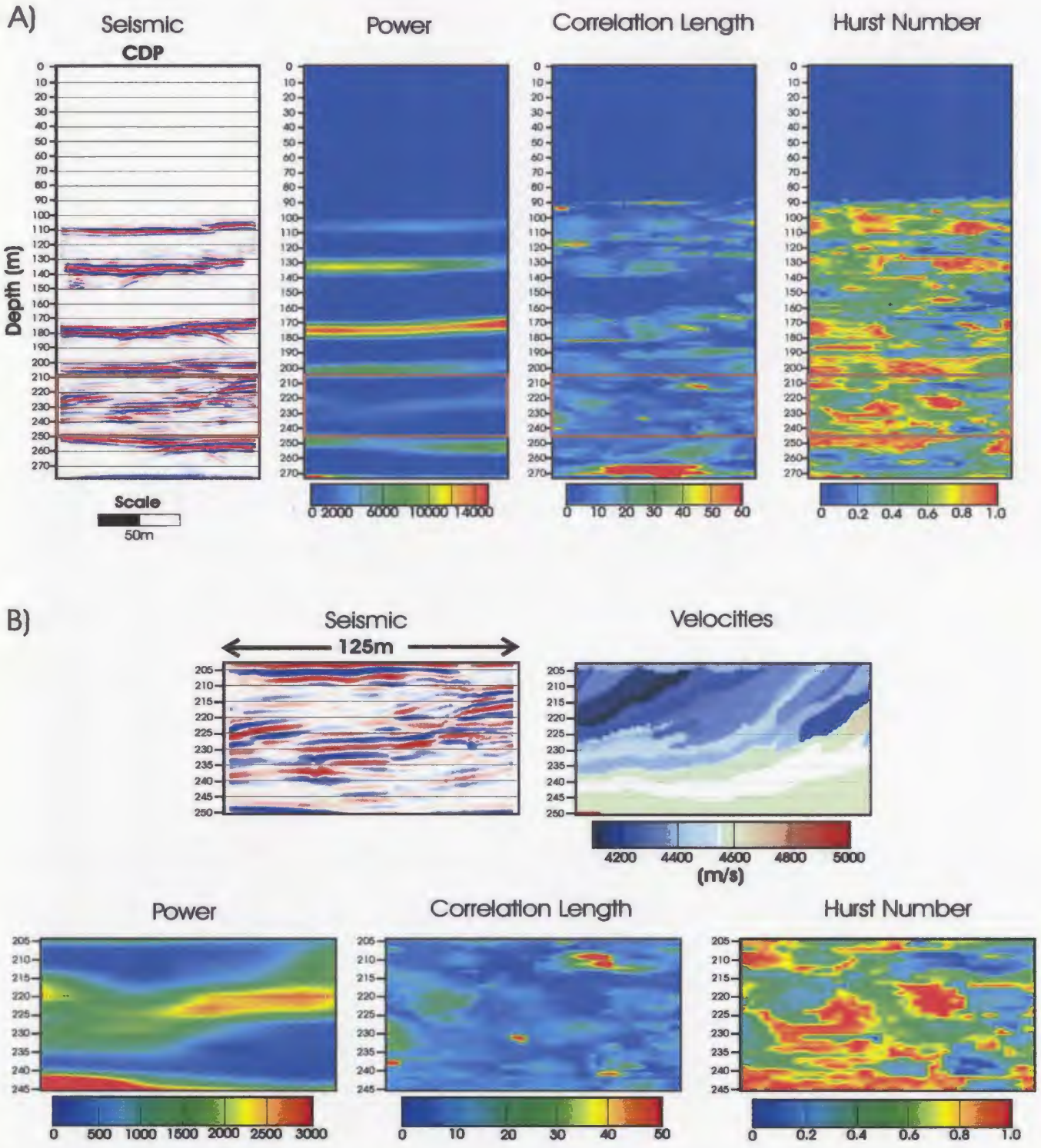

Figure 4.3: A) Seismic section along with statistical maps of the power, correlation length, and Hurst number from model 1. The brown box shows the zoomed area for B. B) Statistical maps of the reservoir portion from A, between depths 205m and 245m.

The correlation length map is more complicated then the power map (Figure 4.3a). The highest correlation lengths occur at the boundaries of the four thick layers and the bottom of the suite of clinoforms. The correlation lengths are not continuous across the whole section indicating variations in the range of scales across these impedance contrasts, possibly due to the uneven interfaces between these layers. There are also high correlation lengths within the suite of clinoforms that are examined in the following paragraph. The Hurst number values are even more complex, displaying much variation in the scaling properties of reflections. The comparison of the correlation length map and Hurst number map show they are anti-correlated, where areas corresponding to large correlation lengths are associated with small Hurst numbers, and vice versa. This indicates that in areas where large correlation lengths exist, the window contains complete range of spatial scales, but in areas where the correlation length is shorter all the events are around the same length.

Zooming in between 203 – 250m (Figure 4.3b), displays variations in the three maps better at the reservoir interval, as they are not scaled by outside measurements. The power map demonstrates the largest amplitudes are located in the middle of the reservoir section signifying a large, dipping, impedance contrast where the transition from clinoform proximal to clinoform distal occurs. By comparing the correlation length and Hurst number maps to the power map shows no correlation because the calculation of these maps is independent of amplitude. The correlation length map displays small areas where a large range of scales is present exhibiting power law scaling, but for the most part correlation lengths are limited to smaller scales, with a mean length of ~9.5m, as

shown in the histogram (Figure 4.4). The Hurst number map is anti-correlated with the correlation length map (as mentioned above), and is dominated by mid to high values with low value areas corresponding to high correlation lengths. The histogram from the section shows a fairly even distribution of values between 0.25 and 1.0 (Figure 4.4). The statistics indicate the reservoir interval is dominated by small-scale features, but the completeness of scale lengths is variable. The dominance of small-scale features found in the seismic section could be a factor of the shorter and thinner clinforms, but also of the cross-well seismic data's ability of resolving the variations in thickness of the longer clinforms as well.

The mapped correlation lengths and Hurst numbers are plotted on a histogram, where the mean, median, and standard deviation are displayed in blue (Figure 4.4). The standard deviation for the correlation lengths is 6.3, which covers the bulk of the correlation lengths found in the reservoir section. The standard deviation for the Hurst numbers appears to be low for the range and frequency of Hurst numbers, but is largely influenced by the two peaks on either side of the mean. Measurements from the entire reservoir interval are also shown on the histogram in green, and are slightly higher for the correlation lengths, but are in close agreement with the Hurst number values. The close agreement of the mean and median of the mapped values with the whole reservoir measurements provides evidence that the mapped values display accurate spatial variations of the seismic wavefield.

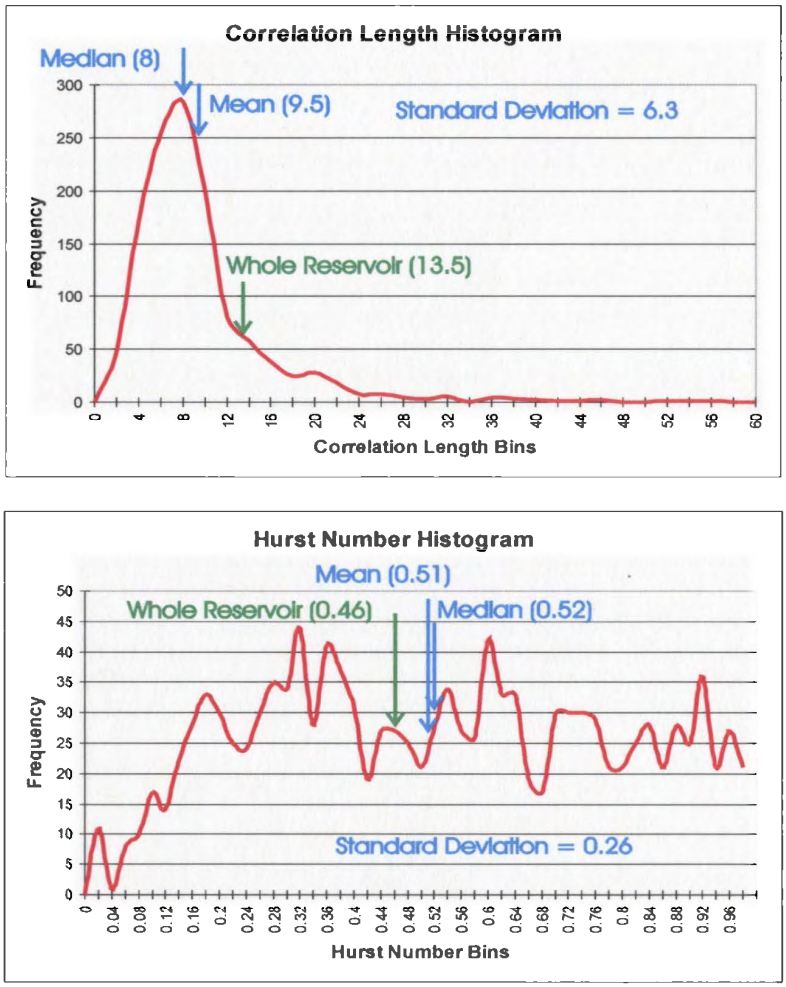

Figure 4.4: Histograms computed from the values of the statistical maps of correlation length and Hurst number of model 1. Shown on the histograms are the mean, median, and standard deviation from the mapped measurements in blue, and in green are the measurements of the whole reservoir section.

Section 4.3.2 Models 2 and 3

Models 2 and 3 contain a sandstone package surrounded by shale layers on the top and bottom, with some intermixed thin siltstone layers and concretionary intervals that vary in length and thickness (Figure 4.5). The reservoir interval within the sandstone package is located between depths 110m and 215m. Outside the reservoir interval, layers are represented by constant velocities that are the same for both models, but within the reservoir interval a stochastic velocity field iss added to simulate reservoir heterogeneity. Each model is given a different stochastic field representing end-member porosity distributions. Model 2 represents porosity controlled by bedding and shows a strong shape anisotropy (Figure 4.5a), and model 3 represents porosity controlled by a more distributed process such as diagenetic effects (Figure 4.5b).

Maps of the power, correlation length, and Hurst number are computed on the whole section using a window 35m in length and 17.5m vertically moved through the section every 2m horizontally and every 1m vertically. Each pixel in the maps represents a sample of seismic data the size of the analysis window. Whole reservoir measurements of the reservoir interval are also made between depths 110 – 152m, using the full inter-well distance (100m). This area is chosen because it represents an area of the stochastic field that is uninterrupted by concretionary intervals that tend to heavily influence the statistical results, creating unreliable measurements of the stochastic field.

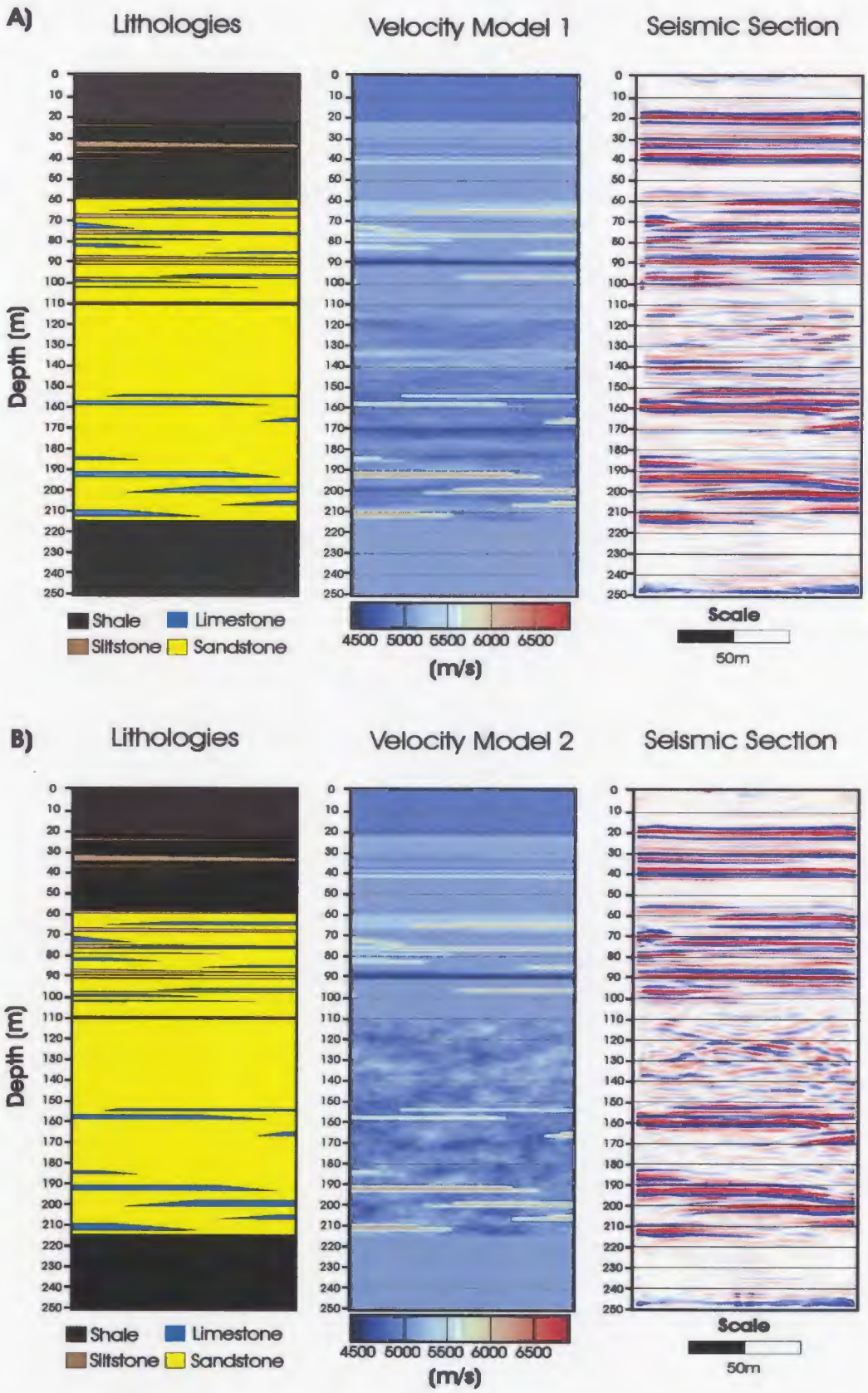

Figure 4.5: Lithologies, velocities, and seismic section from model 2 (A) and model 3 (B).

The statistical maps produced from the seismic sections of both these models outside the reservoir interval are similar (Figure 4.6a and 4.7a). The areas where the concretionary intervals are situated, are represented by higher power and longer correlation lengths, and vice versa for areas that were absent from the concretionary intervals. The Hurst number maps are anti-correlated with the correlation length map, as seen in model 1. However, the Hurst numbers are mildly variable around the mid-range mark indicating the range of scale lengths within the wavefield is approximately the same for their respective correlation lengths. There are some areas within the region of the stochastic velocity field that have higher Hurst numbers, corresponding to areas of short correlation lengths. There are also higher Hurst numbers at the bottom of the section within the shale layer where there are no layers and is represented by noise. In general, above the stochastic field correlation lengths are mainly influenced by the concretionary intervals with little variation in the Hurst number. More variations are observed inside the reservoir interval where the stochastic fields were added.

A comparison of the power maps between the two models show the amplitudes in the model 2 are stronger then in model 3 (Figure 4.6b and 4.7b). This signifies that stronger reflections are produced from long and thin layers, rather then short and thick layers, where a weaker scattered wavefield is produced. This is consistent with observations from Hurich and Kocurko (2000), where the high power reflections originate from zones characterized by relatively thin, continuous (high aspect ratio) impedance contrasts. Localized zones of high power for the two models can be attributed

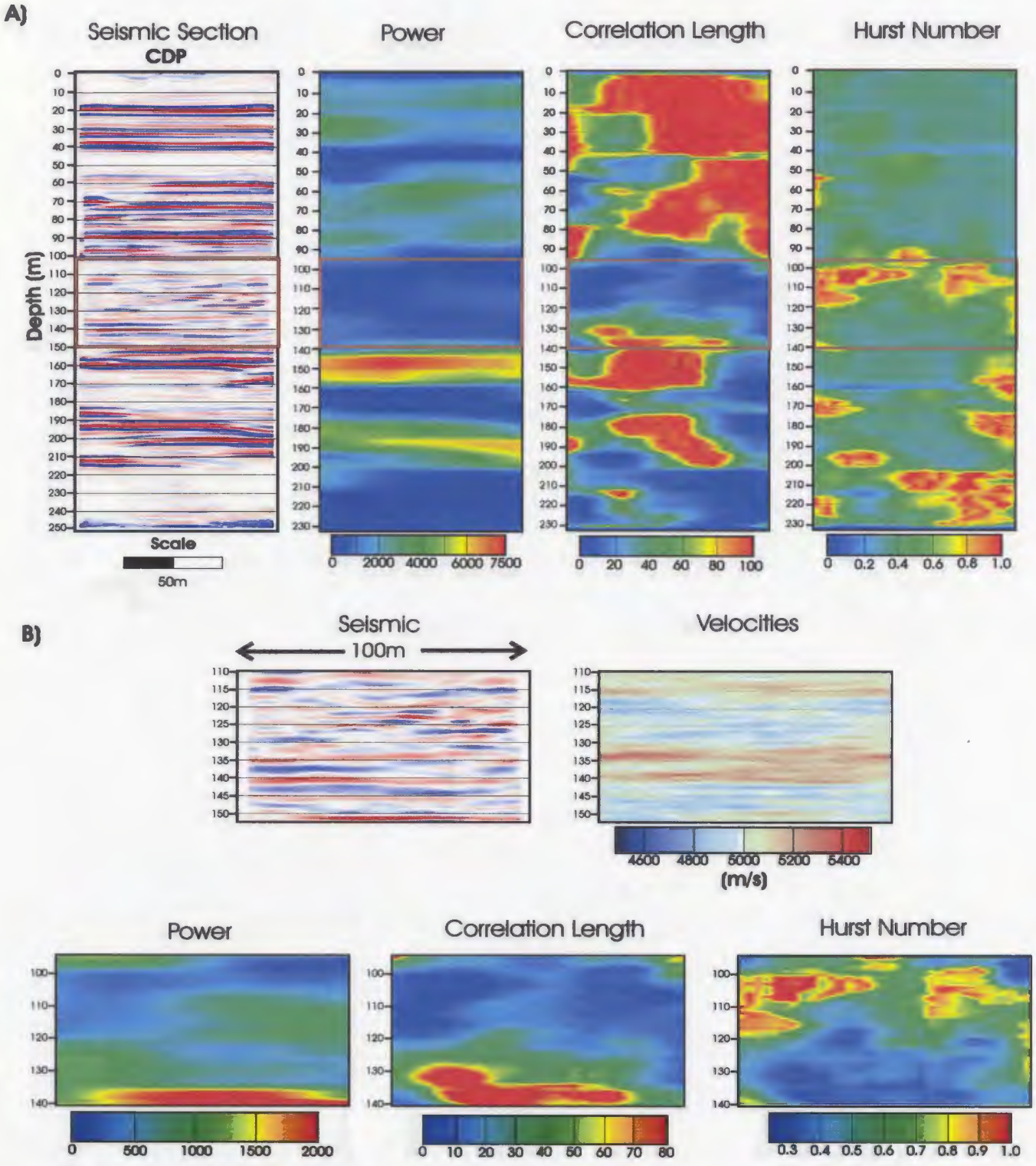

Figure 4.6: A) Seismic section along with statistical maps of the power, correlation length, and Hurst number from model 2. The brown box shows the zoomed area for B. B)) Seismic section, velocity field, and statistical maps of the reservoir portion from A, between depths 95m and 140m.

to the geometry of the wavefield, where short, unordered impedance contrasts can produce high amplitudes from spatial and temporal interference (Hurich, 2003). The power map delivers a generalized interpretation of the impedance field geometry, since the wavefield geometry is controlled by the impedance field geometry, but further interpretations are needed from the correlation length and Hurst number maps.

Model 2 displays considerable variation in the reservoir interval, where there is a clear division between the top and bottom (Figure 4.6b). The top part of the section has lower correlation lengths and higher Hurst numbers than the bottom, corresponding to short events that are around the same length. These maps demonstrate that only a small range of scale lengths exhibit power law scaling within the top part of the section. In the bottom half of the section there is a more complete range of spatial scale lengths exhibiting power law scaling. These observations are consistent with the anti-correlation of the two maps. The comparison of the top and bottom of the Hurst number map show the variability of Hurst numbers is higher when associated with low correlation lengths, then with high correlation lengths. Therefore, the variability in the range of scale lengths is greater for short correlation lengths. Even though the stochastic velocity field is synthetic, these two different responses could indicate two different types of sandstone packages, or one sandstone package with differing physical properties.

Model 2

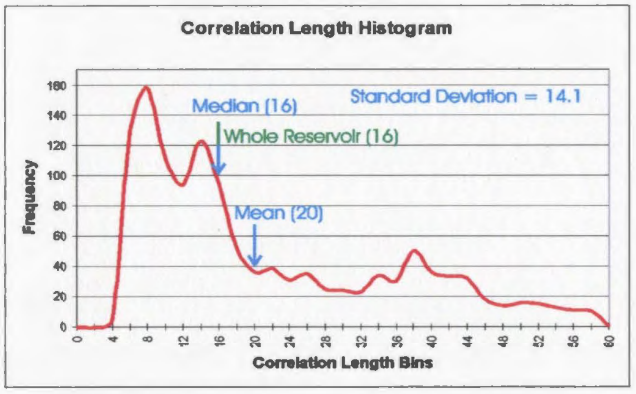

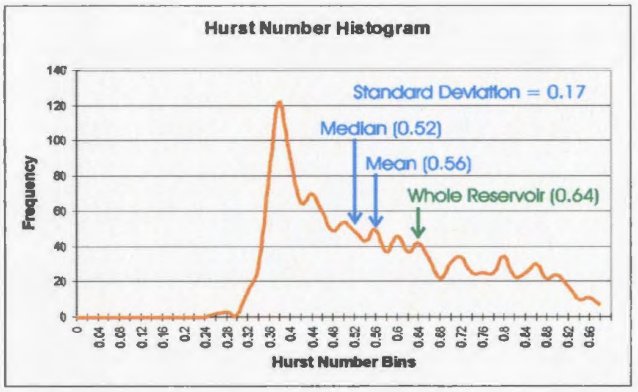

Model 3

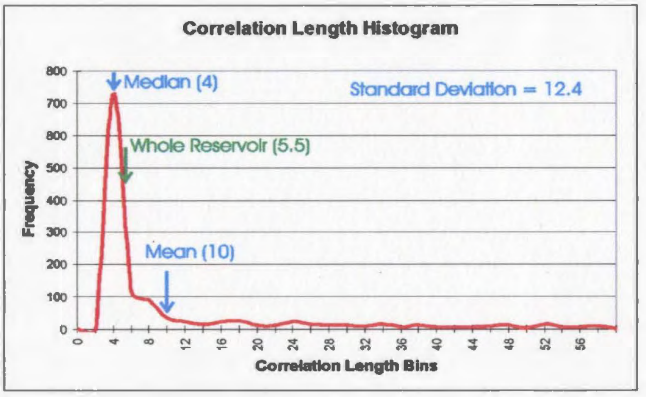

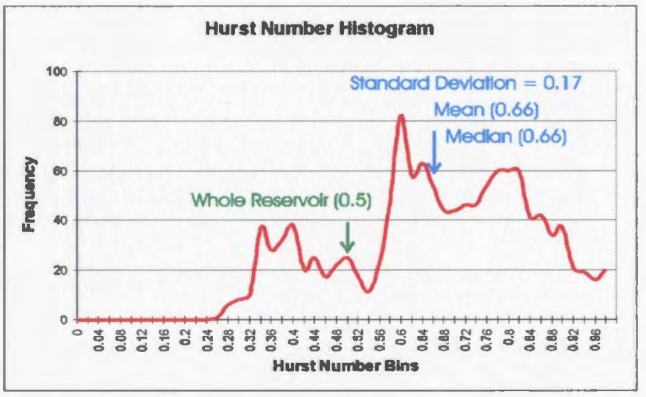

Figure 4.8: Histograms computed from the values of the statistical maps of correlation length and Hurst number of model 2 and model 3. Shown on the histograms are the mean, median, and standard deviation from the mapped measurements in blue, and in green are the measurements of the whole reservoir section.

The histograms for the correlation length and Hurst number maps are shown in figure 4.8 for model 2, with the mean, median, and standard deviation in blue and the whole reservoir measurements in green. The correlation length histogram shows the bulk of the measurements situated between 5 and 18, with a mean of 20, median of 16, and standard deviation of 14.1. The mean does not fall within the bulk of the measurements due to the widely spread distribution of correlation lengths within the data. The measurement for the correlation length of the whole section is the same as the median value, 16. The Hurst numbers range predominately from 0.39 – 0.68, with a small standard deviation of 0.17. The Hurst number histogram shows that the whole reservoir measurement (0.64) is slightly higher then the mean and median of the mapped values. Even though there are discrepancies between mean and median mapped values with the whole reservoir measurements they are still in close agreement. This agreement provides evidence that the mapped values deliver accurate measurements of the spatial variations in the wavefield. However, there are some correlation lengths that are bigger then the analysis window, which have to be treated as relative variations.

Maps of the reservoir interval from model 3 are considerable different from model 2 due to the differing stochastic velocity representing the reservoir interval. Model 3 shows less variability in the correlation lengths (Figure 4.7b), but increased variability in the Hurst number map as seen in the histograms in figures 4.8, and are still anti-correlated. This observation is the same as seen in the top portion of model 2, where lower correlation lengths correspond to lower and more variable Hurst number values. This suggests that the seismic section contains short events that are approximately the

same length. These statistics might indicate a sandstone package with consistent bedding lengths with varying ranges of scale, possibly due to changes in the physical properties within the sandstone layers.

The histograms for the correlation length and Hurst number maps are shown in figure 4.8 for model 3. The histogram shows the distribution of correlation lengths is limited and concentrated around 4 with a standard deviation of 12.4. The whole reservoir measurements for the correlation length map are in agreement with the bulk of the measurements found in the section. The whole reservoir Hurst number measurement is slightly lower then the bulk of the mapped measurements, found between 0.6 and 0.84. As witnessed in the previous two models, the whole reservoir measurements agree with the mapped values, supporting the validity of mapped values and almost all measurements are below the analysis window size.

The measurements extracted from the seismic data can now be compared to the input parameters used to create the stochastic portion of the velocity fields. The measurements extracted from the seismic data for model 2 (Table 4.1) shows that the correlation lengths are much lower then the input stochastic velocity field parameters, but the Hurst numbers are in agreement. The discrepancy between the correlation lengths suggests that the resolution limit is predominately in the vertical direction, since the seismic data is unable to resolve the long thin layering of the stochastic velocity, which results in a scattered image producing the appearance of shorter events. This indicates that the stochastic velocity field parameters are below the vertical resolution of the cross-well seismic data, and the seismic data resolves a larger scale of events within the data.

	Correlation Length	Hurst Number
Input Parameters for Stochastic Velocity Field	50	0.5
Whole Reservoir Measurements	16	0.64
Mean of Mapped Measurements	20	0.56
Median of Mapped Measurements	16	0.52

Table 4.1: The correlation length and Hurst number used for the input stochastic velocity field for model 2, and the correlation lengths and Hurst numbers extracted through whole reservoir measurements and the mean and median of the mapped measurements.

Another factor affecting the correlation lengths is the window size for computing the attributes. A longer window size might improve statistics, but as mentioned before, increasing the window size decreases resolution. The fact the Hurst numbers are in somewhat of agreement with the input parameters, demonstrates that the seismic data is able to capture the range of scales in the input stochastic velocity field, even with band-limited seismic data. Model 3 (Table 4.2) shows there is a relatively good agreement between the input parameters of the stochastic velocity field, the whole reservoir measurements, and the mean and median of the mapped measurements. This indicates that the parameters for the input stochastic velocity field are within the realm of resolution of the seismic data. Observations from the two tables suggests that the Hurst number calculations can deliver information concerning the range of scales, but the correlation length measurements are limited by the scale of data which the seismic data can resolve.

	Correlation Length	Hurst Number
Input Parameters for Stochastic Velocity Field	10	0.5
Whole Reservoir Measurements	5.5	0.5
Mean of Mapped Measurements	10	0.66
Median of Mapped Measurements	4	0.66

Table 4.2: The correlation length and Hurst number used for the input stochastic velocity field for model 3, and the correlation lengths and Hurst numbers extracted through whole reservoir measurements and the mean and median of the mapped measurements.

4.4 Discussion

This chapter has shown that spatial characteristics can be derived from a scattered wavefield that cannot be visually interpreted decisively. The spatial statistics are presented as attribute maps of power, correlation length, and Hurst number that describe the spatial variations of the wavefield. Whole reservoir measurements are also derived of the whole reservoir intervals in the models that provided an average correlation length and Hurst number. The mean and median of the attribute maps in the reservoir interval agree with the whole reservoir measurements, providing evidence that the mapped values are accurate until the correlation lengths become longer than the analysis window size, at which point the measurements have to be interpreted as relative values. While these measurements aid in understanding the spatial distribution of heterogeneities, they can also provide high resolution statistical constraints for flow simulations to reduce uncertainty in simulation results.

The models created for this study incorporated different types of reservoir heterogeneity, so the effectiveness of extracting these differences through statistics could be examined. A comparison of the mapping and histogram results between the three models reveals that the three examples are clearly distinguishable. The histogram plots show the most obvious distinctions, as each distribution of correlation length and Hurst number is different, implying a very different structure of heterogeneity within the models. These results show the differences are captured between the models and that different types of reservoir heterogeneity result in distinctive statistics that are captured by the seismic data.

The mean and median are used to analyze the histograms of the correlation length and Hurst number maps to estimate the central tendencies. A more rigorous statistical approach could be used to analyze the data, but is not completed for this study because the objective is to assess whether the mean and median from mapping results agree with the results of the whole reservoir. Even though a more in-depth statistical approach is not used here, the information gained could be beneficial.

The correlation length and Hurst number measurements provide descriptions of the spatial variations within the seismic data, but as observed in Table 4.1 and 4.2, the correlation length measurements are not able to predict the input parameters to the stochastic velocity field, while the Hurst numbers did. Therefore, the seismic wavefield cannot be related back to the impedance, or in this case, the velocity field. This is an unresolved issue concerning the relationship between the impedance field, velocity field, and seismic wavefield. From the observations of this study, the Hurst numbers can be

used quantitatively to relate the seismic field back to the velocity field, but the correlation lengths can be ambiguous because of the correlation lengths are limited by the resolution of seismic data. The scale of geostatistics are still much better than what can be extracted from conventional seismic techniques and are beneficial for understanding the reservoir structure.

Chapter 5

Conclusions

5.1 Conclusions

This thesis examines the effectiveness of borehole to borehole seismology for providing high resolution reservoir images, and extraction of geostatistical information from these images to improve reservoir characterization. Three models reflecting different types of reservoir heterogeneity are used to create the synthetic cross-well seismic data. The cross-well seismic reflection data are able to detect geological features less then a metre in scale both vertically and horizontal. This level of resolution is unattainable by surface seismic techniques and is significantly better than the horizontal resolution of well logs.

The high resolution images are created from an unconventional processing flow consisting of creating the synthetic data, wavefield separation, transforming the data from the cross-well domain to the CDP domain, transformation to amplitude vs. angle (AVA) gathers, and post-stack processing. A simplified processing flow from previous studies is applied since this is a 2D acoustic modeling study, and noise and tube waves are absent. Without S-waves the processing flow is simplified, and the absence of noise and tube waves eliminates the need of some of the processing required to produce coherent seismic sections. Although this modeling study is a somewhat idealized picture of reality, it does represent the potential resolving power of cross-well imaging.

The cross-well processing flow is able to produce high resolution images of the velocity models. The seismic data from model 1 could not resolve every clinoform because some are too small to be imaged and/or the velocity contrast is too small to produce a noticeable reflection. Even though not all the clinoforms can be imaged, the dominant trend of the layers is captured and the divisions between the three main clinoform packages (clinoform cap, proximal, and distal) are identifiable. Models 2 and 3 are derived from well logs and core data that contain highly impermeable calcite-cemented concretionary intervals that impede fluid flow. These intervals are observed to be less than 1m thick in the well data, and their lateral extents are poorly understood because they are below the resolution of surface seismic data. Within the models their thickness and latent extents are varied, and the cross-well seismic data images concretionary intervals as small as 0.5m thick, and resolves their lateral terminations within +/-5m. In addition to the concretionary intervals, metre-scale shale partings and siltstone layers are imaged. These results demonstrate the effectiveness of the cross-well seismic method for mapping permeability barriers in reservoirs.

The cross-well seismic data sections contain interpretable reflections, but within the reservoir intervals small-scale variations (<1m) produce a scattered wavefield that cannot be visually interpreted. Statistical analysis through mapping the lateral spatial properties of the scattered wavefield provides estimates of the lateral correlation length and the fractal dimension. Attribute maps of power, correlation length, and Hurst number, along with histograms of the mapped values, are used to interpret the spatial properties. Whole reservoir measurements are also derived of the whole reservoir intervals in the

models that provide an average correlation length and Hurst number. The mean and median of the attribute maps in the reservoir interval agree with the whole reservoir measurements, providing evidence that the mapped values are accurate until the correlation lengths become longer then analysis window size, at which point the measurements have to be interpreted as relative values. The results display a unique distribution of spatial properties for each model, indicating the statistics are able to reveal the underlying structure of heterogeneity captured by the seismic data. When relating the statistics back to the stochastic parameters of the velocity fields in models 2 and 3, show that the Hurst numbers can be used quantitatively, but the correlation length can be ambiguous probably because they are limited by the resolution of seismic data. The synthetic cross-well seismic images from the three models provide small-scale lithological detail, and high resolution statistical information extracted from the seismic data supply lateral spatial properties of the reservoirs. This information can provide high resolution statistical constraints for flow simulations to reduce uncertainty in simulation results.

5.2 Summary of Contributions

Two main contributions concerning the cross-well seismic method was made in this thesis. First, new information was derived from the reflection data in the form of geostatistics. Correlation length and Hurst number measurements were extracted from the seismic data to aid in understanding the spatial characteristics of the seismic wavefield where visual interpretation was ineffective. The second contribution

concerned the method of transforming the data from the cross-well domain to the CDP domain. A limited aperture Kirchhoff migration was used to transform each source and receiver gather individually for the construction of CDP gathers, which enabled the editing of the gathers to improve the stacking process. These two contributions should aid interpretation of cross-well seismic data through additional information extracted from the data in the form of geostatistics, and improving the cross-well seismic image quality.

5.3 Looking Ahead

This thesis has provided additional information for the understanding of reservoirs, so the next stage is to evaluate the implementation of this new information and its effectiveness. This can be achieved by incorporating the information from the cross-well seismic data into a reservoir flow simulation deterministically and statistically. The cross-well seismic data provides a high resolution image of the reservoir that bridges the resolution gap between the surface seismic data and well log data, and the geostatistical information can be used as high resolution constraints during flow simulations. Incorporating the data into flow simulations should be done in two steps.

The first step would be to evaluate the implementation of the cross-well seismic information in a controlled experiment using a 3-D model of a well-known reservoir where production data is known. Shoot a synthetic cross-well seismic dataset through a model of the reservoir, process the data, and extract the statistics. Incorporate the information obtained from the cross-well data into flow simulations and compare to the

original flow simulation results. Hopefully, the flow simulations with the cross-well data will yield improved results. The next step after this would be to use real cross-well seismic data from a reservoir, and extract the geostatistical information from this data. The deterministic and statistical information gained from the cross-well seismic data, would again be used in the flow simulations to compare to the original results. The results should yield more accurate realizations from the simulations.

References

Abdalla, A. A., Stewart, R. R., and Henley, D. C., 1990, Traveltime inversion and reflection processing of crosshole seismic data: Expanded abstracts of the 60th Ann. Internat. Mtg., Soc. Expl. Geophys., 47-50

Baker, L. J., and Harris, J. M., 1984, Cross-borehole seismic imaging: Expanded abstracts of the 54th Ann. Internat. Mtg., Soc. Expl. Geophys., 23-25

Berkhout, A.J. (1984). *Seismic resolution: Resolving power of acoustical echo techniques.* London – Amersterdam: Geophysical Press, pp. 95-146

Beydoun, W. B., Delvaux, J., Mendes. M., Noual, G., and Tarantola, A., 1988, Practical aspects of an elastic migration/inversion of crosshole data for reservoir characterization: a Paris basin example: Geophysics 54, 1587-1595

Byun, J., Rector III, J.W., Nameth, T., 2002, Postmap migration of cross-well reflection seismic data: Geophysics, **67**, 135 – 146

Byun, J., 1999, The effects of wide incidence angles on crosswell reflection imaging: Journal of Seismic Exploration, **8**, 101 - 115

Chidsey, T.C. (2001). *Geological and Petrophysical Characterization of the Ferron Sandstone for 3-D simulation of a Fluvial-Deltaic Reservoir.* Salt Lake City: Utah Geological Survey

Deutsch, C.V., Hewett, T.A., 1996, Challenges in Reservoir Forecasting: Mathematical Geology, **28**, no.7, 829-842

Dillon, P.B., 1988, Vertical seismic profile migration using the Kirchhoff integral: Geophysics, **53**, 786-799

Dong, Q, and Marion, B., 2005, Imaging complex structure with crosswell seismic in Jianghan oil field: The Leading Edge, **24**, 18 – 23

Enachescu, M.E., 1987, Tectonic and Structural Framework of the Northeast Newfoundland Continental Margin: Canadian Society of Petroleum Geologists, Memoir 12, p.117 – 146

Frankel, A., Clayton, R.W., 1986, Finite-difference simulations of seismic scattering: implications for propagation of short-period seismic waves in the crust and models of crustal heterogeneity: Journal of Geophysical Research, **91**, 6465-6489

Grammer, G. M., Harris, P. M., Eberli, G. P., 2004, Integration of outcrop and modern analogs in reservoir modeling: Overview with examples from the Bahamas, *in* Integration of outcrop and modern analogs in reservoir modeling: AAPG Memoir 80, 1-22

Harris, J.M., Nolen-Hoeksema, R.C., Langan, R.T., Van Schaack, S., Lazaratos, S.K., Rector, J.W., 1995, High-resolution cross-well imaging of a west Texas carbonate reservoir: Part 1 – Project summary and interpretation: Geophysics, **60**, 667 – 681

Hollinger, K., Levander, A.R., 1992, A stochastic view of lower crustal fabric based on evidence from the Ivrea Zone: Geophysics Research Letters, **19**, 1153-1156

Hurich, C.A., 2003, Origins and scales of crustal heterogeneity: a case study from the Grenville Province, In: Heterogeneity in the Crust and Upper Mantle: Nature, Scaling and Seismic Properties, J.A. Goff and K. Holliger, eds., Kluwer Academic, New York, p. 299-320

Hurich, C.A., Kocurko, A., 2000, Statistical approaches to interpretation of seismic reflection data: Tectonophysics, **329**, 251-267

Husky Oil Operations Limited. 2001. White Rose Development Application, Project Summary. Prepared for Canadian Newfoundland and Labrador Offshore Petroleum Board St. John's, NL

Husky Oil Operations Limited. 2000. White Rose Oilfield Project Description. Prepared for Canadian Newfoundland and Labrador Offshore Petroleum Board, St. John's, NL

Iverson, W. P., 1988, Crosswell logging for acoustic impedance: J. Pet. Tech, 40, 75-82

Khalil, A.A., Stewart, R.R., Henley, D.C., 1993, Full-waveform processing and interpretation of kilohertz cross-well seismic data: Geophysics, **58**, 1248-1256

Lazaratos, S.K., Harris, J.M., Rector, J.W., Van Schaack, M., 1995, High-resolution cross-well imaging of a west Texas carbonate reservoir: Part 4 – Reflection imaging: Geophysics, **60**, 702-711

Lazaratos, S.K., 1993, Cross-well reflection imaging. Ph.D. Thesis. Stanford University

Liu, W., West, G.F., 1998, Time-lapse cross-well seismic monitoring of the Athabasca Tar Sands at Steepbank: SEG Technical Program Expanded Abstract.

Normore, L., 2005, Diagenetic Controls on Permeability of the Ben Nevis/Avalon Sandstones, White Rose Field, Jeanne d'Arc Basin, Newfoundland, Canada: AAPG abstract

Parra, J.O., Price, V., Addington, C., Zook, B.J., Cumbest, R.J., 1998, Interwell seismic imaging at the Savannah River Site, South Carolina: Geophysics, **63**, 1858-1865
Pittman, E.D., 1979, Porosity, diagenesis and productive capability of sandstone reservoirs: SEPM Special Publication, no. 26, p. 159-173

Paulsson, J.A., Meredith, J.A., Wang, Z., 1994, The Steepbank crosswell seismic project: Reservoir definition and evaluation of steamflood technology in Alberta tar sands: The Leading Edge, **13**, 737-747

ProMAX® VSP Reference, Landmark Graphics Corporation, Sept. 1998

Rector, J.W., Lazaratos, S.K., Harris, J.M., Van Schaack, M., 1995, High-resolution cross-well imaging of a west Texas carbonate reservoir: Part 3 – Wavefield separation of reflections: Geophysics, **60**, 692-701

Rector, J.W., Lazaratos, S.K., Harris, J.M., Van Schaack, M., 1994, Multidomain analysis and wavefield separation of cross-well seismic data: Geophysics, **59**, 27-35

Rowbotham, P.S., Goulty, N.R., 1994, Wavefield separation by 3-D filtering in crosshole seismic reflection processing: Geophysics, **59**, 1065-1071

Sheline, H.E., 1998, Cross-well seismic interpretation and reservoir characterization: An offshore case history: The Leading Edge, **17**, 935 – 939

Sheriff, R.E. (1991). *Encyclopedic Dictionary of Exploration Geophysics* (3rd ed.). Tulsa,OK: Society of Exploration Geophysicists

Van Schaack, M., Harris, J.M., Rector, J.W., Lazaratos, S.K., 1995, High-resolution cross-well imaging of a west Texas carbonate reservoir: Part 2 – Wavefield modeling, and analysis: Geophysics, **60**, 682-691

Whelan G., Schlumberger Senior Data Management Specialist, 2006

Yilmaz, O. (1987). *Seismic Data Processing*. Tulsa, OK: Society of Exploration Geophysicists

http://www.budget.gov.nl.ca/budget2001/economy/whiteRose.htm

Appendix A

Vertical and Horizontal Resolution of Cross-well Seismic Data

A.1 Vertical Resolution

The vertical resolution calculations utilize the Rayleigh resolution limit through the equation,

$$\lambda = 4v/f$$

where λ is wavelength, v is velocity, and f is frequency. The Rayleigh resolution limit is defined as the minimum distance between successive reflections such that their individual entities can be recognized is $\lambda/4$, (Sheriff, 1991). Features below this limit can still be detected, as they produce a scattered wavefield (i.e. diffractions) indicating heterogeneities exist, but cannot be resolved. This discussion however, is limited to resolvable features meeting the Rayleigh resolution criteria.

Figures A.1 and A.2 display wavelengths calculated from the above equation over typical velocities found in petroleum reservoirs for surface and cross-well seismic data frequencies, respectively. The figures show cross-well seismic data has about a 10-fold increase in vertical resolution over surface seismic data and that layers of less than 1m thickness may theoretical be resolvable using the cross-well seismic method. This is a significant increase in vertical resolution that can significantly improve imaging at depths of petroleum reservoirs.

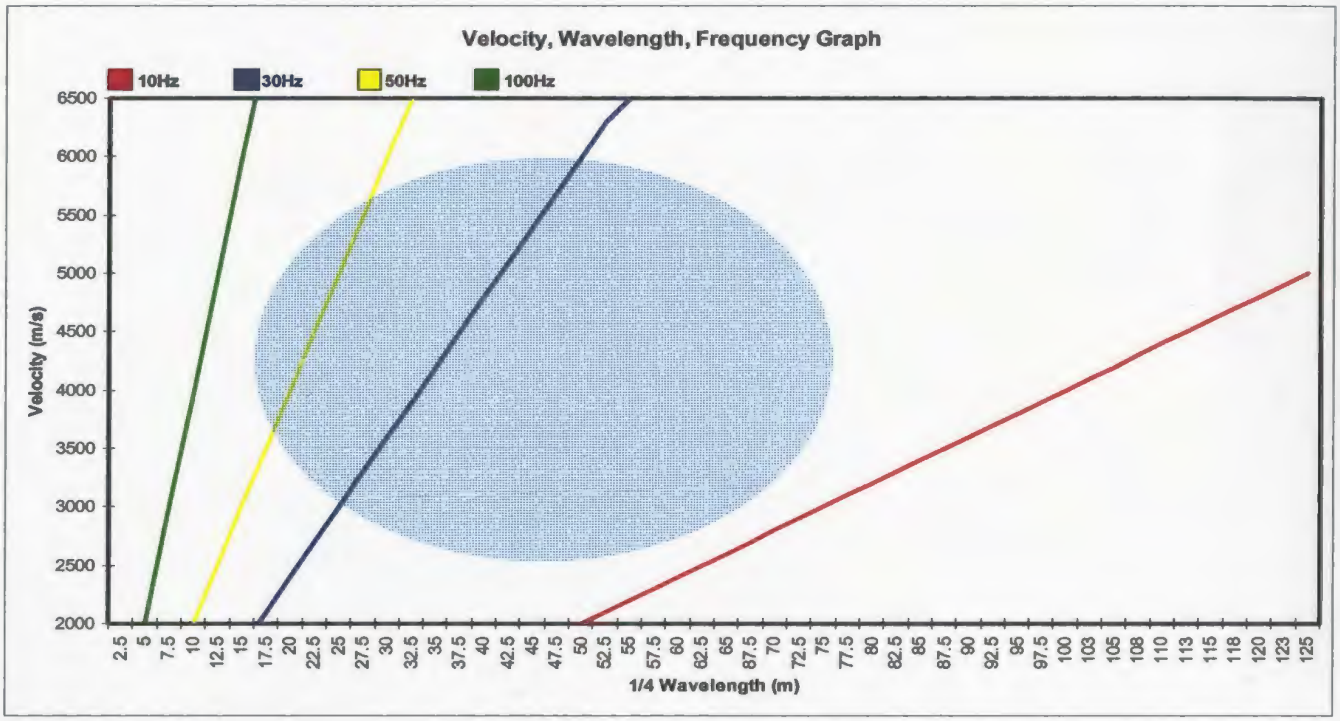

Figure A.1: Graph showing the Rayleigh resolution limit for surface seismic data. Highlighted areas show typical ranges of velocity and wavelength.

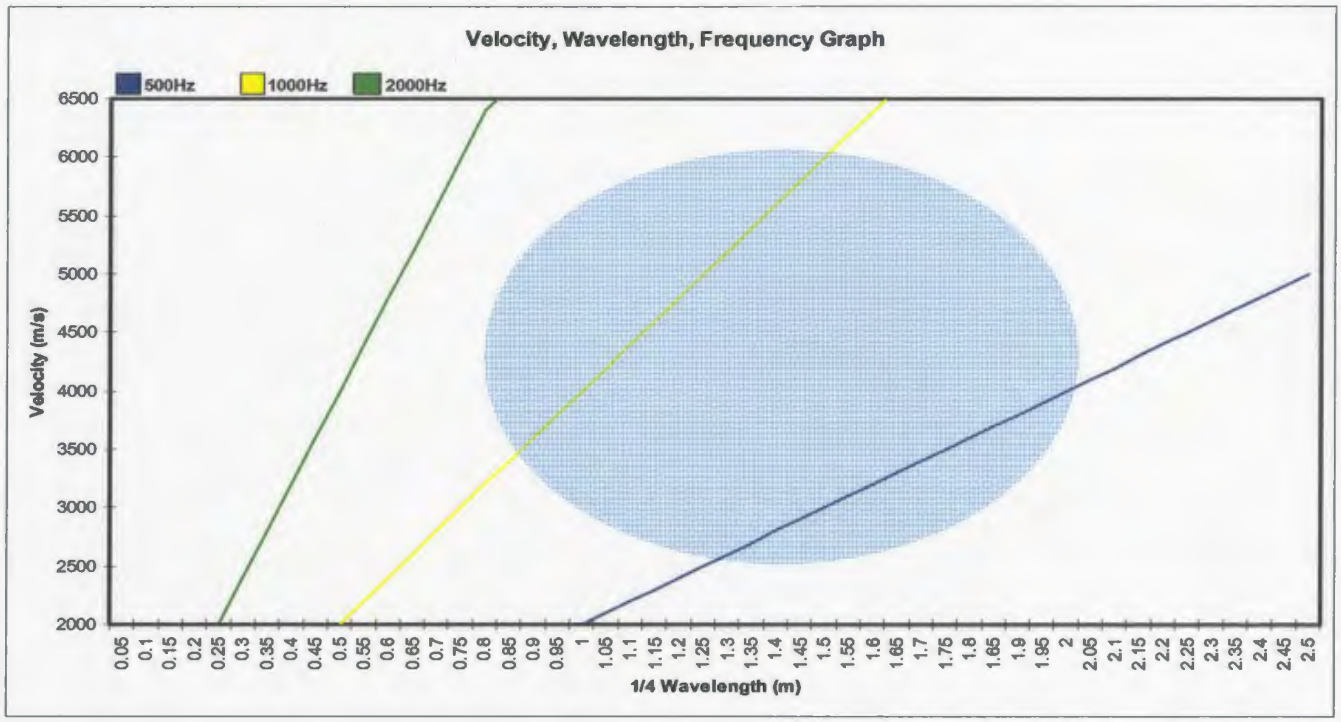

Figure A.2: Graph showing the Rayleigh resolution limit for cross-well seismic data. Highlighted areas show typical ranges of velocity and wavelength.

A.2 Lateral Resolution

A common way of quantifying the lateral resolution is through the notion of Fresnel zones. The first Fresnel zone is defined as the portion of a reflector from which reflected energy can reach a detector within 1/2 wavelength of the first reflected energy (Sheriff, 1991). The full Fresnel zone is composed of in-plane and out-of-plane Fresnel zone components (Figure A.3), but since this is a 2-D seismic survey, only the in-plane Fresnel zone is discussed here and a discussion of the out-of-plane Fresnel zone is given by Lazaratos (1993).

The in-plane Fresnel zone calculation for cross-well data is demonstrated by Lazaratos (1993). He shows that the in-plane Fresnel zone is dependent upon inter-well distance, distance a reflection point is away from the borehole, incident angle, and wavelength (Figure A.4). Figure A.5 shows the Fresnel zone as a function of horizontal location of reflection point, incident angle, and wavelength, where both Fresnel zone and reflection point location are normalized by the inter-well distance. In general, the figure demonstrates that resolution is best closest to the wells and decreases as reflections approach the midpoint of the wells, and as the incident angle increases so does the Fresnel zone. Table A.1 displays three examples demonstrating the dependency of the in-plane Fresnel zone on the acquisition geometry of a cross-well seismic survey.

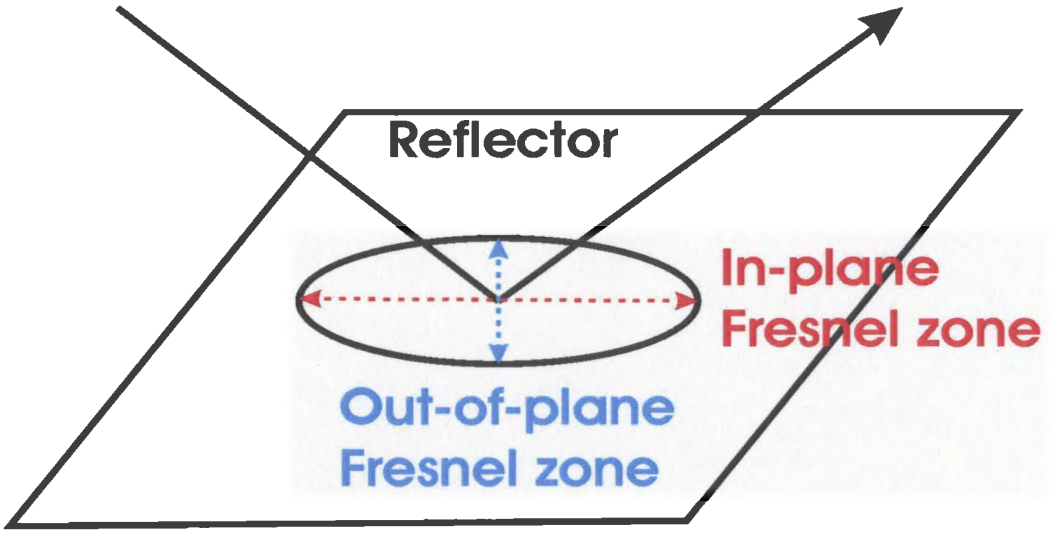

Figure A.3: Schematic displaying the geometry of the in-plane and out of-plane components of the Fresnel zone.

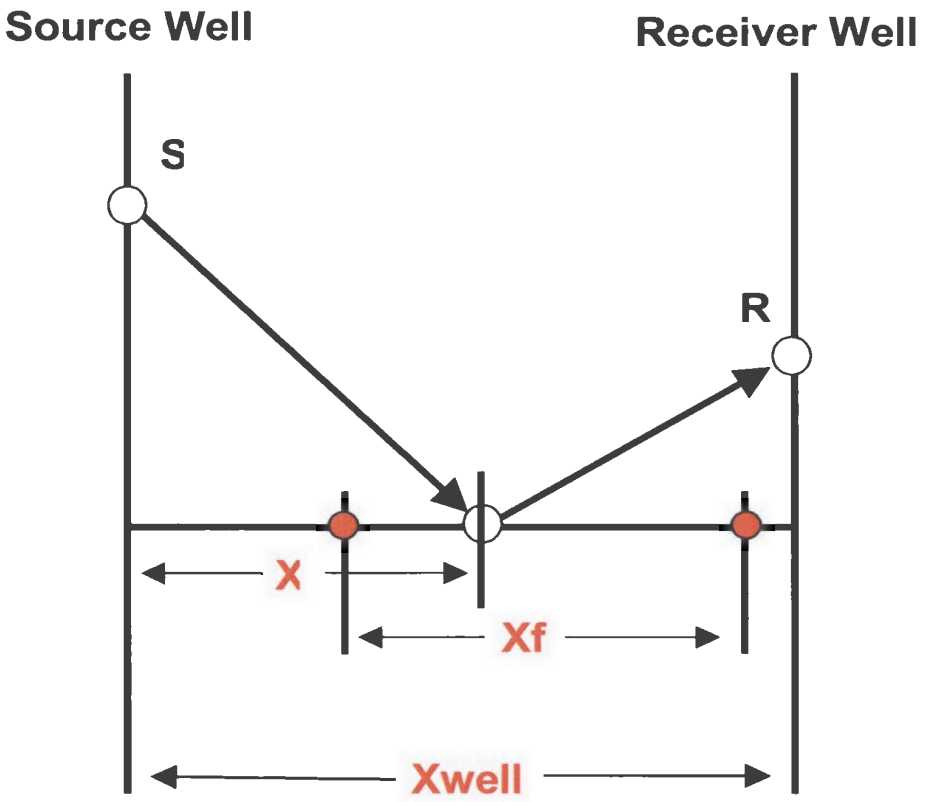

Figure A.4: Basic geometry for describing calculating in-plane Fresnel zone. X is the distance away from source well, X_F is the size of Fresnel zone, and X_{WELL} is the interwell distance.

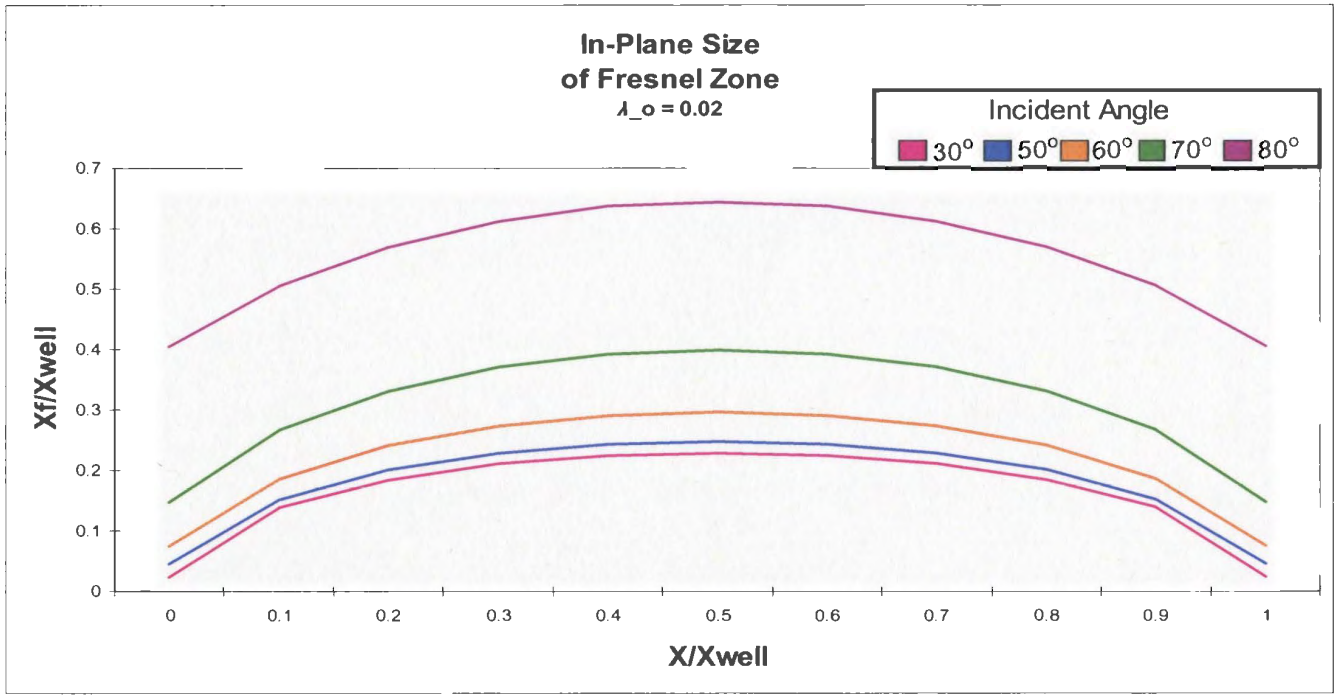

Figure A.5: The in-plane size of the Fresnel zone, as a function of the lateral position between the boreholes (X), incident angle, and dominant wavelength (λ). The lateral position between the boreholes, Fresnel zone size, and wavelength has been normalized by the interwell distance (Xwell) (modified from Lazaratos, 1993).

Example	X_{WELL}(m)	Incident Angle (degrees)	X(m)	X_F(m)
1	100	50	10	15
2	100	50	40	25
3	100	70	15	30

Table A.1: Example calculations demonstrating the effect of acquisition geometry on the cross-well Fresnel zone with a constant wavelength. The parameters are interwell distance (X_{WELL}), incident angle, distance reflection point is away from source well (X), and Fresnel zone (X_F).

The one parameter not dependant on the acquisition geometry is the wavelength. Wavelength is dependant on the wavelet frequency and the velocity of the medium the wave propagates through. As frequency increases, the wavelength decreases and so does the Fresnel zone (Figure A.6). The decrease in Fresnel zone is most dramatic at the lower frequency range where surface seismic data is recorded and less discernible at higher frequencies where cross-well data is recorded. Therefore, to obtain significant improvements in lateral resolution once in the kHz range, large increases in frequency content is needed.

Even though the Fresnel zone measures the lateral resolution, it does not however, represent the theoretical limit because migration possesses the ability to shrink the Fresnel zone. This study uses a migration to transform the data from the cross-well domain to the CDP domain (discussed more in Chapter 3), but the migration parameterization does not collapse the Fresnel zone. A limited aperture migration is used to simulate a VSP-CDP transform, which does not utilize the full potential horizontal wavenumber spectrum from the data (Berkhout, 1984), hindering the migration from shrinking the Fresnel zone. The horizontal resolution is therefore limited to the Fresnel zone size.

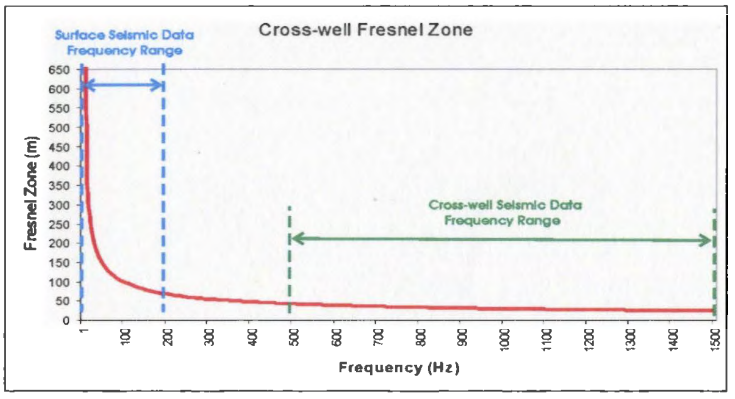

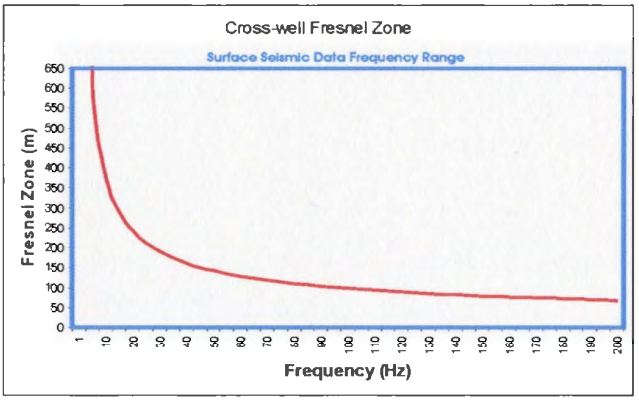

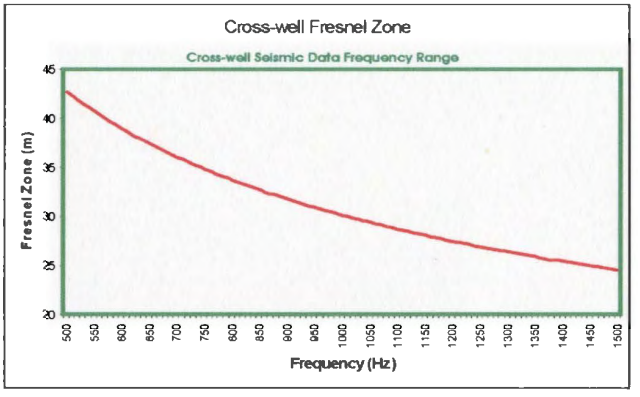

Figure A.6: Graphs of the cross-well Fresnel zone vs. frequency. The graphs assume a velocity of 4500m/s, an incident angle of 30°, an inter-well distance of 100m, and a reflection point 25m away from the borehole.

Appendix B

Permeability to Velocity Calculations

Location of Permeability Transects

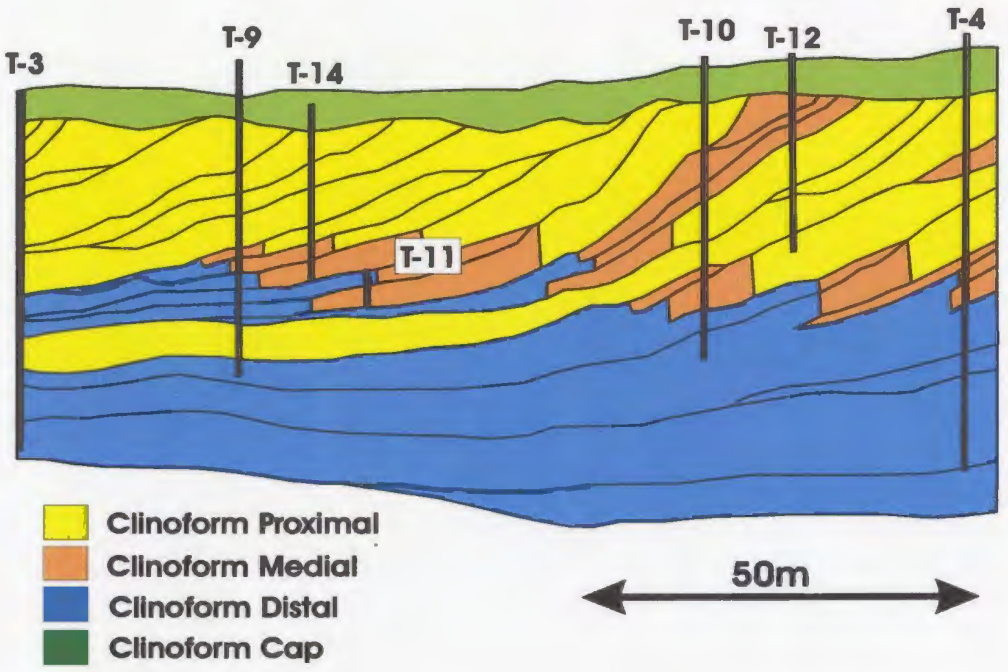

Columns:

1) Elevations (m) as taken from field during permeability measurements
2) Permeability (mD)measurements taken from field
3) Porosities derived from permeabilities through equation, **ln(k) = -6.657 + 56.6 * ö,** where ö porosity and k is permeability
4) Velocity (m/s) derived from porosities through equation, **$v = -9E^{-10}ö^2 - 9683.2ö + 5765.7$**, where v is velocity and ö is porosity

T-3

10.55	0.75	0.11	4676.03
10.82	1.45	0.12	4563.24
11.00	3.42	0.14	4416.44
11.09	0.99	0.12	4628.53
12.38	0.67	0.11	4695.33
12.53	1.36	0.12	4574.21
12.62	1.39	0.12	4570.47
12.81	1.38	0.12	4571.71
12.90	0.85	0.11	4654.62
13.44	0.47	0.10	4755.98
13.52	0.48	0.10	4752.38
13.61	0.47	0.10	4755.98
13.69	0.48	0.10	4752.38
13.78	0.47	0.10	4755.98
13.86	0.47	0.10	4755.98
13.95	0.49	0.11	4748.85
14.12	0.47	0.10	4755.98
14.28	0.48	0.10	4752.38
14.37	0.49	0.11	4748.85
14.54	1.17	0.12	4599.95
14.65	5.58	0.15	4332.69
14.75	1.36	0.12	4574.21
14.93	1.60	0.13	4546.40
15.02	1.39	0.12	4570.47
15.11	1.78	0.13	4528.16
15.20	3.35	0.14	4419.98
15.38	2.86	0.14	4447.04
15.56	1.00	0.12	4626.81
15.65	3.11	0.14	4432.70
15.75	1.48	0.12	4559.74
15.84	2.37	0.13	4479.19
15.93	2.12	0.13	4498.26
16.29	9.28	0.16	4245.67
16.68	2.92	0.14	4443.48
16.78	4.04	0.14	4387.94
16.87	4.22	0.14	4380.48
17.05	4.62	0.14	4364.99
17.14	6.65	0.15	4302.68
17.23	6.23	0.15	4313.84
17.32	5.00	0.15	4351.47
17.41	5.93	0.15	4322.28
17.50	3.09	0.14	4433.80
17.59	4.72	0.15	4361.33
17.68	2.96	0.14	4441.16
17.96	13.41	0.16	4182.68
18.05	13.84	0.16	4177.29
18.14	12.97	0.16	4188.39
18.23	16.08	0.17	4151.62
18.32	6.40	0.15	4309.23
18.41	1.90	0.13	4517.00
18.50	18.55	0.17	4127.17
18.59	7.06	0.15	4292.44
18.68	16.41	0.17	4148.15
18.96	13.91	0.16	4176.42
19.14	8.68	0.16	4257.10
19.23	6.36	0.15	4310.31
19.32	5.00	0.15	4351.47
19.41	5.00	0.15	4351.47
19.59	3.23	0.14	4426.22
19.68	0.57	0.11	4722.98
19.78	11.92	0.16	4202.84
19.87	4.86	0.15	4356.33
20.05	9.90	0.16	4234.60
20.23	6.37	0.15	4310.04
20.32	12.52	0.16	4194.43
20.41	8.49	0.16	4260.89
20.50	13.02	0.16	4187.73
20.68	8.66	0.16	4257.50
20.78	4.25	0.14	4379.27
20.96	10.84	0.16	4219.08
21.05	8.16	0.15	4267.67
21.14	7.25	0.15	4287.90
21.23	9.07	0.16	4249.58
21.32	11.33	0.16	4211.52
21.41	7.92	0.15	4272.78
21.50	14.09	0.16	4174.22
21.59	8.26	0.15	4265.59
21.68	6.83	0.15	4298.11
21.78	18.38	0.17	4128.75
21.95	1.61	0.13	4545.34
22.04	12.81	0.16	4190.52
22.13	5.73	0.15	4328.15
22.31	13.07	0.16	4187.08
22.39	9.99	0.16	4233.05
22.48	8.18	0.15	4267.25
22.57	17.42	0.17	4137.93
22.66	19.08	0.17	4122.35
22.75	21.50	0.17	4101.93
23.18	22.51	0.17	4094.07
23.27	11.96	0.16	4202.26

23.36	13.51	0.16	4181.41
23.45	8.21	0.15	4266.63
23.54	5.65	0.15	4330.56
23.62	7.29	0.15	4286.96
23.71	10.02	0.16	4232.54
23.80	10.94	0.16	4217.51
23.89	8.61	0.16	4258.49
23.98	57.27	0.19	3934.31
24.33	2.95	0.14	4441.74
24.59	2.72	0.14	4455.62
24.76	0.56	0.11	4726.01
24.84	0.74	0.11	4678.33
24.93	1.00	0.12	4626.81
25.01	0.68	0.11	4692.79
25.10	1.08	0.12	4613.65
25.18	1.47	0.12	4560.90
25.50	1.43	0.12	4565.62
25.58	1.35	0.12	4575.47
25.65	1.60	0.13	4546.40
25.73	5.00	0.15	4351.47
25.81	3.40	0.14	4417.45
27.40	4.17	0.14	4382.52
27.67	10.62	0.16	4222.59
27.76	4.84	0.15	4357.03
28.44	1.72	0.13	4534.03
28.53	0.90	0.12	4644.84
28.72	0.63	0.11	4705.86
28.90	0.66	0.11	4697.90
29.08	2.85	0.14	4447.64
29.17	5.24	0.15	4343.45
29.35	2.50	0.13	4470.05
29.44	4.01	0.14	4389.22

T-9

13.85	1.97	0.13	4510.81
13.94	1.97	0.13	4510.81
14.03	2.02	0.13	4506.53
14.12	2.03	0.13	4505.68
14.21	2.06	0.13	4503.17
14.30	2.13	0.13	4497.45
14.39	2.14	0.13	4496.65
14.48	2.09	0.13	4500.70
14.58	2.10	0.13	4499.88
14.68	2.14	0.13	4496.65
14.79	2.34	0.13	4481.37
14.89	2.13	0.13	4497.45
14.99	2.16	0.13	4495.06
15.09	2.18	0.13	4493.48
15.19	2.21	0.13	4491.15
15.27	2.25	0.13	4488.08
15.36	2.30	0.13	4484.32
15.45	2.30	0.13	4484.32
15.55	2.34	0.13	4481.37
15.64	2.31	0.13	4483.57
15.73	2.34	0.13	4481.37
15.82	2.13	0.13	4497.45
15.92	2.18	0.13	4493.48
16.10	2.22	0.13	4490.37
16.19	2.25	0.13	4488.08
16.28	2.04	0.13	4504.84
16.37	1.15	0.12	4602.90
16.47	1.31	0.12	4580.62
16.56	1.06	0.12	4616.84
16.72	1.45	0.12	4563.24
16.82	1.39	0.12	4570.47
16.91	2.79	0.14	4451.28
17.33	3.79	0.14	4398.87
17.41	2.48	0.13	4471.43
17.48	2.93	0.14	4442.90
17.56	3.57	0.14	4409.10
17.65	5.12	0.15	4347.41
17.73	3.65	0.14	4405.31
17.82	2.00	0.13	4508.23
17.90	2.86	0.14	4447.04
17.98	3.95	0.14	4391.79
18.15	4.43	0.14	4372.17
18.23	2.88	0.14	4445.84
18.32	3.21	0.14	4427.28
18.40	2.71	0.14	4456.25
18.48	2.26	0.13	4487.32
18.57	2.24	0.13	4488.84
18.65	2.71	0.14	4456.25
18.74	1.60	0.13	4546.40
18.82	1.94	0.13	4513.44
18.91	21.48	0.17	4102.08
18.99	5.88	0.15	4323.73
19.08	5.07	0.15	4349.09
19.16	9.77	0.16	4236.86
19.25	8.38	0.16	4263.12
19.33	19.35	0.17	4119.95
19.41	17.90	0.17	4133.28
19.50	25.65	0.17	4071.73
19.77	35.60	0.18	4015.65
19.95	9.22	0.16	4246.78
20.04	4.37	0.14	4374.51
20.12	9.56	0.16	4240.58
20.21	13.84	0.16	4177.29
20.62	44.74	0.18	3976.55
20.71	39.78	0.18	3996.66
20.79	19.93	0.17	4114.90
20.88	8.32	0.16	4264.35
20.97	21.49	0.17	4102.01
21.06	35.24	0.18	4017.39
21.15	60.66	0.19	3924.47
21.24	8.57	0.16	4259.28
21.33	5.16	0.15	4346.08
21.42	9.57	0.16	4240.40
21.50	11.37	0.16	4210.92
21.59	96.33	0.20	3845.35
21.68	36.86	0.18	4009.70
21.77	24.85	0.17	4077.15
21.86	44.59	0.18	3977.13
21.95	87.14	0.20	3862.50
22.05	115.69	0.20	3814.02
22.15	73.93	0.19	3890.63
22.25	408.85	0.22	3598.04
22.35	213.52	0.21	3709.18
22.44	565.42	0.23	3542.57
22.54	250.97	0.22	3681.53
22.64	150.16	0.21	3769.40
22.74	127.05	0.20	3797.99
22.88	26.93	0.18	4063.40
23.02	34.95	0.18	4018.80
23.16	36.93	0.18	4009.38

23.30	197.30	0.21	3722.69
23.44	6.92	0.15	4295.87
23.57	25.74	0.18	4071.13
23.66	3.69	0.14	4403.44
23.75	11.65	0.16	4206.76
23.83	8.57	0.16	4259.28
23.92	4.88	0.15	4355.62
24.01	2.87	0.14	4446.44
24.09	9.91	0.16	4234.43
24.18	3.06	0.14	4435.47
24.32	13.37	0.16	4183.20
24.40	154.59	0.21	3764.43
24.48	44.80	0.18	3976.33
25.01	2.01	0.13	4507.37
25.09	2.05	0.13	4504.00
25.16	2.55	0.13	4466.66
25.22	2.12	0.13	4498.26
25.40	2.14	0.13	4496.65
25.48	2.17	0.13	4494.27
25.57	2.27	0.13	4486.56
25.68	2.25	0.13	4488.08
25.77	2.30	0.13	4484.32
25.86	1.76	0.13	4530.10
25.95	2.51	0.13	4469.37
26.03	1.83	0.13	4523.42
26.12	1.85	0.13	4521.57
26.21	1.90	0.13	4517.00
26.30	1.95	0.13	4512.56
27.71	1.94	0.13	4513.44
27.80	2.02	0.13	4506.53
27.88	2.01	0.13	4507.37
27.97	6.52	0.15	4306.06
28.15	4.87	0.15	4355.97
28.41	24.24	0.17	4081.40
28.50	3.60	0.14	4407.67
28.59	40.14	0.18	3995.12
28.67	2.33	0.13	4482.10
28.75	6.57	0.15	4304.75
28.84	20.43	0.17	4110.66
28.92	117.24	0.20	3811.74
29.00	54.75	0.19	3942.01
29.09	100.30	0.20	3838.44

T-14

18.31	14.53	0.16	4168.96
18.40	24.52	0.17	4079.44
18.49	19.57	0.17	4118.02
18.58	46.40	0.19	3970.32
18.87	14.19	0.16	4173.01
19.05	3.96	0.14	4391.36
19.15	5.09	0.15	4348.42
19.24	13.74	0.16	4178.53
19.33	10.35	0.16	4227.00
19.42	20.49	0.17	4110.16
19.52	2.77	0.14	4452.51
19.61	21.48	0.17	4102.08
19.70	15.03	0.17	4163.17
19.79	6.69	0.15	4301.65
19.87	9.43	0.16	4242.92
19.88	21.62	0.17	4100.97
19.98	27.26	0.18	4061.32
20.06	48.07	0.19	3964.27
20.15	32.92	0.18	4029.04
20.23	41.21	0.18	3990.62
20.32	11.75	0.16	4205.29
20.40	40.26	0.18	3994.61
20.49	12.75	0.16	4191.32
20.57	56.29	0.19	3937.27
20.66	51.04	0.19	3954.02
20.75	166.18	0.21	3752.06
20.83	34.98	0.18	4018.66
20.92	58.04	0.19	3932.03
21.11	34.28	0.18	4022.11
21.21	5.63	0.15	4331.16
21.30	5.55	0.15	4333.61
21.40	3.62	0.14	4406.72
21.59	10.87	0.16	4218.61
21.68	4.90	0.15	4354.92
21.77	2.94	0.14	4442.32
21.86	6.49	0.15	4306.85
21.95	3.26	0.14	4424.64
22.04	2.11	0.13	4499.07
22.13	6.71	0.15	4301.14
22.23	51.66	0.19	3951.95
22.31	100.96	0.20	3837.32
22.56	19.10	0.17	4122.18
22.65	12.54	0.16	4194.16
22.73	10.66	0.16	4221.95
22.82	9.18	0.16	4247.52
22.92	14.51	0.16	4169.20
23.01	74.76	0.19	3888.72
23.10	11.86	0.16	4203.70
23.19	25.41	0.17	4073.34
23.28	91.03	0.20	3855.03
23.37	81.19	0.20	3874.60
23.46	31.05	0.18	4039.05

T-11

16.51	5.35	0.15	4339.89
16.60	10.09	0.16	4231.35
16.69	12.04	0.16	4201.12
16.79	5.69	0.15	4329.35
16.88	4.99	0.15	4351.81
16.97	7.76	0.15	4276.27
17.07	3.66	0.14	4404.84
17.11	12.85	0.16	4189.98
17.23	4.47	0.14	4370.64
17.32	4.48	0.14	4370.25

T-10

14.88	2.40	0.13	4477.04
14.97	1.77	0.13	4529.13
15.06	1.79	0.13	4527.21
15.15	1.81	0.13	4525.30
15.25	1.85	0.13	4521.57
15.34	1.91	0.13	4516.10
15.52	2.67	0.13	4458.80
15.61	2.74	0.14	4454.37
15.70	1.99	0.13	4509.09
15.80	2.85	0.14	4447.64
15.90	2.96	0.14	4441.16
15.99	3.24	0.14	4425.69
16.26	3.29	0.14	4423.07
16.45	3.36	0.14	4419.47
16.63	3.42	0.14	4416.44
16.82	3.49	0.14	4412.98
17.00	4.18	0.14	4382.11
17.11	4.17	0.14	4382.52
17.27	21.39	0.17	4102.80
17.35	4.60	0.14	4365.73
17.43	1.75	0.13	4531.07
17.51	1.76	0.13	4530.10
17.58	2.98	0.14	4440.00
17.67	2.07	0.13	4502.34
17.75	2.21	0.13	4491.15
17.92	1.94	0.13	4513.44
18.00	6.74	0.15	4300.38
18.08	11.88	0.16	4203.41
18.17	3.61	0.14	4407.19
18.25	2.70	0.14	4456.89
18.34	4.08	0.14	4386.26
18.42	2.75	0.14	4453.75
18.50	13.17	0.16	4185.77
18.58	4.81	0.15	4358.10
18.67	3.52	0.14	4411.51
18.79	3.82	0.14	4397.52
18.91	7.31	0.15	4286.49
19.03	6.73	0.15	4300.63
19.15	6.01	0.15	4319.99
19.26	10.05	0.16	4232.03
19.32	2.12	0.13	4498.26
19.38	14.54	0.16	4168.84
19.48	3.09	0.14	4433.80
19.50	8.36	0.16	4263.53
19.64	33.79	0.18	4024.58
19.80	7.11	0.15	4291.24
19.96	14.51	0.16	4169.20
20.12	4.19	0.14	4381.70
20.32	2.46	0.13	4472.81
20.41	40.01	0.18	3995.67
20.50	2.28	0.13	4485.81
20.59	11.03	0.16	4216.11
20.68	1.97	0.13	4510.81
20.77	2.01	0.13	4507.37
20.85	2.06	0.13	4503.17
20.95	2.10	0.13	4499.88
21.03	2.16	0.13	4495.06
21.12	3.31	0.14	4422.04
21.34	2.25	0.13	4488.08
21.41	2.13	0.13	4497.45
21.48	2.05	0.13	4504.00
21.55	2.91	0.14	4444.07
21.62	2.18	0.13	4493.48
21.70	6.20	0.15	4314.67
21.77	2.00	0.13	4508.23
21.84	2.04	0.13	4504.84
21.91	2.05	0.13	4504.00
22.00	2.11	0.13	4499.07
22.15	2.26	0.13	4487.32
22.23	2.00	0.13	4508.23
22.31	2.05	0.13	4504.00
22.38	2.36	0.13	4479.91
22.46	6.16	0.15	4315.77
22.55	7.46	0.15	4283.01
22.64	12.99	0.16	4188.13
22.73	10.71	0.16	4221.15
22.82	6.96	0.15	4294.88
22.91	12.89	0.16	4189.45
22.99	2.29	0.13	4485.06
23.08	4.61	0.14	4365.36
23.17	21.75	0.17	4099.95
23.26	13.29	0.16	4184.22
23.35	13.03	0.16	4187.60
23.44	16.24	0.17	4149.93
23.54	5.91	0.15	4322.86
23.63	5.69	0.15	4329.35
23.72	16.42	0.17	4148.04
23.81	18.82	0.17	4124.70
23.91	35.88	0.18	4014.31
24.00	30.45	0.18	4042.38

24.09	2.16	0.13	4495.06
24.18	2.62	0.13	4462.03
24.29	1.96	0.13	4511.68
24.39	1.95	0.13	4512.56
24.48	1.98	0.13	4509.95
24.68	2.08	0.13	4501.52
24.78	2.11	0.13	4499.07
24.86	13.43	0.16	4182.43
24.95	8.48	0.16	4261.09
25.03	11.46	0.16	4209.57
25.12	6.30	0.15	4311.93
25.34	7.56	0.15	4280.74
25.43	5.39	0.15	4338.62
25.51	3.03	0.14	4437.16
25.75	13.11	0.16	4186.56
25.80	100.90	0.20	3837.42
28.18	18.95	0.17	4123.52
28.26	35.21	0.18	4017.54
28.34	1.99	0.13	4509.09
28.41	2.02	0.13	4506.53
28.49	13.15	0.16	4186.03

T-12

19.03	61.15	0.19	3923.10
19.12	45.71	0.19	3972.89
19.22	34.65	0.18	4020.28
19.31	33.41	0.18	4026.51
19.40	35.90	0.18	4014.21
19.49	44.59	0.18	3977.13
19.58	15.35	0.17	4159.57
19.77	18.08	0.17	4131.56
19.86	15.37	0.17	4159.35
19.95	20.46	0.17	4110.41
20.05	20.00	0.17	4114.30
20.12	2.02	0.13	4506.53
20.30	6.04	0.15	4319.14
20.40	3.17	0.14	4429.43
20.50	2.52	0.13	4468.69
20.60	2.64	0.13	4460.73
20.70	24.22	0.17	4081.55
20.79	25.33	0.17	4073.88
20.87	7.80	0.15	4275.39
20.95	4.78	0.15	4359.17
21.03	7.56	0.15	4280.74
21.11	6.06	0.15	4318.57
21.18	25.12	0.17	4075.30
21.26	21.71	0.17	4100.26
21.35	10.03	0.16	4232.37
21.42	15.99	0.17	4152.58
21.51	17.74	0.17	4134.81
21.60	20.49	0.17	4110.16
21.68	17.63	0.17	4135.88
21.77	13.18	0.16	4185.64
21.85	12.55	0.16	4194.02
21.94	11.67	0.16	4206.46
22.03	10.33	0.16	4227.33
22.12	3.41	0.14	4416.94
22.20	4.42	0.14	4372.56
22.29	5.07	0.15	4349.09
22.38	2.13	0.13	4497.45
22.47	2.17	0.13	4494.27
22.55	2.16	0.13	4495.06
22.64	2.34	0.13	4481.37
22.82	2.22	0.13	4490.37
23.02	2.04	0.13	4504.84
23.22	2.01	0.13	4507.37
23.42	2.00	0.13	4508.23
23.61	3.62	0.14	4406.72
23.69	3.56	0.14	4409.58
23.78	11.53	0.16	4208.53
23.86	7.67	0.15	4278.27
23.87	6.43	0.15	4308.43
24.04	22.08	0.17	4097.37
24.13	10.72	0.16	4220.99
24.22	3.53	0.14	4411.03
24.30	2.17	0.13	4494.27
24.42	2.22	0.13	4490.37
24.52	2.16	0.13	4495.06
24.61	3.00	0.14	4438.86
24.70	22.30	0.17	4095.68

T-4

9.51	1.00	0.12	4626.81
9.68	2.97	0.14	4440.58
9.77	0.60	0.11	4714.20
9.85	0.55	0.11	4729.09
10.15	0.54	0.11	4732.23
10.27	0.57	0.11	4722.98
10.48	0.73	0.11	4680.65
10.55	2.17	0.13	4494.27
10.62	0.91	0.12	4642.95
10.69	1.35	0.12	4575.47
10.95	0.70	0.11	4687.83
11.05	0.62	0.11	4708.59
11.15	0.92	0.12	4641.08
11.53	1.16	0.12	4601.42
11.60	0.59	0.11	4717.08
11.69	0.78	0.11	4669.32
11.78	0.72	0.11	4683.01
11.96	0.67	0.11	4695.33
12.05	0.87	0.12	4650.64
12.22	1.37	0.12	4572.95
12.31	1.00	0.12	4626.81
12.40	1.89	0.13	4517.91
12.49	1.09	0.12	4612.07
12.58	1.35	0.12	4575.47
12.66	1.30	0.12	4581.93
13.33	1.00	0.12	4626.81
13.42	1.12	0.12	4607.42
13.50	0.90	0.12	4644.84
13.58	1.00	0.12	4626.81
13.75	1.62	0.13	4544.28
14.04	1.12	0.12	4607.42
14.24	0.69	0.11	4690.29
14.72	5.52	0.15	4334.54
14.91	1.61	0.13	4545.34
15.00	1.03	0.12	4621.76
15.09	1.48	0.12	4559.74
15.18	2.80	0.14	4450.66
15.27	1.55	0.13	4551.83
15.36	1.45	0.12	4563.24
15.45	2.48	0.13	4471.43
15.54	2.44	0.13	4474.21
15.63	3.09	0.14	4433.80
16.09	2.72	0.14	4455.62
16.18	1.67	0.13	4539.08
16.36	11.38	0.16	4210.77
16.45	4.63	0.14	4364.62
16.63	3.09	0.14	4433.80
16.72	13.11	0.16	4186.56
16.82	2.20	0.13	4491.92
16.91	3.52	0.14	4411.51
17.09	1.67	0.13	4539.08
17.18	1.36	0.12	4574.21
17.36	4.39	0.14	4373.73
17.45	3.25	0.14	4425.17
17.72	1.48	0.12	4559.74
17.91	1.34	0.12	4576.74
18.00	0.90	0.12	4644.84
18.10	0.79	0.11	4667.14
18.18	0.58	0.11	4720.00
18.19	0.86	0.11	4652.61
18.29	0.92	0.12	4641.08
18.38	0.59	0.11	4717.08
18.57	0.56	0.11	4726.01
18.66	0.51	0.11	4742.01
18.74	0.52	0.11	4738.69
18.82	0.57	0.11	4722.98
18.90	0.53	0.11	4735.43
19.18	1.00	0.12	4626.81
19.25	0.54	0.11	4732.23
19.35	2.69	0.14	4457.52
19.45	0.54	0.11	4732.23
19.56	0.74	0.11	4678.33
19.66	0.85	0.11	4654.62
19.76	0.81	0.11	4662.86
19.86	0.73	0.11	4680.65
19.96	0.67	0.11	4695.33
20.07	0.73	0.11	4680.65
20.17	1.20	0.12	4595.62
20.27	3.03	0.14	4437.16
20.45	3.71	0.14	4402.52
20.53	7.75	0.15	4276.49
20.62	9.47	0.16	4242.20
20.88	54.06	0.19	3944.18
20.96	13.68	0.16	4179.27
21.14	0.51	0.11	4742.01
21.40	2.69	0.14	4457.52
21.48	0.77	0.11	4671.53
21.57	5.10	0.15	4348.08
21.76	1.56	0.13	4550.73
21.85	3.15	0.14	4430.51

21.95	3.38	0.14	4418.46
22.05	8.49	0.16	4260.89
22.14	3.84	0.14	4396.63
22.23	11.48	0.16	4209.27
22.33	14.14	0.16	4173.62
22.42	1.59	0.13	4547.48
22.51	11.25	0.16	4212.73
22.60	6.62	0.15	4303.45
22.70	6.46	0.15	4307.64
22.79	24.61	0.17	4078.81
22.88	5.00	0.15	4351.47
22.97	26.23	0.18	4067.91
23.07	16.71	0.17	4145.05
23.16	1.60	0.13	4546.40
23.25	13.78	0.16	4178.03
23.43	1.00	0.12	4626.81
23.53	3.90	0.14	4393.97
23.90	31.67	0.18	4035.66
24.08	13.78	0.16	4178.03
24.26	27.90	0.18	4057.35
24.36	16.20	0.17	4150.35
24.45	47.01	0.19	3968.09
24.63	2.19	0.13	4492.70
24.72	0.54	0.11	4732.23
24.83	0.51	0.11	4742.01
24.94	0.52	0.11	4738.69
25.04	0.50	0.11	4745.40
25.15	0.51	0.11	4742.01
25.25	0.50	0.11	4745.40
25.36	0.50	0.11	4745.40
25.45	0.73	0.11	4680.65
25.58	0.50	0.11	4745.40
25.60	0.52	0.11	4738.69
25.89	0.50	0.11	4745.40
26.18	0.51	0.11	4742.01
26.45	7.22	0.15	4288.61
27.54	6.79	0.15	4299.11
27.62	3.07	0.14	4434.91
27.70	3.48	0.14	4413.47
27.78	3.06	0.14	4435.47
28.69	5.28	0.15	4342.15
28.78	4.22	0.14	4380.48